



THE UNIVERSITY OF
WAIKATO
Te Whare Wānanga o Waikato

Research Commons

<http://researchcommons.waikato.ac.nz/>

Research Commons at the University of Waikato

Copyright Statement:

The digital copy of this thesis is protected by the Copyright Act 1994 (New Zealand).

The thesis may be consulted by you, provided you comply with the provisions of the Act and the following conditions of use:

- Any use you make of these documents or images must be for research or private study purposes only, and you may not make them available to any other person.
- Authors control the copyright of their thesis. You will recognise the author's right to be identified as the author of the thesis, and due acknowledgement will be made to the author where appropriate.
- You will obtain the author's permission before publishing any material from the thesis.

A detailed characterisation of the wave climate around
New Zealand and its variability

A thesis
submitted in fulfilment
of the requirements for the degree
of
Doctor of Philosophy in Earth Sciences
at
The University of Waikato
by
VICTOR AZEVEDO GODOI



THE UNIVERSITY OF
WAIKATO
Te Whare Wānanga o Waikato

2018

*"Once you realize that the road is the goal and that you are always on the road,
not to reach a goal, but to enjoy its beauty and its wisdom, life ceases to be a task
and becomes natural and simple, in itself an ecstasy"*

Sri Nisargadatta Maharaj

ABSTRACT

Ocean waves can cause severe social and economic impacts. Therefore, understanding their behaviour is of paramount importance for the effective management of coastal and ocean hazards. This thesis thoroughly investigates four aspects (described below) of the wave climate around New Zealand and its variability by using 44 years (1958–2001) of wave hindcast data. These data were provided by the National Institute of Water and Atmospheric Research Ltd, and were produced using the WAVEWATCH III model forced with wind and ice fields from the ERA-40 reanalysis project.

Relationships between mean wave parameters (significant wave height (H_s), peak and mean wave periods, and peak wave direction) and several climate patterns were analysed. Climate indices representative of the Pacific Decadal Oscillation (PDO), El Niño–Southern Oscillation (ENSO), Indian Ocean Dipole (IOD), Zonal Wavenumber-3 Pattern (ZW3), and Southern Annular Mode (SAM) were correlated with the mean wave parameters using the Pearson’s correlation coefficient and the wavelet spectral analysis. Moreover, mean annual and inter-annual variabilities and trends in H_s were computed for the 44-year period. In general, larger annual and inter-annual variabilities were found along the coastline, in regions dominated by local winds. An increasing trend in H_s was found around the country, with values varying between 1 and 6 cm/decade at the shoreline. The largest trends in H_s were detected to the south of 48°S, suggesting a relationship with the trend toward a positive SAM. The wave parameters showed a strong connection with seasonal to decadal variabilities in the SAM throughout the period analysed. In addition, larger waves were observed during extreme ENSO and IOD events at inter-annual timescales, while they were more evident at intra-seasonal and seasonal timescales in the correlations with the ZW3. Negative phases of the ZW3 and ENSO and positive phases of the IOD, PDO, and SAM were associated with larger waves around most parts of New Zealand.

A detailed climatology of extreme wave events for New Zealand waters was also established, and estimates of H_s for up to 100-year return periods were

calculated. Although comparisons to buoy data at three locations around New Zealand showed negative biases in the hindcast data, the latter still provided a suitable basis for trend, spatial distribution, and frequency analyses. Results indicate some similarities to patterns previously shown in the mean wave climate, with the largest waves found in southern New Zealand, and the smallest ones observed in areas sheltered from southwesterly swells. The number of extreme events varied substantially throughout the year for the period 1958–2001, while their intensity was more consistent. Extreme events occurred more/less frequently in winter/summer months. The greatest mean annual variability of extreme H_s was found on the north coasts of both the North and South Islands, where more locally-generated storms drive the extremes. The inter-annual variability was largest along the north coast of the country and on the east coast of the South Island, suggesting relationships with La Niña-like effects and the SAM, respectively. Furthermore, the known trend for a more positive SAM may explain the increasing number of extreme events on the south and east coasts observed in trend analysis.

Clusters of storm waves contribute disproportionately to coastal erosion hazards because the coastline has insufficient time to recover between events. The change in occurrence of clustered storms and its association with atmospheric oscillation modes were also investigated in New Zealand waters. In order to do so, long-term averages of cluster parameters (number of storms within the cluster, potential for coastal erosion, and cluster duration) were firstly assessed. Then, the relationships between clustering and the ENSO, IOD, ZW3, PDO, and SAM were explored through correlation analysis over several timescales. Clusters were more frequently observed to the northeast of New Zealand and on the central eastern coast of the South Island. The most vulnerable regions to cluster-induced coastal erosion were southern New Zealand and the northwestern coast, which resulted from steady southwesterly swells, although clusters with the longest duration occurred on the east coast of the South Island. Trends suggest that clusters have incorporated more storms, have become more hazardous, and have increased in duration, particularly along the South Island coastline. Although these trends may be sensitive to the reanalysed wind fields used to force the wave hindcast, they

reflect trends in the ENSO, PDO, and SAM. Stronger southwesterly winds during El Niño (negative ENSO) and El Niño-like conditions (positive IOD/PDO) generated more clustered storms mainly on the southwestern coast of New Zealand, whereas increases in clustering were observed on the north coast during La Niña and La Niña-like conditions (stronger northeasterly winds). Higher occurrence of clustering was also evident on the west coast during the strong atmospheric zonal flow associated with negative ZW3. Lastly, strengthened westerlies related to positive SAM led to increased clustering primarily to the south of New Zealand.

The last aspect of the wave climate around New Zealand explored in this thesis was the modulation of H_s variability by wind anomalies associated with the co-occurrence of the Madden-Julian Oscillation (MJO) and ENSO. For this purpose, H_s and wind anomalies composites were created using 23 years (1979–2002) of the wave hindcast data and ERA-40 winds. Composites were calculated for November–March periods, when simultaneous ENSO-MJO phase pairs are potentially most active. Results showed striking features: El Niño-related wave conditions (which consist of increased H_s along the west and south coasts of New Zealand) are reinforced during MJO phase 8, whereas the wave conditions associated with La Niña (which consist of larger H_s along the north coast) are enhanced during MJO phase 6; Similar wave anomalies are generated during opposing ENSO phases (La Niña and El Niño) when these are combined with MJO phases 3 and 5, respectively; The majority of statistically significant H_s anomalies disappear from the study area during El Niño-MJO phase 6 and La Niña-MJO phase 4, showing the neutralising nature of some phase combinations; Lastly, negative H_s anomalies are experienced during El Niño-MJO phase 4, in contrast to the positive anomalies expected during El Niño events. These results clearly show the importance of remote forcing to wave anomalies in the New Zealand region and highlight the need to assess atmospheric and oceanic conditions considering multiple climate oscillations.

This thesis has shown that the wave climate around New Zealand is affected by a range of atmospheric conditions, which have significantly different impacts along the coastline. All these conditions should be taken into account in order to mitigate future hazards. Therefore, the results presented here may assist coastal

communities and stakeholders as well as offshore activities around the country in better prepare for potential impacts. Additionally, these results contribute to enhancing the research community knowledge of wave climatology in an area with recognised importance for regulating climate changes.

PREFACE

The main body of this thesis comprises four research chapters (chapters 2–5), which either have been published or are under review in peer-reviewed scientific journals. I was responsible for the data processing, data analysis, and writing. The wave hindcast data used in this thesis was generated by Dr Richard Gorman, from the National Institute of Water and Atmospheric Research Ltd (NIWA). Unless otherwise referenced, the information in this thesis was produced from my own ideas, and all work presented was conducted under the guidance and supervision of Professor Karin Bryan and Dr Richard Gorman. Dr Scott Stephens, from NIWA, and Dr Felipe de Andrade, from Centro de Previsão de Tempo e Estudos Climáticos – Instituto Nacional de Pesquisas Espaciais (CPTEC–INPE), also guided me in Chapters 3 and 5, respectively.

Chapter 2 has been published in *Journal of Geophysical Research: Oceans* (2016), volume 121(6), under the title “Regional influence of climate patterns on the wave climate of the southwestern Pacific: The New Zealand region”, by VA Godoi, KR Bryan, and RM Gorman.

Chapter 3 has been published in *Ocean Modelling* (2017), volume 117C, under the title “Extreme waves in New Zealand waters”, by VA Godoi, KR Bryan, SA Stephens, and RM Gorman.

Chapter 4 has been accepted for publication and is in press in the *International Journal of Climatology*, under the title “Storm wave clustering around New Zealand and its connection to climatic patterns”, by VA Godoi, KR Bryan, and RM Gorman.

Chapter 5 has been submitted for peer review to the *International Journal of Climatology*, under the title “Regional-scale ocean wave variability associated with ENSO-MJO combined activity”, by VA Godoi, FM de Andrade, KR Bryan, and RM Gorman.

ACKNOWLEDGEMENTS

Fortunately, many people accompanied me throughout this PhD journey, which was very encouraging and made the bumps along the way rather smooth. I am very thankful to:

- My parents, Valéria Lima and Ivan Godoi, for their immense and unconditional support, patience, and love.
- Carrie Riley for the great moments we shared throughout these years, which certainly made me happier and helped me carry on.
- My supervisors, Professor Karin Bryan and Dr Richard Gorman, for excellent discussions and all the support that led me to the end of this journey.
- Dr Scott Stephens for the help with extreme value analysis and for valuable suggestions during the development of Chapter 3.
- My friend Felipe Marques for suggesting the topic of and contributing with great comments to my last PhD paper, as well as for providing valuable comments on my climate analyses.
- My friend Ricardo Campos for the great guidance on the implementation of extreme value approaches.
- The technicians Dirk Immenga, Dean Sandwell, and Chris Morcom, who I had the enjoyable opportunity to spend some time with in the field.
- All of those who I had the pleasure of sharing the office with (Alex Port, Shawn Harrison, Stephen Hunt, Mareike Hoehne, Mariana Cussioli, Justin Walker, Peter de Ruiten, Bradley Monahan, Ben Norris, Ben Stewart, VV Hemanth, John Montgomery, Thomas Sailour, and Hiue Nguyen; special thanks to Bérengère Déjeans for her friendship and amazing food and coffee).
- The lunch and tea breaks team (Erik Horstman, Nicola Lovett, and Paola Salinas), the German-side Intercoast students (David Gehrmeier, Florian Boxberg, Sandy Boehnert, Susanne Coers, Tobias Kulgemeyer, Marine Le Minor, Anja Singer, Merle Bollen, Christina Gawrych, Linda Schumacher, Manuela Biondo, Robert Roskoden, and Brice Blossier), and the Bio crew (Rebecca Gallagher, Tarn Drylie, Clarisse

Niemand, Emily Douglas, Steph Mangan, Vera Rullens, and Tom Moore) for great and relaxing conversations.

- My Raglan-Brazilian friends (Rafael Soutelino, Juliana Miranda, Rafael Guedes, Phellipe Couto, Vanessa Barbosa, Henrique Rapizo, Andre Lobato, and Sabrina Nart) for keeping our culture alive with long BBQs and feijoadas and amazing times.

- All my family and friends in Brazil for making my trips back home so special.

- Vicki Smith, Gloria Edwards, and Fiona Martin for their help with bureaucratic stuff.

- Coordenação de Aperfeiçoamento de Pessoal de Nível Superior (CAPES) for financial support.

- The University of Waikato for providing funding for conference travel through the Terry Healy Memorial Award.

- The python community for knowledge sharing.

- Dr Marilyn Raphael, NOAA, ECMWF, JAMSTEC, BAS, JMA, and BoM for making their data freely available.

- The ocean waves (last but not least!) for making my personal and professional lives so exciting and happy.

TABLE OF CONTENTS

ABSTRACT	v
PREFACE	ix
ACKNOWLEDGEMENTS.....	xi
LIST OF SYMBOLS	xv
LIST OF ACRONYMS AND ABBREVIATIONS.....	xix
LIST OF FIGURES.....	xxi
LIST OF TABLES.....	xxix
CHAPTER 1: General introduction	1
1.1 Background and introduction.....	1
CHAPTER 2: Relationships between the mean wave climate around New Zealand and climate patterns.....	11
2.1 Introduction	11
2.2 Atmospheric oscillation modes.....	14
2.3 Wave model hindcast.....	16
2.4 Data preparation.....	19
2.5 Significant wave height variability.....	20
2.6 Relationships between the wave parameters and the climate patterns.....	23
2.6.1 Correlation analysis.....	23
2.6.2 Cluster and wavelet analyses.....	29
2.7 Conclusions.....	42
CHAPTER 3: The extreme wave climate around New Zealand	49
3.1 Introduction	49
3.2 Dataset.....	51
3.3 Extreme wave climatology	55

3.4 Extreme value analysis	65
3.5 Discussion.....	73
3.6 Conclusion.....	75
CHAPTER 4: Relationships between storm wave clustering conditions around New Zealand and climate patterns.....	79
4.1 Introduction	79
4.2 Methodology.....	82
4.3 Overview of storm wave clustering around New Zealand	90
4.4 Association between climate patterns and storm wave clustering	97
4.5 Conclusions.....	110
CHAPTER 5: Response of the wave climate around New Zealand to wind conditions associated with ENSO-MJO combined activity	115
5.1 Introduction	115
5.2 Datasets and methodology	118
5.3 Results and Discussion	120
<i>5.3.1 Composites for active ENSO with MJO phases.....</i>	<i>123</i>
<i>5.3.2 Composites for ENSO neutral with MJO phases.....</i>	<i>128</i>
<i>5.3.3 ENSO-MJO combined activity versus MJO activity.....</i>	<i>129</i>
5.4 Conclusions.....	130
CHAPTER 6: Summary	133
REFERENCES.....	137

LIST OF SYMBOLS

c_g	wave group velocity
d	mean water depth
D	storm duration
D_p	peak wave direction
g	gravitational acceleration
H_s	significant wave height
H_{smax}	storm peak H_s value
i	value of H_s above the 95 th percentile during the storm
I_d	index of dispersion
j	year
k	wavenumber
\mathbf{k}	wavenumber vector
m	coordinate perpendicular to the wave direction (θ)
n	number of records
N	wave action density spectrum
p	time period (years)
r	index of the record
R	radius of the Earth
S	sources and sinks of energy for the wave action density spectrum
t	time

T_{mean}	mean wave period from variance spectral density inverse frequency moment
T_{m-01}	mean wave period from variance spectral density 1st frequency moment
T_{m-02}	mean wave period from variance spectral density 2nd frequency moment
T_{m-10}	same as T_{mean}
T_p	peak wave period
U	depth- and time- averaged current velocity
U_λ	longitudinal component of the current velocity
U_ϕ	latitudinal component of the current velocity
v	total number of H_s values above the 95 th percentile during the storm
x	time series of significant wave height
Δt	temporal resolution
ΔT	time interval between storm peaks
$\langle \Delta T \rangle$	mean interval between storm peaks
θ	wave direction
λ	longitude
ρ	mass density of sea water
σ	relative frequency
ϕ	latitude
$44H_s$	44-year mean annual maxima H_s
$44T_{mean}$	44-year average of T_{mean} values corresponding to $44H_s$

$90thH_s$

ninetieth percentile H_s

LIST OF ACRONYMS AND ABBREVIATIONS

AAO	Antarctic Oscillation
AM	Annual maxima
AOI	Antarctic Oscillation Index
BAS	British Antarctic Survey
BoM	Australian Bureau of Meteorology
CDF	Cumulative distribution function
CFSR	Climate Forecast System Reanalysis
CSE	Cumulative storm energy
DIA	Discrete interaction approximation
DMI	Dipole Mode Index
ECMWF	European Centre for Medium-Range Weather Forecasts
ENSO	El Niño–Southern Oscillation
EOF	Empirical orthogonal functions
GEV	Generalised extreme value
GPD	Generalised Pareto distribution
IAV	Inter-annual variability
IOD	Indian Ocean Dipole
JAMSTEC	Japan Agency for Marine–Earth Science and Technology
JMA	Japan Meteorological Agency
JONSWAP	Joint North Sea Wave Project
MAV	Mean annual variability

MJO	Madden-Julian Oscillation
NDBC	National Data Buoy Center
NGDC	National Geophysical Data Center
NIWA	National Institute of Water and Atmospheric Research Ltd
NOAA	National Oceanic and Atmospheric Administration
ONI	Oceanic Niño Index
PDF	Probability density function
PNA	Pacific-North American
POT	Peaks-Over-Threshold
PSA	Pacific-South American
R	Pearson's correlation coefficient
RMM	Real-time multivariate
RMSE	Root-mean-square error
SAM	Southern Annular Mode
SAMI	Southern Annular Mode Index
SI	Scatter index
SLP	Sea level pressure
SOI	Southern Oscillation Index
SPI	Storm power index
SST	Sea surface temperature
SWC	Storm wave cluster
ZW3	Zonal Wavenumber-3 Pattern
45WH	45-year wave hindcast

LIST OF FIGURES

- Figure 2.1.** Grid domains used in the 45-year wave hindcast. (Left) Global domain. The area delineated by the green square represents the regional domain, which is expanded in the right plot. AI, CI, M, and O stand for Auckland Islands, Chatham Islands, Mokau, and Ohiwa, respectively, mentioned later in the text. Pink (non-directional measurements obtained) and blue (directional measurements obtained) dots represent the sites of the buoys used for validating the hindcast..... 18
- Figure 2.2.** (a) Mean annual variability (MAV) of significant wave height; (b) inter-annual variability (IAV) of significant wave height; (c) 44-year (1958–2001) trend in significant wave height (only statistically significant values at the 95% confidence level are plotted). Note that the colour scales are different to better represent the parameters. 22
- Figure 2.3.** Correlation coefficients (in percentage) of the (first column) SAMI and (second column) SOI with the wave parameters (rows) for the period 1958–2001. Correlations of the wave parameters with the (third column) ZW3 index comprise the period 1979–2001. Red/blue contours represent positive/negative correlations. Statistically significance within 95% is represented by light grey colour..... 24
- Figure 2.4.** Correlation coefficients (in percentage) of the PDO index and DMI (columns) with the wave parameters (rows) for the period 1958–2001. Red/blue contours represent positive/negative correlations. Statistically significance within 95% is represented by light grey colour..... 28
- Figure 2.5.** (a) Results of the cluster analysis. Each colour represents one cluster. The black dots represent the geographical coordinates where time series of the wave parameters were extracted to be used in the wavelet analysis; (b) 44-year (1958–2001) average of significant wave height. 31
- Figure 2.6.** Squared wavelet coherence spectra of significant wave height with the: (a) DMI and (b) SOI. The 90% confidence levels are represented by thick contours, and hatched areas represent the cone-of-influence. In phase and anti-phase signals are represented by arrows pointing upward and downward, respectively. Arrows

pointing rightward represent climate patterns preceding H_s , whereas the converse is true for arrows pointing leftward. The letters N, W, E, and S, on top of each plot, stand for northern, western, eastern, and southern clusters, respectively..... 33

Figure 2.7. Squared wavelet coherence spectra of significant wave height with the: (a) SAMI and (b) ZW3 index. The 90% confidence levels are represented by thick contours, and hatched areas represent the cone-of-influence. In phase and anti-phase signals are represented by arrows pointing upward and downward, respectively. Arrows pointing rightward represent climate patterns preceding H_s , whereas the converse is true for arrows pointing leftward. The letters N, W, E, and S, on top of each plot, stand for northern, western, eastern, and southern clusters, respectively..... 37

Figure 2.8. Squared wavelet coherence spectra of significant wave height with the PDO index. The 90% confidence levels are represented by thick contours, and hatched areas represent the cone-of-influence. In phase and anti-phase signals are represented by arrows pointing upward and downward, respectively. Arrows pointing rightward represent climate patterns preceding H_s , whereas the converse is true for arrows pointing leftward. The letters N, W, E, and S, on top of each plot, stand for northern, western, eastern, and southern clusters, respectively..... 38

Figure 2.9. (top) Normalised anomalies of the climate indices with their corresponding (bottom) power spectra: (a) SAMI, (b) ZW3 index, (c) SOI, (d) DMI, and (e) PDO index. The 95% confidence levels are represented by thick contours, and hatched areas represent the cone-of-influence..... 41

Figure 3.1. Regional grid domain of the 45-year wave hindcast. Green dots represent the model grid points on the 50 m isobath, whereas crosses indicate the buoy locations. NI and SI stand for North Island and South Island, respectively. . 52

Figure 3.2. Forty-four year (1958–2001) mean (a) annual maxima significant wave height; (b) mean wave period associated with annual maxima significant wave height. 57

Figure 3.3. Cluster analysis results using 44-year (1958–2001) averages of annual maxima H_s and corresponding mean wave periods (a) 4 clusters; (b) 5 clusters. Each colour represents one cluster..... 58

Figure 3.4. Annual average number of extreme wave events at the model grid points on the 50 m isobath (calculated using POT data).	59
Figure 3.5. Monthly climatology of extreme H_s calculated using POT data on the 50 m isobath.....	61
Figure 3.6. Monthly climatology of the number of extreme wave events calculated using POT data on the 50 m isobath.....	62
Figure 3.7. (a) Mean annual variability of extreme H_s ; (b) Inter-annual variability of extreme H_s . Both statistics were calculated using POT data on the 50 m isobath.	63
Figure 3.8. Monotonic trends in (a) annual maxima H_s ; (b) the annual average extreme H_s ; (c) the number of extreme wave events. Trends in (a) were computed for the whole regional domain of the 45-year wave hindcast, whereas in (b) and (c) they were calculated using POT data on the 50 m isobath. Only statistically significant values at the 95% confidence level were plotted. Significance was computed using p -value.....	65
Figure 3.9. Quantile-Quantile comparison of H_s return values for 100-year return period estimated using both the Annual Maxima-Generalised Extreme Value Distribution (AM-GEV) and Peaks-Over-Threshold-Generalised Pareto Distribution (POT-GPD) approaches. Return values were estimated at the model grid points on the 50 m isobath. R and RMSE (m) stand for Pearson’s correlation coefficient and root-mean-square error, respectively.	68
Figure 3.10. Significant wave height return values for 100-year return period (a) estimated at the model grid points on the 50 m isobath using the Peaks-Over-Threshold-Generalised Pareto Distribution approach; (b) estimated for the whole regional domain using the Annual Maxima-Generalised Extreme Value Distribution approach.	69
Figure 3.11. Validation of modelled significant wave height peaks during overlapping periods with buoy data for Baring Head (black circles), Banks Peninsula (green diamonds) and Maui (grey squares). Basic statistics (Pearson’s correlation coefficient (R), bias in meters, root-mean-square error (RMSE) in meters, and scatter index (SI)) were calculated according to Durrant <i>et al.</i> (2009).	71

Figure 3.12. Significant wave height return values (solid lines) estimated from the buoy (black) and model (red) data (H_s peaks from independent storms above the 99th percentile) for (a) Baring Head; (b) Banks Peninsula; (c) Maui. Dashed lines represent confidence intervals at the 95% level estimated from the asymptotic covariance matrix of the maximum likelihood estimators. Dots represent the data plotted in their Gringorten plotting positions (Gringorten, 1963).....72

Figure 4.1. Regional domain of the 45-year (1957–2002) wave hindcast. Filled circles represent the locations used in the wavelet spectral analysis. Filled squares A and B indicate the sites used as examples for showing time series of occurrence of clustered storms in Figure 4.2b and 4.2c, respectively. Grey dots illustrate the model grid points on the 200 m isobath, with the filled triangle marking the first point (0) of the sequence of Figure 4.2a. Dashed lines represent coastline delimiters, plotted here as a guide for Figure 4.2a. NI and SI stand for North Island and South Island, respectively.83

Figure 4.2. (a) Statistics computed for time series of storm wave occurrence at the 418 model grid points on the 200 m isobath: half of the index of dispersion of time intervals between storm peaks (dashed line), mean interval between storm peaks (solid line), and standard deviation of the time interval between storm peaks (dotted line). Vertical lines A and B mark the largest and smallest differences between the mean interval between storm peaks and half of the index of dispersion; the locations of the model grid points associated with these differences are displayed in Figure 4.1 as A and B. W, N, E, and S stand for west, north, east, and south, respectively, delimited according to Figure 4.1. Shaded and non-shaded areas of the graph comprise the model grid points along each section of the coastline (W: 0-143; N: 144-216; E: 217-375; S: 376-417), with 0 being located on the southwestern coast (triangle in Figure 4.1) and the subsequent numbers follow a clockwise rotation; (b) Time series of occurrence of storms and clustered storms at site A; (c) Time series of occurrence of storms and clustered storms at site B. Grey circles represent storm waves, whereas black circles indicate storm waves pertaining to clusters.....87

Figure 4.3. Considering the period 1958–2001: (a) annual average number of storm wave clusters; (b) average storm wave cluster duration. The averages were calculated at the model grid points on the 200 m isobath.91

Figure 4.4. Measures of the potential for cluster-induced coastal erosion: (a) average storm power index per cluster (in hecto m²h); (b) average cumulative storm energy per cluster (in mega Jh/m²). The averages were calculated using all storm wave clusters occurred during the period 1958–2001 for each model grid point on the 200 m isobath.....92

Figure 4.5. Monotonic trends in storm wave cluster parameters, calculated for the pre-satellite period (1958–1978, left column), satellite period (1979–2001, middle column), and long-term period (1958–2001, right column). Top row: cumulative storm energy (in kilo Jh/m²); middle row: cluster duration; bottom row: number of storms within the cluster. Trends were calculated from annual averages of the cluster parameters using the Mann-Kendall test and the Theil-Sen estimator. Only statistically significant values at the 95% confidence level (calculated using *p*-value) are displayed.94

Figure 4.6. Monotonic trends in normalised anomalies of climate indices: Southern Annular Mode index (SAMI), Zonal Wavenumber-3 Pattern (ZW3) index, Southern Oscillation Index (SOI), Dipole mode Index (DMI), and Pacific Decadal Oscillation (PDO) index. The anomalies of climate indices were normalised by the standard deviation. Trends were computed for the period 1979–2001 for the ZW3 index, and for the period 1958–2001 for the other indices. **S95%** and **NS95%** stand for statistically significant and non-significant at the 95% confidence level, respectively.97

Figure 4.7. Correlations of monthly anomalies between storm cluster indices and climate indices. Correlations were carried out at the model grid points on the 200 m isobath over the period 1958–2001 for the SAMI, SOI, DMI, and PDO index, and over the period 1979–2001 for the ZW3 index. Only statistically significant values at the 95% confidence level are displayed.....100

Figure 4.8. Correlations of seasonally-averaged monthly anomalies between storm cluster indices and climate indices lagged by one season. Correlations were carried

out at the model grid points on the 200 m isobath over the period 1958–2001 for the SAMI, SOI, DMI, and PDO index, and over the period 1979–2001 for the ZW3 index. Only statistically significant values at the 95% confidence level are displayed.

.....102

Figure 4.9. Correlations of annually-averaged monthly anomalies between cumulative storm energy per cluster and climate indices. Correlations were carried out at the model grid points on the 200 m isobath over the period 1958–2001 for the SAMI, SOI, DMI, and PDO index, and over the period 1979–2001 for the ZW3 index. Only statistically significant values at the 95% confidence level are displayed.

.....104

Figure 4.10. Correlations of annually-averaged monthly anomalies between storm cluster duration and climate indices. Correlations were carried out at the model grid points on the 200 m isobath over the period 1958–2001 for the SAMI, SOI, DMI, and PDO index, and over the period 1979–2001 for the ZW3 index. Only statistically significant values at the 95% confidence level are displayed.....105

Figure 4.11. Correlations of annually-averaged monthly anomalies between the number of storms within the cluster and climate indices. Correlations were carried out at the model grid points on the 200 m isobath over the period 1958–2001 for the SAMI, SOI, DMI, and PDO index, and over the period 1979–2001 for the ZW3 index. Only statistically significant values at the 95% confidence level are displayed.

.....106

Figure 4.12. Squared wavelet coherence spectra of monthly anomalies of storm cluster indices with monthly anomalies of the SOI. Thick contours represent 90% confidence levels, while hatched areas represent the cone-of-influence. In phase and anti-phase signals are represented by arrows pointing upward and downward, respectively. Arrows pointing rightward represent the ENSO preceding storm wave clusters, whereas the converse is true for arrows pointing leftward. The letters N, W, E, and S on top of each plot stand for north, west, east, and south coasts, respectively.....108

Figure 5.1. Wind at 10 m daily anomaly composites for El Niño with MJO phases over the November–March season during the period 1979–2002. Only statistically

significant anomalies at the 95% confidence level are displayed. Statistical significance was calculated using Student's t-test.....121

Figure 5.2. Wind at 10 m daily anomaly composites for La Niña with MJO phases over the November–March season during the period 1979–2002. Only statistically significant anomalies at the 95% confidence level are displayed. Statistical significance was calculated using Student's t-test.....122

Figure 5.3. Wind at 10 m daily anomaly composites for ENSO neutral with MJO phases over the November–March season during the period 1979–2002. Only statistically significant anomalies at the 95% confidence level are displayed. Statistical significance was calculated using Student's t-test.123

Figure 5.4. Significant wave height daily anomaly composites for El Niño with MJO phases over the November–March season during the period 1979–2002. Only statistically significant anomalies at the 95% confidence level are displayed. Statistical significance was calculated using Student's t-test.124

Figure 5.5. Significant wave height daily anomaly composites for La Niña with MJO phases over the November–March season during the period 1979–2002. Only statistically significant anomalies at the 95% confidence level are displayed. Statistical significance was calculated using Student's t-test.127

Figure 5.6. Significant wave height daily anomaly composites for ENSO neutral with MJO phases over the November–March season during the period 1979–2002. Only statistically significant anomalies at the 95% confidence level are displayed. Statistical significance was calculated using Student's t-test.129

LIST OF TABLES

Table 1.1. Inter-comparison between the 45WH, ECMWF, Chawla <i>et al.</i> (2013), and Durrant <i>et al.</i> (2014) wave hindcasts. Validations were carried out using a set of buoy measurements from the National Data Buoy Center data archive. RMSE and SI stand for root-mean-square error and scatter index (= RMSE normalised by the measured mean value), respectively.....	6
Table 2.1. Correlation coefficients among the climate indices for the period 1958–2001 ^a	42
Table 3.1. Buoy deployments. NIWA stands for National Institute of Water and Atmospheric Research Ltd.....	55
Table 5.1. Number of days in each ENSO-MJO phase pair over the November–March season during the period 1979–2002.	120

CHAPTER 1: General introduction

1.1 Background and introduction

Waves are fascinating. They have attracted human attention and have played a significant role in human lives for centuries. Historically, being able to interpret meteorological conditions and relate them to forthcoming sea states were key factors in our ability to colonise new lands and survive long ocean crossings. During wars, the threshold between winning a battle and losing a lot of lives was also directly associated with the knowledge of wave conditions. Wave-related research received substantial funds during and after the Second World War, leading to renowned studies like those of Munk *et al.* (1963) and Snodgrass *et al.* (1966). Nowadays, many daily activities continue to depend on the sea state, such as fishing, people and goods transportation, and water sports practice. Furthermore, the safety of coastal and offshore structures requires understanding of the long-term average wave behaviour (Young *et al.*, 2012; Godoi *et al.*, 2016, 2017), the so-called “wave climate”. Waves have also been found to be an important alternative energy source (Cruz, 2008; Reguero *et al.*, 2015) to support the needs of a consistently growing population. Climate changes (Domingues *et al.*, 2008; Rapp, 2008; Rind, 2008; Yamada *et al.*, 2010) reinforce the need to update our understanding of atmospheric and oceanic processes continuously. Therefore, understanding the wave climate and its fluctuations and trends is critical to adapt to a climate-changing world.

Wave climate is characterised by long-term statistics of a set of wave parameters (Holthuijsen, 2007). Several wave parameters (e.g., significant wave height, mean wave period, and mean wave direction) should be analysed in order to describe the wave climate satisfactorily. Nonetheless, the analysis is usually limited to the significant wave height (Holthuijsen, 2007). The analysis of the wave climate should be carried out according to the application (e.g., design of marine structures or assessment of wave energy potential). The latter determines whether

temporally averaged wave fields should be examined in terms of monthly, seasonal, or longer timescale means.

Wave climate has been assessed mainly through the analysis of buoy measurements (e.g., Bromirski *et al.*, 2005; Gemmrich *et al.*, 2011; Ruggiero *et al.*, 2010; Rapizo *et al.*, 2015), satellite altimetry data (e.g., Young, 1994, 1999; Chen *et al.*, 2002; Woolf *et al.*, 2002; Young *et al.*, 2011), and wave hindcast results (e.g., Cox and Swail, 2001; Sterl and Caires, 2005; Hemer *et al.*, 2010; Stopa *et al.*, 2013), all of which have advantages and limitations. Buoy measurements are generally taken as ground truth (Hemer, 2010) because they provide the most reliable records, especially when dealing with extreme values (Menéndez *et al.*, 2008). However, significant errors might be present in buoy data depending on the method used to compute wave heights. For example, Bender *et al.* (2010) investigated four different means of computing wave heights using data from a buoy in the Mississippi Sound recorded during Hurricane Katrina. The authors concluded that wave heights are overestimated by 26%, on average, and up to 56% during the hurricane peak when using the most widely used method for a buoy with a strapped-down 1D accelerometer. Moreover, the limited number of buoys precludes a spatial assessment of the wave climate in many regions of the globe. On the other hand, satellite altimetry data have satisfactory spatial coverage for many purposes, but the frequency with which data are collected is inadequate for establishing, for instance, an extreme wave climatology; a particular location is typically re-visited by a satellite every 10 days (Sterl and Caires, 2005). Wave hindcast results are alternative datasets to deal with spatial and temporal coverage difficulties, although they are generally less accurate than buoy and satellite data.

In general, long-term wave hindcasts are carried out using reanalysed wind fields. Although more and more wind measurements have been collected and reanalysis datasets have improved considerably over the time, most reanalysed wind fields still do not account for abrupt changes in wind direction and intense wind speed gradients because of their relatively low space-time resolution. This leads to insufficient energy input by the wind in the wave modelling, resulting in an underestimation of the largest waves (Caires and Sterl, 2003). Additionally, the

quality of wave hindcast results can be impacted by the physics of the numerical model, especially by source term parameterisations (Stopa *et al.*, 2016). Despite these issues, wave hindcast results are widely used to characterise wave climates all over the world (e.g., Sterl *et al.*, 1998; Sterl and Caires, 2005; Hemer *et al.*, 2010; Semedo *et al.*, 2011) and represent a powerful tool to evaluate, in a relatively short timeframe, the wave dynamics at several temporal and spatial scales.

State-of-the-art full discrete spectral models for generation, propagation, and dissipation of wind-generated waves (e.g., WW3DG, 2016 – first developed by Tolman (1991)) are governed by the random phase spectral action density balance equation for wavenumber-direction spectra (Mei *et al.*, 2005; WW3DG, 2016), described as:

$$\frac{dN}{dt} = \frac{S}{\sigma} \quad (1.1)$$

where d/dt ($t = \text{time}$) describes the total rate of change of the wave action density spectrum N , which in turn is a function of the wavenumber k and direction θ (perpendicular to the wave crest); σ is the relative frequency, which is observed in a frame of reference moving with the mean current; and S represents sources and sinks of energy for the spectrum. In numerical modelling, it is generally reasonable to consider only wind-wave interactions, nonlinear wave-wave interactions, and wave-ocean interactions (dissipation through whitecapping) as sources and sinks of energy in deep-water applications (Tolman, 1991). In shallow waters, other processes should be taken into account, as for example, wave-bottom interactions, depth-induced breaking, and triad wave-wave interactions (WW3DG, 2016). Although the wave model used to generate the hindcast results employed in this thesis parameterises shallow water wave propagation effects, the spatial resolution adopted in the simulation does not allow precise representation of such effects. Although the energy (variance) of the wave train is not conserved in the presence of currents, the wave action, defined as the wave energy over the relative frequency, is a conserved quantity (Bretherton and Garrett, 1969). This makes the wave action

density spectrum suitable for describing the wave propagation within a spectral model.

An Eulerian form of Equation (1.1) is needed when waves are numerically modelled, and this is represented, in spherical coordinates (WW3DG, 2016), as:

$$\frac{\partial N}{\partial t} + \frac{1}{\cos \phi} \frac{\partial}{\partial \phi} \dot{\phi} N \cos \theta + \frac{\partial}{\partial \lambda} \dot{\lambda} N + \frac{\partial}{\partial k} \dot{k} N + \frac{\partial}{\partial \theta} \dot{\theta}_g N = \frac{S}{\sigma} \quad (1.2)$$

$$\dot{\phi} = \frac{c_g \cos \theta + U_\phi}{R} \quad (1.3)$$

$$\dot{\lambda} = \frac{c_g \sin \theta + U_\lambda}{R \cos \phi} \quad (1.4)$$

$$\dot{\theta}_g = \dot{\theta} - \frac{c_g \tan \phi \cos \theta}{R} \quad (1.5)$$

$$\dot{\theta} = -\frac{1}{k} \left(\frac{\partial \sigma}{\partial d} \frac{\partial d}{\partial m} - \mathbf{k} \cdot \frac{\partial \mathbf{U}}{\partial m} \right) \quad (1.6)$$

where ϕ and λ represent latitude and longitude, respectively; c_g is the group velocity (velocity of the wave energy); U_ϕ and U_λ are components of the current velocity; R is the radius of the Earth; d is the mean water depth; m is a coordinate perpendicular to θ ; \mathbf{k} is the wavenumber vector (same direction as θ); and \mathbf{U} is the (depth- and time- averaged) current velocity. In short, Equations (1.2)–(1.6) are used to describe the wave propagation as a function of wavenumber, wave direction, position in space, and time. These equations constitute the basic set of formulations implemented in the numerical model used to generate the hindcast data employed in the present research.

The aforementioned hindcast data were produced by Dr Richard Gorman (Gorman *et al.*, 2010), from the National Institute of Water and Atmospheric Research Ltd (NIWA), by using version 3.14 (Tolman, 2009) of the WAVEWATCH III model (Tolman, 1991). The wave hindcast (henceforth 45WH) is 45 years long (September 1957 – August 2002) and is focused on the New Zealand region, my study area. A proper description of the 45WH is provided in the next section. The 45WH differs from other well-known wave hindcasts (e.g., Chawla *et al.*, 2013;

Durrant *et al.*, 2014) in some respects (briefly listed below), but the main one is the spatial resolution around New Zealand ($0.125^\circ \times 0.09375^\circ$ (~ 10 km) for the 45WH).

Chawla *et al.* (2013) and Durrant *et al.* (2014) used the same wave model as the one implemented in the 45WH, and generated results at spatial resolutions of 0.5° and 0.4° , respectively, for the New Zealand region. Durrant *et al.* (2014), nevertheless, used a newer version (4.08) of the WAVEWATCH III and adopted the source term package of Ardhuin *et al.* (2010), whereas the source term package of Tolman and Chalikov (1996) was selected for the Chawla *et al.* (2013) hindcast and the 45WH. Both hindcasts (Chawla *et al.* (2013) and Durrant *et al.* (2014)) cover a shorter period (1979–2009) than the 45WH, but were forced with higher-quality wind fields. On the other hand, the wave hindcast developed by the European Centre for Medium-Range Weather Forecasts (ECMWF) (Caires *et al.*, 2004; Sterl and Caires, 2005) covers the same period as the 45WH and was forced with the same wind fields. The ECMWF hindcast, nonetheless, was conducted using the WAM model (Komen *et al.*, 1994 – originally developed by WAMDI (1988)), which was implemented with a considerably coarser spatial resolution ($1.5^\circ \times 1.5^\circ$) than the 45WH. With the exception of the ECMWF hindcast, whose results were generated for the common synoptic hours (00, 06, 12, 18 UTC), the other three hindcasts produced hourly data.

The wind fields used to force the 45WH and the ECMWF hindcast were sourced from the ERA-40 reanalysis (Uppala *et al.*, 2005), and have spatial and temporal resolutions of 1.125° and 6 h, respectively. One of the main limitations of ERA-40 wind fields is related to the data shortage in the Southern Hemisphere during the pre-satellite era (period before 1979). A distinct temporal inhomogeneity is observed in the amount of data assimilated by the atmospheric model used to generate the ERA-40 reanalysis with the introduction of satellite data (Bromwich and Fogt, 2004). This inhomogeneity can be problematic when assessing trends in the reanalysed winds and, consequently, in the products generated using these wind fields. Moreover, ERA-40 winds have been found to underestimate speeds above 14 m/s (Caires *et al.*, 2004), with obvious consequences for the high percentile wave heights. The underprediction of the

largest waves by hindcasts that used ERA-40 winds as boundary conditions has been reported by a number of authors (e.g., Caires and Sterl, 2003; Caires *et al.*, 2004). The Chawla *et al.* (2013) and Durrant *et al.* (2014) hindcasts were forced with winds obtained from the Climate Forecast System Reanalysis (CFSR) (Saha *et al.*, 2010), which provides wind fields with spatial and temporal resolutions of $\sim 0.3^\circ$ and 1h, respectively. These winds are not free from problems either. Stronger winds are overpredicted in the Southern Hemisphere prior to 1994 (Chawla *et al.*, 2013), which is likely related to changes in wind observations assimilated in the CFSR atmospheric model. Such overprediction has been shown to lead to an overprediction in ocean waves as well (Chawla *et al.*, 2013). Another discontinuity in the CFSR wind speed over the Southern Hemisphere was observed in 2006 (Chawla *et al.*, 2013; Stopa *et al.*, 2013). Therefore, both ERA-40 and CFSR wind fields have problems that affect the New Zealand region directly.

Statistical comparisons between the performances of those four wave hindcasts have been carried out by Dr Richard Gorman (personal communication) and are summarised in Table 1.1.

Table 1.1. Inter-comparison between the 45WH, ECMWF, Chawla *et al.* (2013), and Durrant *et al.* (2014) wave hindcasts. Validations were carried out using a set of buoy measurements from the National Data Buoy Center data archive. RMSE and SI stand for root-mean-square error and scatter index (= RMSE normalised by the measured mean value), respectively.

	<u>Significant wave height</u>			<u>Peak wave period</u>		
	Bias	RMSE	SI	Bias	RMSE	SI
45WH	-0.22 m	0.49 m	0.25	-0.18 s	2.47 s	0.28
ECMWF	-0.19 m	0.49 m	0.21	-	-	-
Chawla <i>et al.</i> (2013)	0.16 m	0.41 m	0.19	-	-	-
Durrant <i>et al.</i> (2014)	-0.02 m	0.37 m	0.18	0.64 s	2.53 s	0.26

The values presented in Table 1.1 correspond to averages computed across the buoys from the National Data Buoy Center (NDBC) included in the validation of all four hindcasts. These buoys are all located in the Northern Hemisphere, mainly along the USA coastline (Figure 2.1 – chapter 2). Unfortunately, an inter-

comparison of those hindcasts for the New Zealand region was not possible using buoy measurements. Differences in the validation statistics between the hindcasts can be chiefly attributed to the quality of wind fields used to force the wave model and to the source term parameterisations employed in each simulation. Further discussion is provided in chapter 3 for the 45WH. Additional details on the wave hindcasts discussed can be found in the quoted studies. More information on the 45WH and its validation is provided throughout this thesis. Regarding wave hindcast datasets produced prior to the ECMWF one, Caires *et al.* (2004) present an inter-comparison of four wave reanalyses. Their findings include the identification of long-term trends in all reanalysis datasets and worse data quality in the Southern Hemisphere than in the Northern Hemisphere. The latter results from the lack of measurements in the Southern Hemisphere during the pre-satellite era. Reguero *et al.* (2012) briefly describe some wave reanalysis datasets developed in the past, and present a calibrated global wave reanalysis (GOW). According to the authors, GOW is supposed to provide the longest (since 1948) wave dataset for the analysis of global wave climate variability in addition to being updated periodically.

Although Table 1.1 shows that the other hindcasts generally performed better than the 45WH for the specific set of locations selected (where an inter-comparison was possible), the 45WH was chosen for three reasons: 1) the spatial resolution of its results around New Zealand; 2) its relatively long record; 3) and the possibility of collaborating with NIWA researchers, who have contributed to the sustainable management of New Zealand natural resources for more than 20 years. The 45WH data allow a thorough investigation of the New Zealand wave climate, which, surprisingly, has been analysed carefully in just a few studies (e.g., Laing, 2000; Gorman *et al.*, 2003b – Their findings are reported in the introduction of Chapter 2). New Zealand is located in the mid-latitudes of the Southern Hemisphere, about 166°–179°E and 34°–48°S, and its landmass sits in the prevailing westerly winds (Drost *et al.*, 2007). Different types of atmospheric systems affect weather in the country, with tropical and subtropical cyclones having a greater impact on the northern regions, while extratropical cyclones affect the other areas

more. These transient atmospheric systems imply distinct wave conditions along the New Zealand coastline, and are components of long-term changes in the atmosphere (climate oscillations).

Wave climate comprises all possible sea states, from calm to extreme conditions, which are strongly influenced by atmospheric fluctuations at several timescales. The variability of wave conditions in response to those fluctuations depends on the exposure of the coastline to wave generation zones. Long wave records, with high space-time resolution, are required to investigate this variability climatologically. This thesis addresses such climatological variability within the New Zealand context, using hindcast data as the main research tool to describe its nature.

This thesis is composed of four main topics, all of which are inter-related through a common objective, to improve the knowledge of the wave climate around New Zealand. Specifically, I aim to contribute to a more detailed understanding of the following topics:

- Relationships between the mean wave climate around New Zealand and climate patterns (Chapter 2);
- Past and future behaviours of extreme waves around New Zealand (Chapter 3);
- Relationships between storm wave clustering conditions around New Zealand and climate patterns (Chapter 4);
- Response of the wave climate around New Zealand to wind conditions resulting from the interaction of two specific climate oscillations whose main variabilities occur at different timescales (Chapter 5).

Chapters 2–5 describe how these objectives have been achieved and examine multiple aspects relevant to the full characterisation of the wave climate around New Zealand. Each chapter includes an introduction, methods, results and discussions, and conclusions. The association of the mean wave climate and storm clustering conditions around New Zealand with climate patterns was assessed using the Pearson's correlation coefficient, cluster analysis, and wavelets. Past and future extreme wave conditions were analysed by establishing an extreme wave climatology and employing two extreme value approaches, respectively. The wave

climate variability due to wind conditions associated with the interaction of two specific climate oscillations was examined using a compositing approach. Chapter 6 provides a summary of previous chapters and main contributions of this thesis, as well as suggests potential future work.

Contributions of the author and co-authors to Chapter 2

I was responsible for the data processing, data analysis, and writing. Karin R. Bryan and I came up with the idea of the topic addressed in this chapter. I defined the methodology employed.

Richard M. Gorman produced and validated the hindcast results employed in Chapter 2.

Karin R. Bryan and Richard M. Gorman reviewed Chapter 2 and made suggestions regarding the writing.

CHAPTER 2: Relationships between the mean wave climate around New Zealand and climate patterns

2.1 Introduction

Wave dynamics have a significant impact on human lives, particularly in island nations such as New Zealand. A wide variety of recreation, fishing and activities at sea require constant monitoring of the sea state. In nations with less established roading and rail networks, people rely on shipping trade between cities and depend on wave conditions to do so. Recently, waves have also been used as energy resource to supply power to coastal communities. Engineering specifications for coastal and offshore structures, for instance harbours and oil platforms, require a detailed understanding of wave conditions at building sites. The synthesis of wave conditions, based on long-term statistics, is scientifically known as “wave climate” (Sterl and Caires, 2005), and has been required for many purposes in addition to construction, such as evaluation of extreme wave heights, planning of naval and marine operations (Cox and Swail, 2001), wave energy estimation, and oil spills and sediment transport assessments. Amongst the information that can be extracted from a wave climatology, of particular interest is the relationship between atmospheric oscillation modes and the wave climate of a region. These modes can allow us to understand future trends in the nature of coastal hazards and may serve as proxies to understand potential effects of future climate change (Quan *et al.*, 2013).

Atmospheric oscillation modes can dramatically alter weather conditions and, as a consequence, the wave conditions. Some climate patterns have been shown to be influential on local scales, while others are known to impact on a wide range of regions (e.g., Hemer *et al.*, 2010; Harley *et al.*, 2010; Gorman *et al.*, 2003b) through “teleconnections”. The latter can be defined as remote influences on the variability of large-scale atmospheric and/or oceanic features (Grimm and Ambrizzi, 2009). Significant attention has been devoted to the impacts caused by climate patterns on ocean waves, especially in regions where severe storms play an

important role. Despite being located in a relatively isolated portion of the world, New Zealand is a particularly interesting case because it lies at the interface of the Southern and Pacific oceans and the Tasman Sea, and hence is influenced by a range of climatic drivers. The Southern Ocean has also been proven to be extremely important for regulating climate. By sinking and storing carbon dioxide and heat in deep waters, the Southern Ocean slows down global warming, minimising anthropogenic impacts (Lavergne *et al.*, 2014; Sallée *et al.*, 2012; Russell *et al.*, 2006). Therefore, there is general interest in the impact of climate oscillations on the properties of the Southern Ocean, and New Zealand plays a key role in controlling these properties (Chiswell *et al.*, 2015; Morris *et al.*, 2001) by changing the ocean dynamics in the area (e.g., by blocking and steering the flow) and influencing waves, currents and sea level. As a consequence, phenomena of global scales are directly affected by changes in the waters surrounding New Zealand (Sasaki *et al.*, 2008; Davis, 2005).

New Zealand's high-latitude location along with the long stretch of ocean lying immediately to the west of it provide a highly energetic wave environment (Gorman *et al.*, 2003b). Swell waves generated in the region just south of the country propagate through the Pacific Ocean and impact upon the west coasts of South America, Central America and part of the North America (Young, 1999). The long period of these swells and their seasonality are different from other more well studied areas, such as the North Atlantic, and so a greater understanding is essential for hazard management along South Pacific shipping routes, oil exploration, coastal engineering, and wave power generation. Estimates show substantial wave power potential within the New Zealand region (Rusu and Guedes Soares, 2009). Moreover, the Trans-Pacific Partnership will have a direct impact on trade of goods across the Pacific (World Bank Group, 2016), which will affect not only the 12 countries involved in the agreement, but also their trade partners, and thus increase pressure on south Pacific shipping routes.

Different methodologies have been applied to assess the wave climate around New Zealand. Pickrill and Mitchell (1979) used approximately 40 sources of data, including deep-water, mid-water and shore-based visual and buoy

observations, covering approximately 17 years. Laing (1993) implemented a second-generation wave model to perform a 5-month wave hindcast for the New Zealand region, which covered mainly the winter of 1989. In a subsequent study, Laing (2000) used approximately 13 years (1985–1998) of wave data derived from radar altimeters to create a wave climatology for the New Zealand waters. The coastal wave climate was assessed again in more detail by Gorman *et al.* (2003a, 2003b). The authors conducted a 20-year (1979–1998) deep-water wave hindcast and extracted boundary conditions from it to use as initial conditions for a shallow-water hindcast. All these authors found similar spatial patterns of significant wave height (H_s), where the south coast receives the highest energy waves, followed by the west, east and north coasts, respectively. Pickrill and Mitchell (1979) observed that the westerly air flow is responsible for generating the waves that impact on the south coast. Swell waves generated to the south also reach the east coast, which in turn, receives in addition locally-generated northerly and southerly storm waves. The west coast receives southerly swells and locally-generated westerly and southerly storm waves. Finally, the north coast is dominated by northeasterly waves. Some of the most intense storm conditions were observed to occur in the summer months as a result of tropical cyclones (Gorman *et al.*, 2003a). Increasing wave heights off the northeast coast of the North Island occur during La Niña events (Gorman *et al.*, 2003b). In contrast, the rest of the country experiences increasing wave heights during El Niño events (Gorman *et al.*, 2003b). Laing (1993) also verified that monthly anomalies of mean H_s seem to be associated with El Niño events in winter.

Extreme wave heights in southern Pacific, especially in the New Zealand region, are modulated by positive phases of the Antarctic Oscillation and Indian Ocean Dipole (Izaguirre *et al.*, 2011). According to Caires *et al.* (2006), significant increases of extreme H_s are expected around the southern half of New Zealand in the austral winter. On the basis of the 20-year hindcast produced by Gorman *et al.* (2003a), Stephens and Gorman (2006) estimated extreme H_s for the New Zealand region. The authors showed that the estimates follow the trend of the mean H_s ,

although they present less spatial variation. The smallest extreme H_s value (13.9 m) was observed in the northeast, and the largest (19.3 m) in the southwest.

In summary, preliminary studies have shown that the wave climate in the southwest Pacific is influenced by the state of climatic indicators, and the response around New Zealand is spatially variable (Godoi *et al.*, 2015), depending on the exposure of the coastline to generating regions. This chapter extends this previous work by describing the nature of the correlation, determining its timescale, and showing how the correlation depend on the local exposure of the coastline. In order to determine how atmospheric oscillations modulate the regional wave climate around New Zealand, mean wave parameters generated by a 45-year wave hindcast were used to conduct two main analyses. First, mean annual and inter-annual variabilities of H_s were calculated to understand which areas around the country are most susceptible to large variations in wave conditions, hence providing an indication of the most vulnerable areas to climate change. Then, time series of mean wave parameters were correlated with climate indices using a basic statistical tool, the Pearson's correlation coefficient, and a more sophisticated technique based on spectral energy, the wavelet analysis. The long timeframe of the analysis allows us to capture some of the longer timescale patterns and how these differ depending on exposure to the Southern Ocean in contrast to the South Pacific Ocean.

The chapter is organised as follows. The climate patterns that potentially influence the wave climate of New Zealand are briefly described in section 2.2. Details of the wave hindcast carried out to conduct the analyses are explained in section 2.3. Section 2.4 addresses the manipulation of the dataset used in the methodology of this chapter, which in turn is explained along with the discussion of the results in sections 2.5 and 2.6. Finally, the conclusions are presented in section 2.7.

2.2 Atmospheric oscillation modes

A number of atmospheric oscillation modes have been described in the literature, and at least five of them have been reported to somehow affect the

weather and/or the ocean in the southwest Pacific. These are the Pacific Decadal Oscillation (PDO), the El Niño–Southern Oscillation (ENSO), the Indian Ocean Dipole (IOD), the Zonal Wavenumber-3 Pattern (ZW3), and the Antarctic Oscillation (AAO), frequently called Southern Annular Mode (SAM) (Limpasuvan and Hartmann, 1999).

The PDO is an inter-decadal climate fluctuation identified by the leading empirical orthogonal function of monthly sea surface temperature (SST) anomalies over the North Pacific (Mantua *et al.*, 1997; Taylor *et al.*, 2009; Deser *et al.*, 2010). Only two cycles have been verified within the last century, with predominantly negative SST anomaly between 1947 and 1976, and predominantly positive SST anomaly between 1925 and 1946, and after 1977 (Mantua *et al.*, 1997).

Like the PDO, the ENSO is also characterised by SST anomalies (Zhang *et al.*, 1997). Its signatures are primarily observed over the equatorial region of the Pacific Ocean with inter-annual cycles that range from 2 to 7 years (Trenberth and Hurrell, 1994; Cane, 2005; Stopa *et al.*, 2013). The ENSO has been recognised by its influence on atmospheric and oceanic conditions all over the world as a result of the so-called “Atmospheric Bridge” (heat and moisture fluxes from the source region to remote areas – Alexander *et al.*, 2002). The ENSO is measured by the Southern Oscillation Index (SOI) (Ropelewski and Jones, 1987), which is the difference between the Darwin and Tahiti surface air pressures.

An inter-annual variability with dipole-shaped signature in the SST field over the tropical Indian Ocean defines the IOD (Saji *et al.*, 1999; Izumo *et al.*, 2010). This oscillation is measured by the Dipole Mode Index (DMI), which describes the difference in SST anomaly between the tropical western Indian Ocean and the tropical southeastern Indian Ocean. Extreme IOD events occurred in 1961, 1994, and 1997 (Cai *et al.*, 2014; Saji *et al.*, 1999), and despite its irregular cycle, the IOD seems to have strong cycles with periodicities of approximately 2 and 5 years (Webster *et al.*, 1999; Yuan and Cao, 2013).

The ZW3 is a quasi-stationary planetary wavenumber-3 pattern that significantly impacts on daily (Kidson, 1988), seasonal (Mo and White, 1985), and inter-annual (Trenberth, 1980; Karoly, 1989; Cai *et al.*, 1999) timescales at mid-

latitudes of the Southern Hemisphere (van Loon and Jenne, 1972; Raphael, 2004). It is normally identified by sea ice, sea level pressure (SLP), wind (Yuan and Li, 2008), and geopotential height fields (Mo and White, 1985). Indices for the ZW3 have been computed by different authors (e.g., Mo and White, 1985; Raphael, 2004) using mainly SLP and geopotential height values at three selected geographical points, which vary in accordance with the methodology adopted by each author.

Zonally symmetric anomalies of opposite signs in Antarctica and the mid-latitudes of the Southern Hemisphere define the SAM (Marshall, 2003). Such anomalies can be identified in several atmospheric fields, such as surface pressure and surface temperature, and they modulate phenomena at timescales that vary from high to low frequency. Noteworthy cycles of 2.7, 4.2, and 45.7 months were reported by Gong and Wang (1999), who defined an index to represent the SAM. The index is called Antarctic Oscillation Index (AOI) or Southern Annular Mode Index (SAMI), and measures the difference of zonal mean sea level pressure between 40°S and 65°S.

2.3 Wave model hindcast

A 45-year wave hindcast (September 1957 to August 2002), hereinafter 45WH, has been carried out using the WAVEWATCH III v. 3.14 model (Tolman, 2009). This is a third-generation wave model that solves the wave action density spectrum as a function of wavenumber and direction. Parameterisations of physical processes include wave growth and decay by wind stress, nonlinear resonant interactions, bottom friction, dissipation by whitecapping, surf-breaking, and scattering by wave-bottom interactions (Tolman, 2009). Refraction and straining of the wave field due to spatial variations of the mean water depth are included in the shallow-water governing equation.

In order to perform the simulation, 1-minute bathymetric results from the ETOPO1 1 arc-minute global relief model (Amante and Eakins, 2009) were implemented in the wave model to assign depths to oceans and seas, and delimit borders of continents, countries and islands. The ETOPO1 was developed by the National Geophysical Data Center (NGDC) and is aimed at supporting tsunami

forecasting, modelling and warning, and also ocean circulation modelling. Wind fields at 10 m and ice fields from the ERA-40 reanalysis dataset (Uppala *et al.*, 2005) were employed as boundary conditions in the 45WH. The ERA-40 was created by the European Centre for Medium-Range Weather Forecasts (ECMWF) and spans 45 years, from September 1957 to August 2002. It was produced by assimilating atmospheric and oceanographic observations from different sources, such as aircrafts, ocean buoys, ships, radiosondes, balloons, satellite-borne instruments and surface platforms. The ERA-40 products used in the 45WH have temporal resolution of 6 h and spatial resolution of 1.125° .

The evolution of the directional wave spectrum was computed by using two one-way nested numerical grids (Figure 2.1) with 25 logarithmically spaced frequencies and 24 equally spaced directions. The global grid covers latitudes 81°S – 81°N and longitudes 0°E – 358.875°E at 1.125° resolution, while the regional grid has spatial resolution of 0.125° in longitude and 0.09375° in latitude, and covers latitudes 51.75°S – 32.625°S and longitudes 162°E – 185.625°E . The bottom friction was represented by the Joint North Sea Wave Project (JONSWAP) parameterisation (Hasselmann *et al.*, 1973), and the Cavaleri and Malanotte-Rizzoli (1981) formulation assisted the improvement of the initial wave growth behavior from calm conditions. The formulation proposed by Tolman and Chalikov (1996) was used to compute input and dissipation terms, whereas the discrete interaction approximation (DIA) (Hasselmann *et al.*, 1985) was used in modelling nonlinear wave-wave interactions. Wind and ice fields were input every 6 h, and the output parameters were generated at 3 and 1 h intervals for the global and regional domains, respectively.

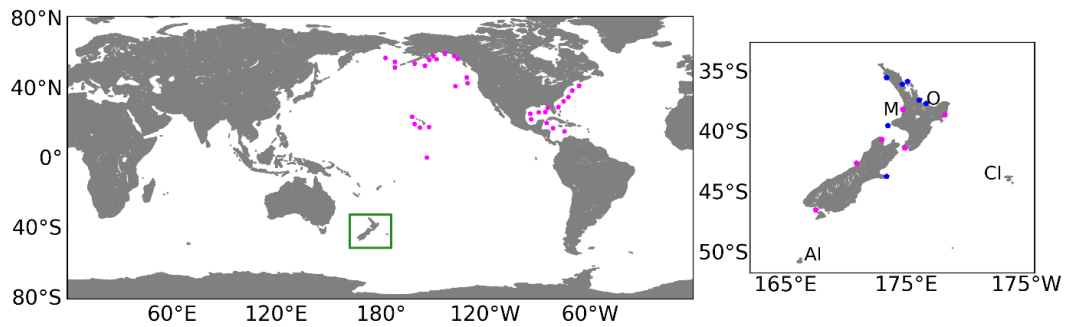


Figure 2.1. Grid domains used in the 45-year wave hindcast. (Left) Global domain. The area delineated by the green square represents the regional domain, which is expanded in the right plot. AI, CI, M, and O stand for Auckland Islands, Chatham Islands, Mokau, and Ohiwa, respectively, mentioned later in the text. Pink (non-directional measurements obtained) and blue (directional measurements obtained) dots represent the sites of the buoys used for validating the hindcast.

The 45WH has been validated with buoy and satellite measurements. Buoy records from the National Data Buoy Center (NDBC) and from stations around New Zealand (see Figure 2.1 for buoy locations) have been used to verify the accuracy of the hindcast. Several wave parameters were validated, including significant wave height, mean wave direction, directional spread, peak wave period, peak wave direction, and mean wave period (second moment), depending on what was available from each wave buoy. The statistical indices computed in the validation were the mean, standard deviation, bias, root-mean-square error (RMSE), scatter index and correlation coefficient. Satellite altimetry data in the New Zealand region were obtained from the TOPEX/Poseidon, ERS1 and ERS2 missions, and subject to a set of quality control procedures as detailed by Laing (2000) and summarised by Gorman *et al.* (2003b). First, the whole hindcast domain was divided into areas of $2.25^\circ \times 2.25^\circ$ for both satellite altimetry data and model results. Then, occurrence distributions of H_s within each of these bins were computed and compared over the available time period. Additionally, comparisons between altimetry data and global model results were performed by calculating H_s monthly means for all the values within each bin.

Results of the validation of modelled data against buoy and satellite measurements varied according to location and sea state. As a result of the

reasonably low spatial-temporal resolution of wind fields, which does not account for significantly strong velocity gradients and sudden changes in the wind direction, mean wave parameters were generally underestimated during extreme events. Despite this, the 45WH results are suitable for the purpose of the present chapter, since monthly averages have been used (as described in the next section) and results have been generated for a considerably long time period. Due to the coarse spatial resolution near the coast, the global hindcast presented better results at the NDBC buoys than at the New Zealand buoys. The RMSE from comparisons of measured and modelled H_s had values of 0.52 m, averaged over the NDBC buoys, and 0.61 m averaged over the New Zealand buoys, while the correlation coefficient from the same comparisons averaged 0.89 and 0.83 over the NDBC and New Zealand buoys, respectively. In the comparison with satellite data, the hindcast results underestimated H_s (with up to 0.5 m of negative bias) in the western Tasman Sea and near the New Zealand coast, whilst overestimation (with localised positive bias of order 0.5 m) was seen in the Southern Ocean. The latter was particularly more pronounced during the austral winter. Significant improvement was observed in the comparisons between the regional results and New Zealand buoy data, with mean RMSE of 0.50 m, and mean correlation of 0.83, obtained from H_s comparisons. Comparisons of the regional hindcast with satellite data showed a reduction in the magnitude of negative biases in the wave height near the New Zealand coast seen in the global hindcast. Additional details on the 45WH and its validation can be found in Gorman *et al.* (2010).

2.4 Data preparation

An overview of the wave climate can be obtained by computing monthly means over a long period of time. Monthly means of significant wave height (H_s), peak wave period (T_p), mean wave period (T_{mean}) and peak wave direction (D_p) were calculated over 44 years (1958–2001). Only the full calendar years covered by the 45WH were considered in the analysis, disregarding the years 1957 and 2002 due to incomplete data coverage.

According to Stopa *et al.* (2013), atmospheric oscillations have a more significant impact on extreme than on average conditions. Extreme conditions have distinct definitions depending on the author. Storlazzi *et al.* (2015), for example, define extreme significant wave height as the mean of the top 5% H_s within a specific period. On the other hand, Stopa *et al.* (2013) and Bosserelle *et al.* (2012) use the mean of the top 10% H_s . Young *et al.* (2011) assess trends in more extreme wave conditions considering the 90th and 99th percentiles. In this chapter, I use the ninetieth percentile as the threshold for determining monthly extreme significant wave heights ($90thH_s$) for the 44-year period.

The five wave parameters used in this chapter enable a comprehensive understanding of the wave climate around New Zealand. The wave period and wave direction associated with the most energetic waves are represented by T_p and D_p , respectively, while $90thH_s$ takes into consideration wave heights of extreme events (H_s and T_{mean} are more representative of mean wave conditions of the ocean).

Monthly means of the SOI, DMI, SAMI, PDO index, and ZW3 index were sourced from the National Oceanic and Atmospheric Administration (NOAA), Japan Agency for Marine-Earth Science and Technology (JAMSTEC), British Antarctic Survey (BAS), Japan Meteorological Agency (JMA), and Raphael (2004), respectively. The ZW3 index is only available from 1979 onwards, whereas the other indices cover the whole hindcast period. The anomalies of the climate indices were computed by subtracting their climatological monthly means from their monthly means. The same was done for the wave parameters in order to investigate how they are modulated by the climate modes.

2.5 Significant wave height variability

The mean annual variability (MAV) and inter-annual variability (IAV) of H_s were computed for each grid point of the regional domain over the 44-year period following the methodology described in Stopa *et al.* (2013). The MAV (Equation (2.1)) is defined as the average of the annual standard deviation normalised by the annual average, and the IAV (Equation (2.2)) is determined by the standard

deviation of the annual means normalised by the overall mean (Stopa *et al.*, 2013).

Thus, MAV and IAV can be written as:

$$MAV = \frac{1}{p} \sum_{j=1}^p \sqrt{\frac{1}{n} \sum_{r=1}^n \left[x_{jr} - \left(\frac{1}{n} \sum_{r=1}^n x_{jr} \right) \right]^2} \left(\frac{1}{n} \sum_{r=1}^n x_{jr} \right)^{-1} \quad (2.1)$$

IAV =

$$\sqrt{\frac{1}{p} \sum_{j=1}^p \left\{ \left(\frac{1}{n} \sum_{r=1}^n x_{jr} \right) - \left[\frac{1}{p} \sum_{j=1}^p \left(\frac{1}{n} \sum_{r=1}^n x_{jr} \right) \right] \right\}^2} \left(\frac{1}{np} \sum_{j=1}^p \sum_{r=1}^n x_{jr} \right)^{-1} \quad (2.2)$$

where x is the time series of significant wave height over a period of p years with n records each, and j and r refer to the year and record, respectively.

Signatures of the wave climate of New Zealand can be clearly noted in the MAV and IAV maps (Figures 2.2a and 2.2b). Relatively large variability is observed in coastal areas, especially in sheltered regions dominated by locally-generated waves, such as to the north of both islands. This characteristic agrees with the works by Stopa *et al.* (2013) and Bosserelle *et al.* (2012), who conducted their studies for the whole globe and Western Australia, respectively. The large values in northerly-exposed regions are a consequence of the absence of steady southerly swells. The northern area experiences tropical cyclones, typically in summer, which contributes to relatively large MAV in that region (Figure 2.2a). As reported by Laing (2000), there is a larger difference between the mean and 99.9 percentile values to the north of the country, resulting in relatively large variability. The same northern region as well as the areas off the west and south coasts show higher IAV than the region off the east coast (Figure 2.2b), suggesting a stronger association of those areas with atmospheric oscillations that are characterised by inter-annual cycles. As previously mentioned, Gorman *et al.* (2003b) reported increasing wave heights off the northeast coast of the North Island during positive phases of the ENSO, and around the rest of the country during negative phases, especially off the southwest and south regions. In contrast to the IAV, the high frequency of southwesterly swells with nearly constant wave height in the west coast results in smaller MAV

(Figure 2.2a) at this coast in comparison to the east coast. Regarding deep-water regions, the area to the south of 45°S generally has larger IAV than most regions to the north of this parallel (Figure 2.2b), which indicates a possible relation with the SAM. As cited by Marshall (2003) and Kushner *et al.* (2001), a trend toward the positive phase of the SAM has been detected by several works, leading to strengthening of westerly winds in the Southern Ocean. Finally, the fluctuations of H_s throughout the seasons produce generally higher values in the MAV than in the IAV, highlighting the prevalence of high-frequency oscillations in the wave climate variability.

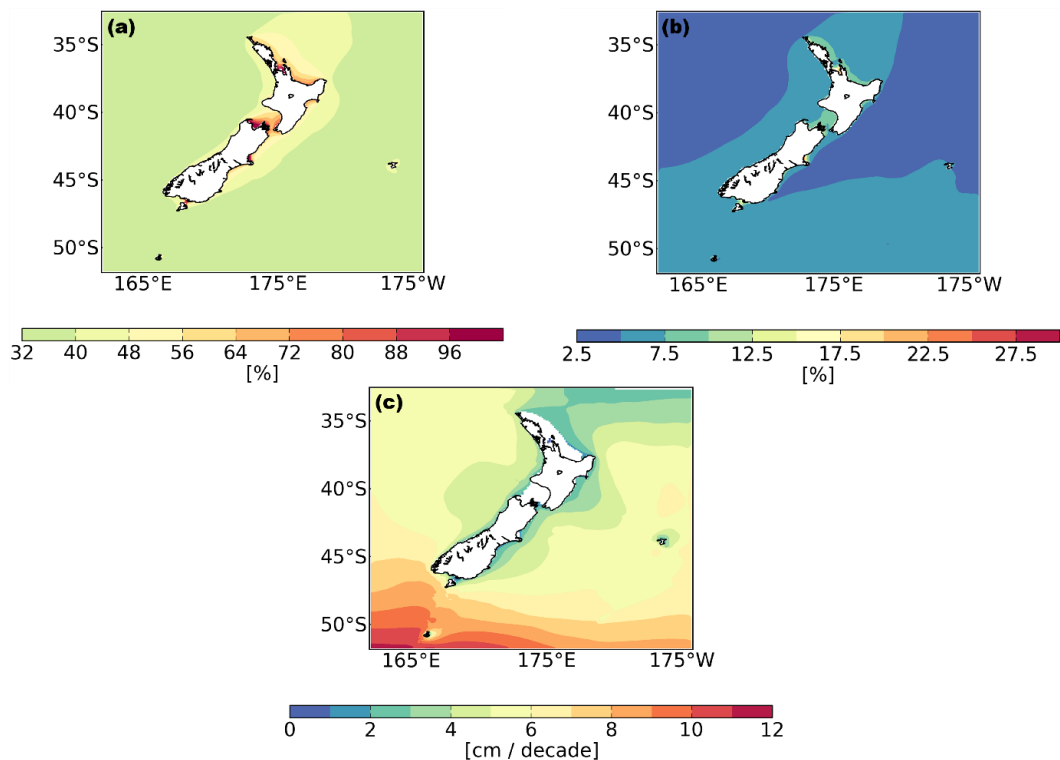


Figure 2.2. (a) Mean annual variability (MAV) of significant wave height; (b) inter-annual variability (IAV) of significant wave height; (c) 44-year (1958–2001) trend in significant wave height (only statistically significant values at the 95% confidence level are plotted). Note that the colour scales are different to better represent the parameters.

To complement the MAV and IAV results, the trend in H_s was computed for the period 1958–2001 (Figure 2.2c). This was carried out by fitting a linear curve to

H_s monthly means on each grid point of the regional domain using least-squares regression. Only statistically significant values at the 95% confidence levels are displayed, which excludes the regions immediately to the north of both islands where the largest MAV is found. The whole regional domain presents an increasing trend in H_s . The areas adjacent to the coastline have a positive trend that varies from values smaller than 1 cm/decade, in more sheltered sites, to 6 cm/decade in the southwest coast. The greatest trends, of up to 12 cm/decade, are observed to the south of 48°S, suggesting a relationship with the positive trend in the SAM. These results are consistent with the general trend of increasing H_s found by Coggins *et al.* (2015). Nevertheless, their results are more focused on offshore regions due to the coarser spatial and temporal resolutions in relation to the present dataset.

2.6 Relationships between the wave parameters and the climate patterns

2.6.1 Correlation analysis

Monthly anomalies of H_s , $90thH_s$, T_{mean} , T_p , and D_p fields were correlated with monthly anomalies of the SOI, SAMI, DMI, PDO index, and ZW3 index by computing the Pearson's correlation coefficient (R) for each grid point of the 45WH regional domain (Figures 2.3 and 2.4). The 95% confidence levels were used to determine statistically significant results, and are represented by shaded light grey in Figures 2.3 and 2.4. In view of the fact that all atmospheric oscillations assessed were derived from linear analyses, climate anomalies associated with cool phases oppose those of warm phases (Mantua and Hare, 2002).

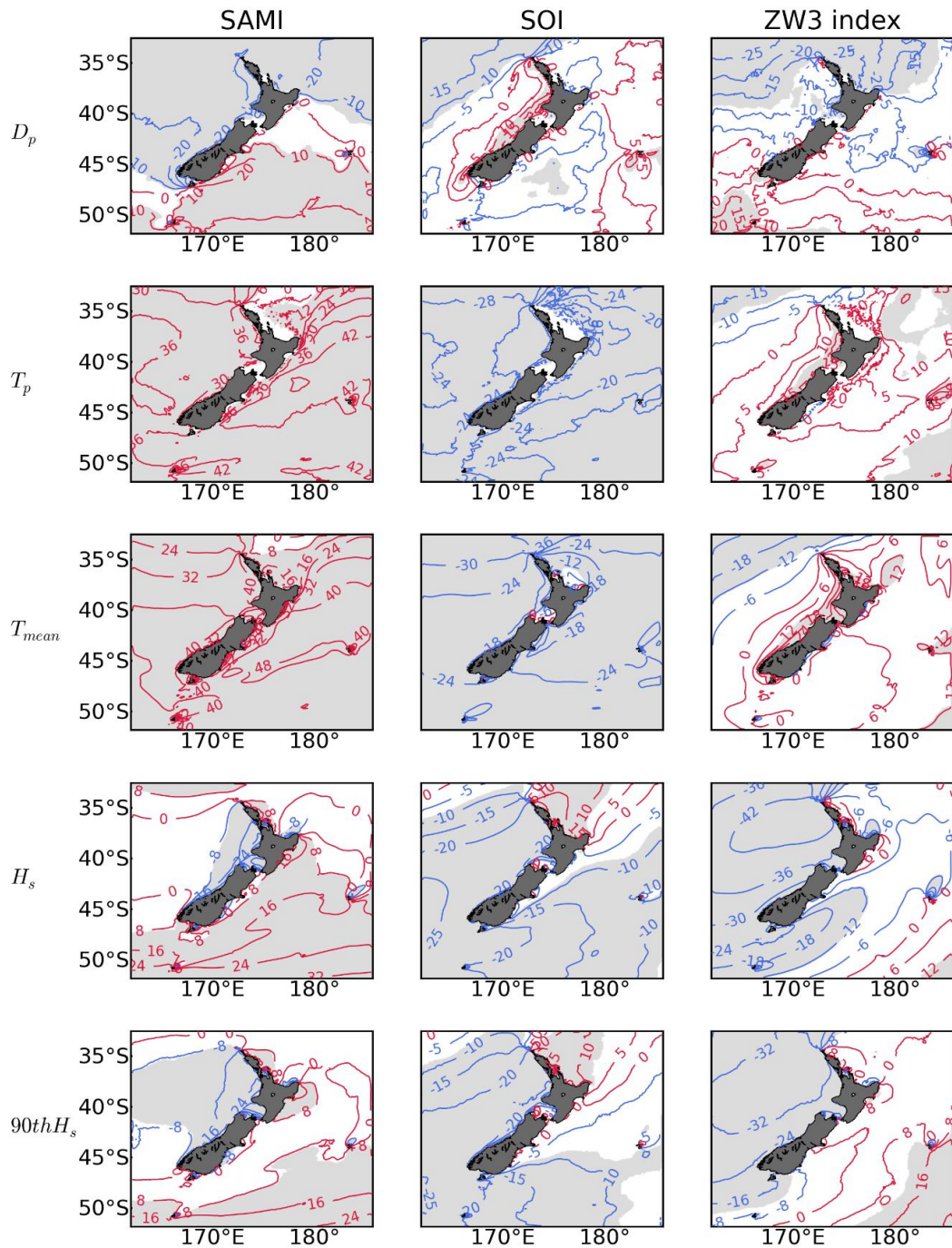


Figure 2.3. Correlation coefficients (in percentage) of the (first column) SAMI and (second column) SOI with the wave parameters (rows) for the period 1958–2001. Correlations of the wave parameters with the (third column) ZW3 index comprise the period 1979–2001. Red/blue contours represent positive/negative correlations. Statistically significance within 95% is represented by light grey colour.

The SAM is the prevailing mode to the south of New Zealand. The intensification of the SAM over recent decades (a trend toward its positive phase)

results in the strengthening of the circumpolar westerlies (Schott *et al.*, 2009; Marshall, 2003; Hemer, 2010; Gillett and Thompson, 2003), leading to larger wave heights (Hemer *et al.*, 2010; Bosserelle *et al.*, 2012) and longer wave periods (Figure 2.3). The trend toward the SAM positive phase has been occurring since the mid-1960s (Marshall, 2003), accompanied by a reduction in the number of cyclones south of 40°S, with greatest reductions near 60°S (Simmonds and Keay, 2000). Associated with such reductions are increases in the intensity of cyclones to the south of Australia, in the Tasman Sea, and in the central Pacific, in addition to decreases in the eastern portions of the Pacific and Indian Oceans (Simmonds and Keay, 2000). Moreover, a poleward shift of the extratropical cyclone storm tracks has also been observed as a result of the positive trend in the SAM (Gillett and Thompson, 2003). Hemer *et al.* (2010) reported a trend of counter-clockwise rotation in wave direction south of ~48°S during positive phases of the SAM. In contrast to this trend, one sees a clockwise rotation in D_p associated with positive anomalies in the SAMI in our results (Figure 2.3), which is represented by positive correlations. On the other hand, a counter-clockwise rotation in D_p , represented by negative correlations, is observed along and off the west and north coasts during the SAM positive phase. The SAM is associated with substantial changes in the wave parameters. Changes in D_p , T_p , and T_{mean} are observed in most parts of the regional domain, in H_s along most sectors of the coastline (the north coast is less affected), and in $90thH_s$ mostly along the west coast. In the case of T_p and T_{mean} , correlations indicate that longer wave periods are associated with increasing values of the SAMI.

Negative correlations of the SOI with H_s and $90thH_s$ are found all around the country's coastline, except to the north (Figure 2.3). This is in agreement with the studies of Gorman *et al.* (2003b) and Laing (2000), who observed increased occurrence of southwesterly winds around New Zealand during negative ENSO phases (El Niño). Accompanying increasing wave heights during El Niño events are increasing wave periods, as illustrated by negative correlations. During La Niña events (positive phases of the ENSO), increased occurrence of northeasterly winds in the northeast coast have been noted (Gordon, 1986; Gorman *et al.*, 2003b),

possibly as a result of an increasing number of cyclones in Australasia during such events (Sinclair *et al.*, 1997). Larger wave heights with shorter wave periods are observed to the north of New Zealand as a consequence of La Niña events. Both H_s and $90thH_s$ are positively correlated with the SOI in the region, while T_{mean} and T_p are negatively correlated. A possible explanation for the inverse relationship between increasing wave heights and decreasing wave periods would be the formation of shorter wave fetches resulting from storms that track more closely to the shore during cold ENSO conditions than during warm and neutral ENSO conditions. This explanation agrees with Revell and Goulter (1986), who verified that the origin points of tropical cyclones tend to be concentrated farther to the northeast with decreasing SOI. According to Hemer *et al.* (2010), there is a clockwise/counter-clockwise rotation in wave direction in the Tasman Sea and in the western Pacific Ocean during El Niño/La Niña events. In other words, since wave direction is predominantly southeasterly during both phases of the ENSO (Hemer *et al.*, 2010), southerly/easterly waves are more common during El Niño/La Niña events. Most areas around New Zealand show no statistically significant relationship between SOI and D_p . However, the rotation in wave direction noted by Hemer *et al.* (2010) agrees with our results in two out of the four regions where statistically significant correlations are observed. Negative correlations are present in the northwestern area of the regional domain and off the southeast coast of the South Island. On the other hand, the regions adjacent to the west coasts of both the North and South Islands and around the Chatham Islands show positively correlated values, in opposition to the study of Hemer *et al.* (2010). These differences might be related to the products used by the authors for generating their results. Satellite observations are of limited application to coastal waters as a result of the influence of land on the return signal (Gorman *et al.*, 2003a). In addition, the spatial resolutions of both satellite observations and model results used by Hemer *et al.* (2010) are coarser than the one used here, hampering a high-quality representation of coastal areas.

In the atmospheric circulation, the ridges of the planetary ZW3 wave have preferred locations of formation; these are over southern South America, southern

Indian Ocean, and southwest of New Zealand (Raphael, 2004; Garreaud and Battisti, 1999; Yuan *et al.*, 1999). Consequently, preferred locations for cyclogenesis are observed in the open ocean north of the ice cover (Yuan and Li, 2008). Negative correlations (Figure 2.3) of the ZW3 with H_s , $90thH_s$, and D_p are consistent with the zonal flow associated with negative phases of the ZW3. Conversely, the northward wind stress anomaly between southwest Australia and south of New Zealand (Cai *et al.*, 1999) suggests that smaller waves with a clockwise rotation propagate into the study area during positive phases of the ZW3. A strong meridional flow is associated with positive phases of the ZW3, and is more pronounced from Australia to South America (Raphael, 2004) due to the troughing of the ZW3 wave (generated by the presence of a low-pressure system) over the south Pacific. Positive correlations of T_{mean} and T_p with the ZW3 index indicate increasing wave periods as a result of stronger meridional flow, but they are statistically significant only along the west coast of New Zealand.

The PDO is not the most influential mode on any wave parameter around New Zealand. However, statistically significant positive correlations with T_{mean} and T_p are found in most parts of the regional domain (Figure 2.4). According to Mantua *et al.* (1997), the SOI is correlated with the PDO index, such that positive PDO tends to coincide with El Niño-like conditions. This explains increasing wave periods as well as increasing wave heights around the country, excepting to the north, during positive PDO. However, the correlations of wave height with the PDO index are statistically significant only along and off the west and south coasts of New Zealand. Despite not being statistically significant, the negative correlations of wave height and wave period with the PDO index to the north of the country are consistent with negative phases of the PDO, in which La Niña-like conditions are expected to occur in the region. Regarding wave direction, statistical significance is found mostly to the north and northwest of the country, with wave direction exhibiting a clockwise rotation pattern during positive PDO.

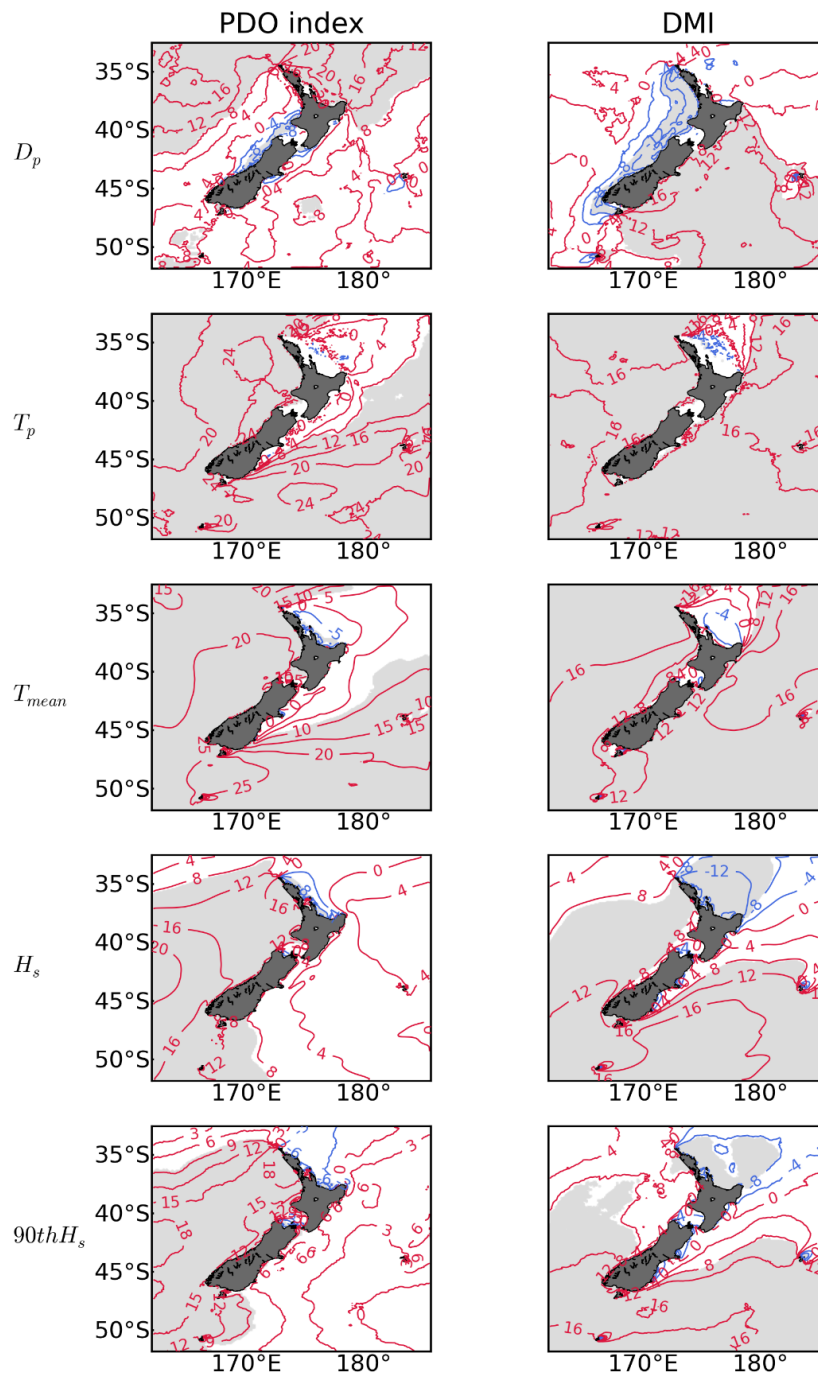


Figure 2.4. Correlation coefficients (in percentage) of the PDO index and DMI (columns) with the wave parameters (rows) for the period 1958–2001. Red/blue contours represent positive/negative correlations. Statistically significance within 95% is represented by light grey colour.

Like the PDO, the IOD does not seem to have a strong association with the wave parameters around New Zealand (Figure 2.4). According to Schott *et al.* (2009), the IOD can either self-generate or be externally triggered by the ENSO. The

opposite is also true, with the positive phase of the IOD often preceding positive phases of the ENSO (Izumo *et al.*, 2010). Signals of the IOD influencing the zonal winds over the Pacific Ocean were described by Izumo *et al.* (2010). This means that indirect effects of the IOD can take place through the effect of the ENSO, since the modes are correlated. The IOD is weak in most years (Schott *et al.*, 2009), presenting anti-cyclonic circulation at low levels during its positive phase (Yuan and Cao, 2013), easterly winds along the equator (Cai *et al.*, 2014; Webster *et al.*, 1999; Yuan and Cao, 2013), where weak westerlies normally prevail (Cai *et al.*, 2014; Webster *et al.*, 1999), and westerly flow near 30°S (Cai *et al.*, 2014). The most energetic waves of the world occur in the Southern Ocean between South Africa and Australia (Young, 1999), where the influence of the IOD is rarely addressed. Such energetic waves arrive on the west and south coasts of New Zealand as they propagate from the Indian Ocean to the South Pacific Ocean. Positive correlations of the DMI with T_{mean} , T_p , H_s , and $90thH_s$ are found in most parts of the regional domain (Figure 2.4), which agrees with the study of Izaguirre *et al.* (2011). The authors observed increasing extreme wave height in the southwestern Pacific during IOD positive phases. Negative correlations are found to the north of New Zealand for H_s and $90thH_s$, indicating decreases in the wave height during positive IOD and vice versa. This is consistent with the inverse relationship between the IOD and ENSO (shown later in Table 2.1 by the negative correlation between the DMI and SOI), in which conditions associated with negative IOD resemble La Niña conditions (positive ENSO). Lastly, a counter-clockwise rotation in D_p is observed along the west coast of the country, whereas the opposite rotation is observed along the east coast.

2.6.2 Cluster and wavelet analyses

According to Bell *et al.* (2000) and Goring and Bell (1999), quasi-periodic fluctuations that vary in both the magnitude and timescale, such as those under consideration here, require an analysis that is different from the traditional Fourier spectral analysis, which assumes stationarity. The wavelet technique has been used as an alternative for resolving non-stationary dominant modes of variability (Goring and Bell, 1999; Grinsted *et al.*, 2004). The wavelet power spectrum provides an indication of periods of time that most contribute to the dominant cycles, and is

obtained by taking the average of the square of the wavelet coefficients. The relationship between two variables is identified by the wavelet coherence spectrum.

To facilitate the wavelet spectral analysis, a subset of geographical locations was selected for examination. The selection was based on a cluster analysis conducted to divide the 45WH regional domain into subregions that encompass areas with similar wave climate. Pickrill and Mitchell (1979) identified four main wave climates around New Zealand. In order to be consistent with them, four clusters were employed here, each one being representative of each subregion (wave climate). Attempts using five and more clusters were also performed, but no significant gain in information was obtained. Forty-four years (1958–2001) of mean fields of H_s and T_{mean} were standardised to a Gaussian distribution (zero mean and unit variance) for the cluster analysis. The clustering was based on the k -means algorithm (Hartigan and Wong, 1979; Kanungo *et al.*, 2002; Likas *et al.*, 2003), which was executed 10 times with different initial centroid seeds using 300 iterations for each run.

The results of the cluster analysis (Figure 2.5a) agree with the spatial distribution of the four main wave climates described by Pickrill and Mitchell (1979). Interesting features of the 44-year average of significant wave height (Figure 2.5b) can be observed in the cluster analysis results. First, areas with distinct wave climates are clearly demarcated by each colour, roughly representing the four quadrants. Southwesterly swells propagate not only along the west coast of both islands but also along the south coast of the South Island. The shadowing to the north of the northern portion of New Zealand clearly shows the obstruction caused by the presence of landmasses, which prevents energetic southwesterly waves from reaching that region and, consequently, results in a less rough wave climate. The same occurs to the north of the Chatham and Auckland islands, located near the 45°S and 50°S parallels, respectively. Finally, the sectors immediately seaward of the east coast and between the North and South islands present a relatively moderate wave climate.

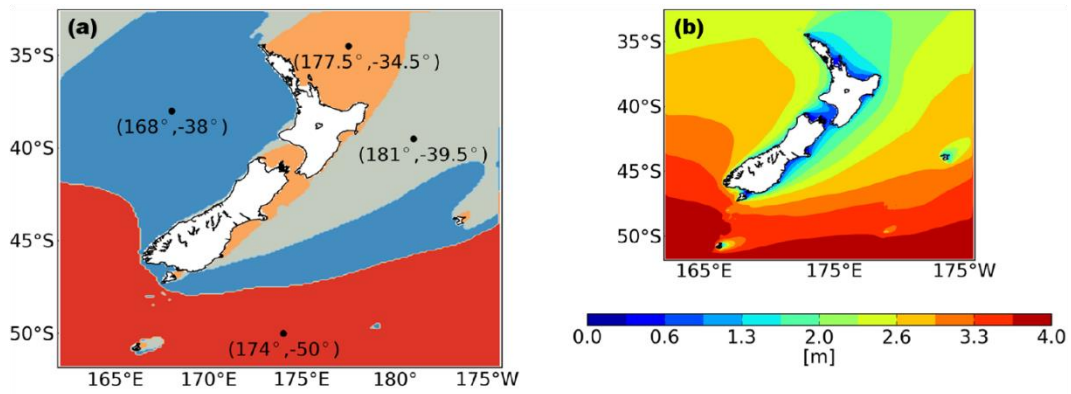


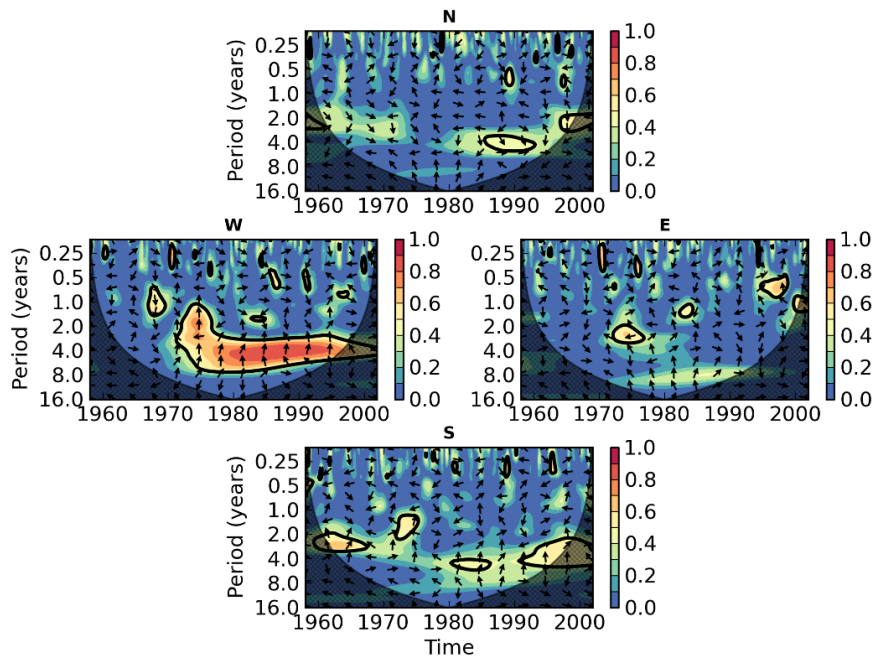
Figure 2.5. (a) Results of the cluster analysis. Each colour represents one cluster. The black dots represent the geographical coordinates where time series of the wave parameters were extracted to be used in the wavelet analysis; (b) 44-year (1958–2001) average of significant wave height.

Anomalies of the wave parameters were computed for the monthly time series extracted from the central geographical coordinate of each cluster (henceforth cluster), whose positions are 181°E/39.5°S, 177.5°E/34.5°S, 168°E/38°S, and 174°E/50°S (Figure 2.5a). In order to identify dominant modes of variability for each subregion, such anomalies were correlated with monthly anomalies of the climate indices by computing squared wavelet coherence spectra. Unreliable and less significant wavelet results can be produced if the probability density function (PDF) of geophysical time series is far from normally distributed (Grinsted *et al.*, 2004). Following Grinsted *et al.* (2004), this lack of normality can be addressed by transforming the time series of anomalies of the wave parameters into time series of percentiles. Then, both the wave parameters and climate indices were normalised by their standard deviation in order to have total energy equal to one at all scales. Finally, the wavelet technique was applied. Power spectra were calculated using the Morlet function with non-dimensional frequency equal to six for satisfying the admissibility condition (Farge, 1992). According to Grinsted *et al.* (2004), the Morlet wavelet is generally a good choice when using wavelets for feature extraction purposes, since it provides a good balance between time and frequency localisation. The authors recommend using the Morlet wavelet unless there are good grounds to do otherwise. Veltcheva and Guedes Soares (2015) state,

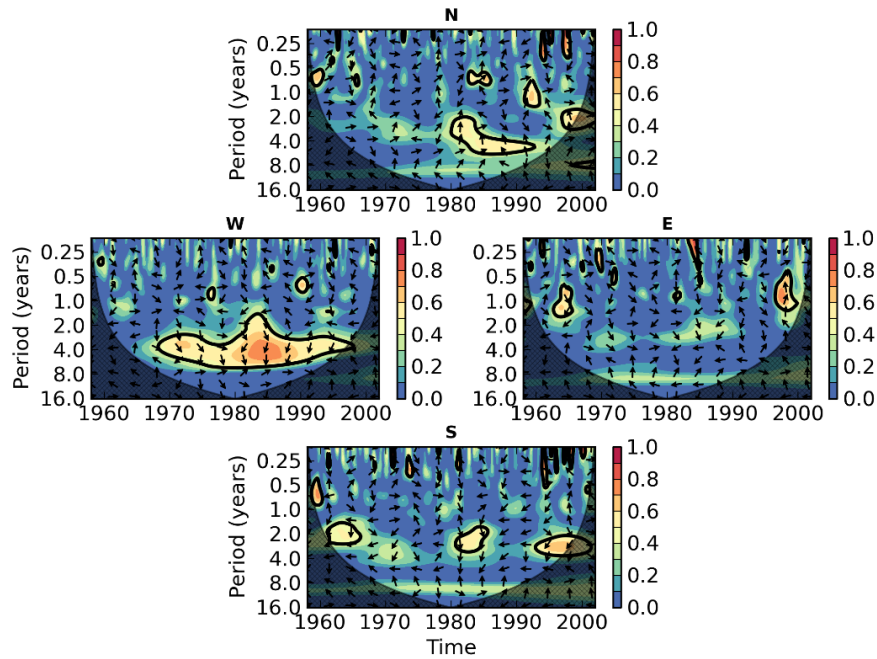
in addition, that the Morlet wavelet is appropriate for the wavelet analysis of wave data due to its oscillatory nature and the similarity between the Morlet scale parameter and Fourier period. Statistically significant signals were calculated using the chi-squared test for power spectra, since the wavelet power spectrum is chi-square distributed, and using 300 Monte Carlo simulations for coherence spectra. Significance at the 95% and 90% confidence levels were used for the power and coherence spectra, respectively. The cone-of-influence, where edge effects become important (Torrence and Compo, 1998), was computed for the purpose of dealing with errors at the beginning and end of the wavelet spectrum. Other studies in which wavelets have been used to analyse ocean waves include, for example, Liu (1994) and Massel (2001).

For a given time period, anomalies result from the combination of the signal in all frequencies, and for this reason, it is not trivial to account for the exact contribution of each atmospheric oscillation mode to the amplitudes of anomalies of the wave parameters.

The squared wavelet coherence spectra of H_s with the climate indices are displayed in Figures 2.6–2.8. Hatched areas represent the cone-of-influence, and 90% confidence levels are represented by thick contours. In phase and anti-phase signals are represented by arrows pointing upward and downward, respectively, while arrows pointing rightward represent climate patterns preceding H_s , and the converse is true for arrows pointing leftward. The graphics related to the ZW3 index (Figure 2.7b) range from 1979 to 2001 due to lack of data in previous periods.



(a)



(b)

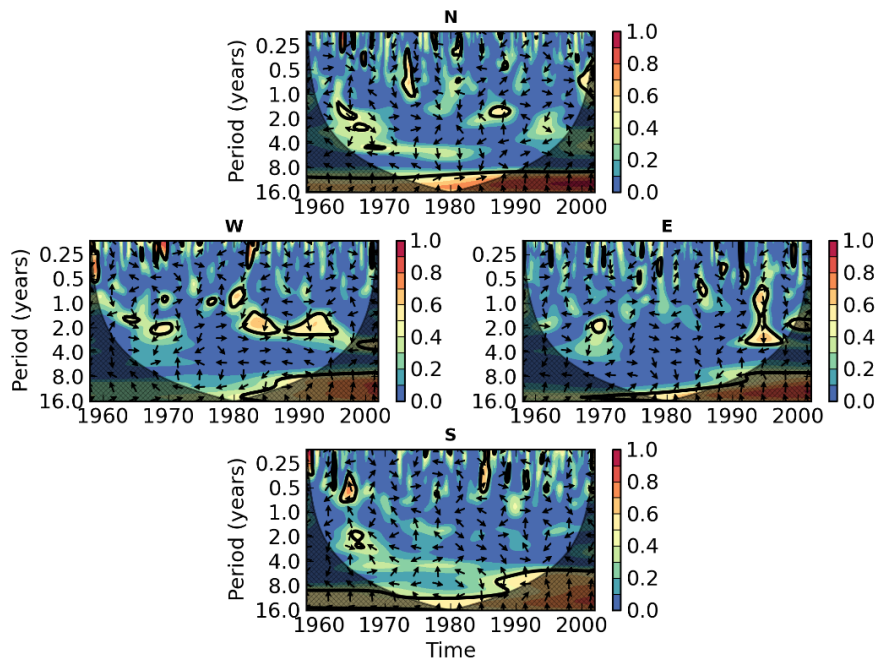
Figure 2.6. Squared wavelet coherence spectra of significant wave height with the: (a) DMI and (b) SOI. The 90% confidence levels are represented by thick contours, and hatched areas represent the cone-of-influence. In phase and anti-phase signals are represented by arrows pointing upward and downward, respectively. Arrows pointing rightward represent climate patterns preceding H_s , whereas the converse is true for arrows pointing leftward. The letters N, W, E, and S, on top of each plot, stand for northern, western, eastern, and southern clusters, respectively.

H_s was most affected by IOD and ENSO cycles in the western cluster (Figure 2.6). Significant correlations with the DMI (Figure 2.6a) and SOI (Figure 2.6b), at periodicities ranging from approximately 2 to 7 years, were observed in the western cluster from the late 1960s to the early 2000s. In general, positive/negative phases of the IOD/ENSO were accompanied by large waves (positive anomalies in H_s) in the western cluster during this period, as indicated by upward/downward arrows in Figures 2.6a and 2.6b. This pattern can also be noted in the southern cluster, corroborating the correlation coefficient analysis. Examples of the relationships between H_s and IOD/ENSO are described as follows. It is worth mentioning that the opposite convention in relation to Saji *et al.* (1999) has been used here for positive and negative phases of the ENSO, since they use Niño 3 SST anomalies (El Niño [+]; La Niña [-]) and we use the SOI (El Niño [-]; La Niña [+]). Concomitant positive IOD and negative ENSO extreme events occurred in 1972 (Saji *et al.*, 1999) and 1997 (Saji *et al.*, 1999; Cai *et al.*, 2014). In the first, the IOD was associated with H_s in the western and eastern clusters through ~ 3 -year cycles, and in the southern cluster through ~ 2 -year cycles (Figure 2.6a). The SOI and H_s were correlated in the western cluster through signals with periodicities of ~ 3 years (Figure 2.6b). In the second concomitant extreme event (1997), H_s showed correlations with the DMI in the western and southern clusters at periodicities of approximately 4 years (Figure 2.6a), while 3 to 4-year cycles related to the ENSO were highlighted in the same clusters (Figure 2.6b). The moderate IOD event of 1982 (Cai *et al.* 2014) in combination with the extreme ENSO event in the same year (Cai *et al.*, 2015) also resulted in large waves. Correlations with the DMI and SOI were observed in the western cluster (~ 4 -year cycles). Additionally, H_s and SOI were also correlated in the southern cluster (~ 2 -year cycles). The extreme positive IOD event that occurred in 1994 (Cai *et al.*, 2014; Saji *et al.*, 1999) presented strong correlations with H_s in the western cluster and moderate correlations in the southern cluster, both at periodicities of approximately 4 years (Figure 2.6a). Moderate correlations of H_s with the SOI were also noted in 1994, with cycles of approximately 4 years in the western and southern clusters and at the seasonal timescale in the southern cluster (Figure 2.6b). These might have been triggered by the IOD due to its relationship

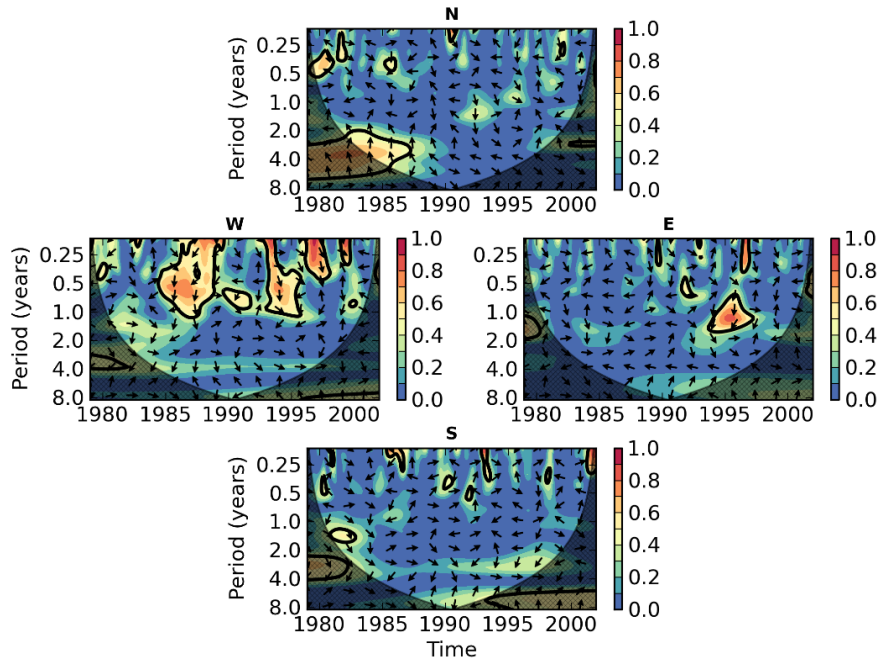
with the ENSO. Another extreme IOD event took place in 1961, as reported by Saji *et al.* (1999). This had an effect on H_s only in the southern cluster, at periodicities of approximately 3 years (Figure 2.6a). As discussed in the correlation coefficient subsection, positive anomalies in H_s are generally seen during negative/positive phases of the IOD/ENSO in the northern cluster. Knowing that El Niño conditions prevailed during the extreme ENSO event of 1982, one observes decreases in H_s in the northern cluster in this year, indicated by upward arrows in all timescales with significant correlations (Figure 2.6b). Extreme La Niña events occurred in 1988–1989 and 1998–1999 (Cai *et al.*, 2015). Their signatures can be clearly seen in the northern cluster at ~5 and ~2-year cycles, respectively (Figure 2.6b). In contrast, downward arrows suggest decreases in H_s in the southern cluster in 1998–1999. The IOD negative phase was rather weak and short during 1988–1989, and stronger and longer during 1998–1999. However, signals with cycles of approximately four and two years, respectively, were still apparent in the northern cluster during both periods, suggesting influence of the ENSO on the IOD.

Remarkable long-term (longer than 8 years) cycles are noted in the wavelet coherence spectra of H_s with the SAMI in all clusters (Figure 2.7a). Although these features are under the influence of edge effects, which means that they should be treated with caution, Gong and Wang (1999) reinforce the importance of examining the decadal variability of the SAM. Correlations of H_s with the SAMI at decadal timescales were strengthened from the late 1980s onward, with upward arrows indicating larger waves associated with positive phases of the SAM. Regarding shorter timescales, the strongest correlations of H_s with the SAMI were found in the western cluster, with cycles generally shorter than approximately 4 years. Strong correlations at the biannual timescale occurred in the southern cluster around the mid-1960s, indicating that positive SAM was accompanied by positive anomalies in H_s . These correlations mark the onset of the trend toward the positive phase of the SAM, which has been occurring since the mid-1960s (Marshall, 2003). The SAMI and H_s also presented strong correlations in the western cluster at seasonal timescale in the late 1950s and late 1960s. In the same cluster, a ~2-year cycle was dominant from the early 1980s until the mid-1990s, when larger waves

were associated with negative phases of the SAM. With respect to the ZW3, very distinct patterns were observed among the clusters (Figure 2.7b). According to Raphael (2004), significant fluctuations of the ZW3 resulted in rapid changes from the atmospheric meridional flow to zonal flow in 1986–1987 and 1993–1995. These fluctuations coincided with strong correlations of the ZW3 index with H_s in the western cluster at intra-seasonal, seasonal, and biannual timescales. Another strong signal at intra-seasonal and seasonal timescales took place in 1996–1997, suggesting that larger waves occurred in the western cluster during the migration of the atmospheric zonal flow to meridional flow (Raphael, 2004). In the same cluster, signals of the annual cycle described by Raphael (2004) appeared in the mid-1990s and early 2000s. The main cycle in the eastern cluster also appeared around the mid-1990s at the annual timescale. The northern cluster presented correlations at inter-annual timescales (2–8 years), with most signals under the influence of edge effects. A similar pattern is observed in the southern cluster for cycles ranging from 2 to 4 years.



(a)



(b)

Figure 2.7. Squared wavelet coherence spectra of significant wave height with the: (a) SAMI and (b) ZW3 index. The 90% confidence levels are represented by thick contours, and hatched areas represent the cone-of-influence. In phase and anti-phase signals are represented by arrows pointing upward and downward, respectively. Arrows pointing rightward represent climate patterns preceding H_s , whereas the converse is true for arrows pointing leftward. The letters N, W, E, and S, on top of each plot, stand for northern, western, eastern, and southern clusters, respectively.

The PDO index and H_s were moderately correlated in all clusters (Figure 2.8). Despite being under the influence of edge effects, inter-annual PDO cycles (5–8 years) were significantly correlated with H_s until the mid-1960s and after the mid-1990s. PDO cycles ranging from the intra-seasonal up to the biennial timescale were also associated with changes in H_s throughout the period of analysis, especially in the western and eastern clusters.

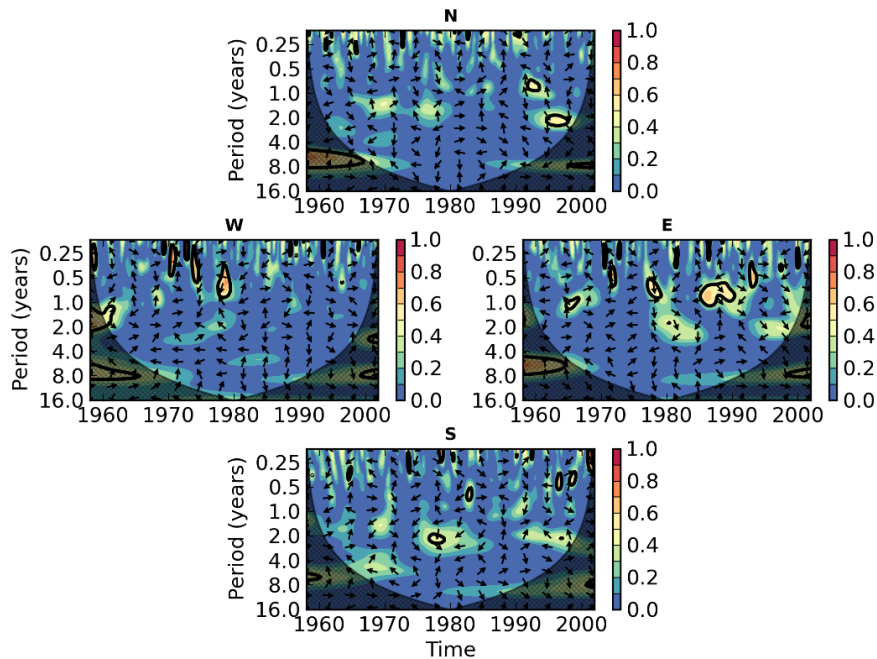


Figure 2.8. Squared wavelet coherence spectra of significant wave height with the PDO index. The 90% confidence levels are represented by thick contours, and hatched areas represent the cone-of-influence. In phase and anti-phase signals are represented by arrows pointing upward and downward, respectively. Arrows pointing rightward represent climate patterns preceding H_s , whereas the converse is true for arrows pointing leftward. The letters N, W, E, and S, on top of each plot, stand for northern, western, eastern, and southern clusters, respectively.

The squared wavelet coherence spectra of the climate indices with the other wave parameters (not shown) presented analogous structure to the squared wavelet coherence spectra of H_s with the climate indices. Obviously, some cycles were either stronger or weaker than the ones just mentioned, and were either longer or shorter. Some of the strong statistically non-significant signals seen in

the coherence spectra of the climate indices with H_s , showed statistically significance in the squared wavelet coherence spectra of climate indices with the other wave parameters. In addition to that, some features noted only in certain clusters occasionally became apparent in others. Therefore, only noteworthy differences are mentioned below.

The greatest differences relative to H_s were generally found in the coherence spectra of D_p with the climate indices. Significant correlations of the DMI with D_p in the western cluster were mostly associated with short-lived IOD signals. Substantially strong correlations between the IOD and $90thH_s$ in the eastern cluster during the 1970s indicate that larger extreme waves occurred in association with ~ 3 -year cycles of positive IOD. In the western cluster, longer T_{mean} correlated with positive IOD at inter-annual timescales (1.5–3 years) from the early 1960s to the mid-1970s. Regarding the ENSO, strong correlations with D_p were found in the eastern cluster at seasonal, intra-annual, and annual timescales during the extreme 1972 El Niño. These suggest that wave direction rotated counter-clockwise. Additionally, an 8–14-year energy band in the western cluster spanning the whole hindcast period indicated counter-clockwise/clockwise rotation in D_p during El Niño/La Niña events. This band was replicated in the southern cluster for $90thH_s$, contributing to decreases in extreme waves during El Niño years. Longer T_{mean} was correlated with inter-annual El Niño cycles (1.5– ~ 3 years) in the eastern cluster from the late 1950s to the mid-1960s and from the early 1980s to the early 2000s. Counter-clockwise rotation in D_p in the northern cluster was associated with positive SAM (signals at inter-annual timescales up to ~ 8 years). Wave periods (T_{mean} and T_p) were strongly correlated with the SAMI in all clusters during the whole hindcast period. Among all wave parameters, they were the most correlated with the SAMI at timescales ranging from intra-seasonal to inter-decadal. In general, longer wave periods were associated with positive SAM, excepting in the northern cluster. Clockwise rotation in D_p was strongly correlated with positive PDO in the western cluster from the late 1950s to the late 1980s (at mainly inter-annual timescales). Finally, longer wave periods (T_{mean} and T_p) were associated

with positive PDO in the western and southern clusters during the 1970s (~2–6-year cycles).

The anomalies of wave parameters are enhanced or reduced when climate modes coincide in time and frequency. The climate modes have overlapped in several periods of time, as can be noted in Figure 2.9, which shows normalised anomalies (top) of the climate indices with their corresponding power spectra (bottom). The anomalies provide information on the climate mode phases and how strong they were. On the other hand, they do not explain the exact percentage of variance related to each cycle. As this issue is beyond the scope of this chapter, the variance related to each cycle is not analysed. Thus, for the purpose of understanding inter-relationships among the climate patterns, correlation coefficients (R) were computed for the monthly anomaly time series of their indices during the hindcast period (Table 2.1). The largest correlation occurs between the SOI and PDO index ($R=-0.35$), which strongly co-varied in the early 1970s and in the 1990s (Figure 2.9c and 2.9e). The negative nature of this correlation is in agreement with Mantua *et al.* (1997). A correlation of $R=-0.29$ between the SOI and DMI reinforces the studies of Schott *et al.* (2009) and Izumo *et al.* (2010), and is associated with cycles that co-varied at inter-annual timescales, between approximately 1.5 and 6 years (Figure 2.9c and 2.9d). Yuan and Li (2008) stated that the ZW3 is rather independent from the SAM. However, a statistically significant correlation of $R=0.21$ was found despite the little variability shared by the modes (Figure 2.9a and 2.9b). The SAMI and DMI presented a low but statistically significant correlation of $R=0.09$, which is related to cycles that co-varied at timescales between 0.5 and 4 years (Figure 2.9a and 2.9d). Raphael (2004) suggested a possible relationship between the ZW3 and ENSO, but a statistically non-significant correlation of only $R=0.06$ was obtained here. Correlations between the SOI and SAMI are positive but without statistical significance, as previously reported by Harley *et al.* (2010). However, Stammerjohn *et al.* (2008) showed that when positive/negative phases of both the ENSO and SAM occurred simultaneously, the high-latitude ice-atmosphere response to the ENSO was stronger than when they were not concurrent.

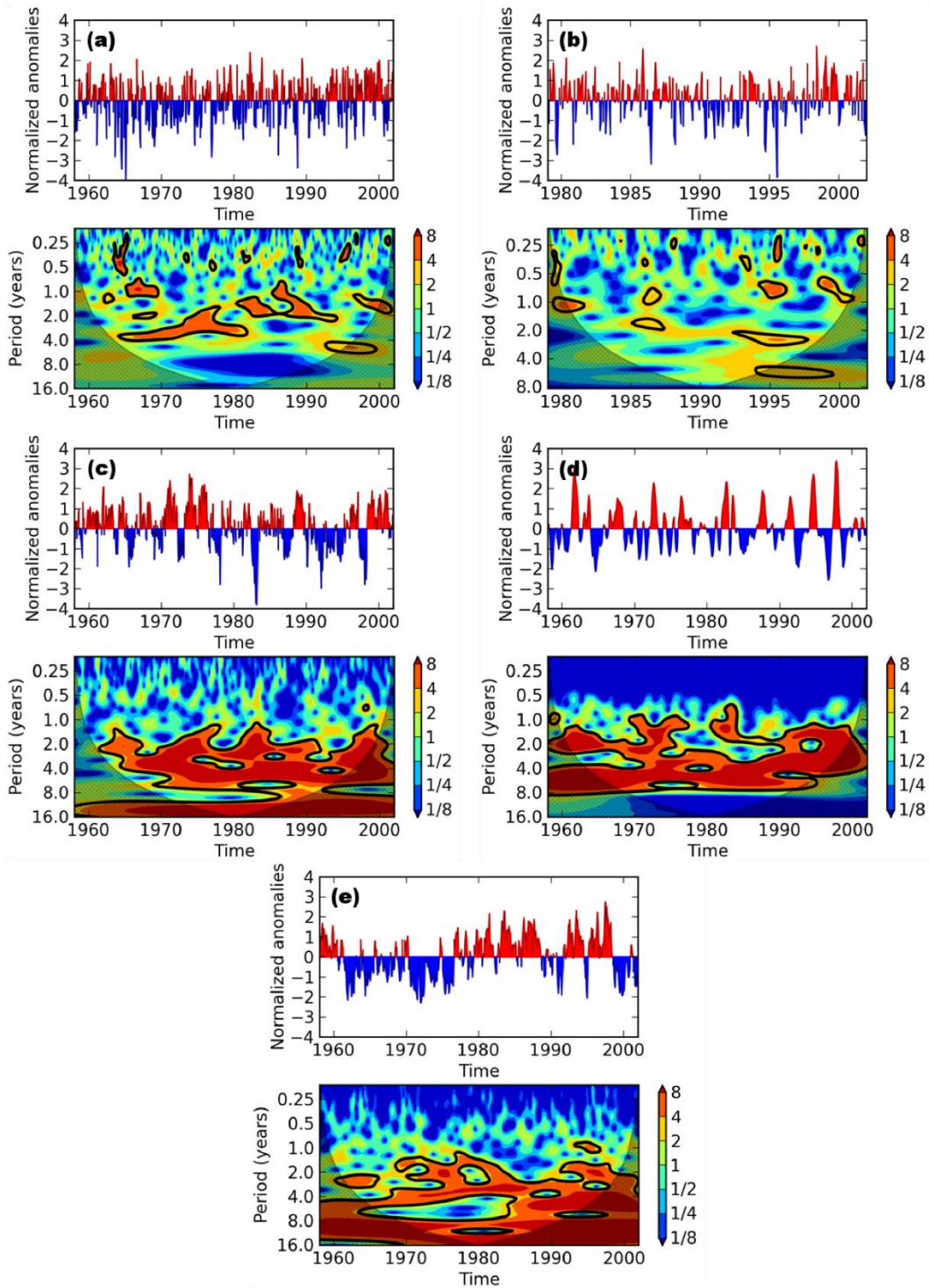


Figure 2.9. (top) Normalised anomalies of the climate indices with their corresponding (bottom) power spectra: (a) SAMI, (b) ZW3 index, (c) SOI, (d) DMI, and (e) PDO index. The 95% confidence levels are represented by thick contours, and hatched areas represent the cone-of-influence.

Table 2.1. Correlation coefficients among the climate indices for the period 1958–2001^a.

	SAMI	SOI	DMI	PDO index
SOI	0.05			
DMI	0.09	-0.29		
PDO index	-0.01	-0.35	-0.04	
ZW3 index	0.21	0.06	-0.04	-0.08

^aCorrelations with the ZW3 index comprise the period 1979–2001. Statistically significance within 95% is represented by bold font.

2.7 Conclusions

The influence of climate patterns on the wave climate around New Zealand and the surrounding southwest Pacific Ocean has been explored in detail in this chapter. The results of a 45-year (1957–2002) wave hindcast were compared to atmospheric oscillations over several timescales. First, the mean annual and inter-annual variabilities of H_s were computed with the purpose of verifying sites susceptible to large variations in relation to average wave conditions. Then, the PDO, ENSO, IOD, SAM, and ZW3 modes were correlated with five simulated wave parameters. The interactions of D_p , T_p , T_{mean} , H_s , and $90thH_s$ with the climate modes were assessed by correlation coefficients and squared wavelet coherence spectra.

In general, low to moderate correlations between climate patterns and wave parameters were obtained. This suggests that many factors contribute to the variability of the wave climate in the region of study. Positive correlations of the wave parameters with the SAMI in the highest latitudes of the regional domain arise from the strengthening of westerly winds generated by stronger pressure gradients between 40°S and 65°S during its positive phase. The SAM is the most important climate pattern for wave direction, which rotates clockwise south of the country and counter-clockwise along and off the west and north coasts during positive SAM. The zonal wind stress anomaly induces larger waves along and off the west and south coasts of New Zealand during negative phases of the ZW3. The ENSO also plays a significant role, with northeasterly winds producing larger waves

to the north of New Zealand during La Niña phases, while southwesterly winds cause larger waves around the rest of the country during El Niño events. Positive phases of the PDO contribute to increasing wave height and wave period mainly along and off the west and south coasts. The influence of the IOD on the wave climate is also more significant during its positive phase, when wave periods and wave heights increase around most parts of the country (except to the north). Correlations of H_s with the SOI using seasonally averages were also conducted (not shown) and presented substantially higher statistically significant values than monthly averages. An example that reinforces such stronger correlations is the warming in the tropical Indian Ocean due to the ENSO, which takes approximately 3 to 6 months to occur (Deser *et al.*, 2010). According to Harley *et al.* (2010), seasonally averaged SOI values are more suitable for correlations with other parameters than monthly averaged values, since the latter produce a non-coherent pattern due to the inherent noisiness of its time series at short timescales. This issue is beyond the scope of the present chapter, but deserves further investigation in future studies.

The correlation coefficient analysis provided a good overview, in terms of spatial distribution, of the relationships between the wave parameters and different phases of the climate modes. However, information on how these relationships have evolved in time cannot be extracted from such analysis. Thus, this was accomplished by using wavelet coherence spectra. First, a cluster analysis was conducted to divide the regional domain into distinct wave climates. This enabled the assessment of the dominant modes of variability related to each climate pattern through wavelet coherence spectra. The latter revealed that the wave parameters exhibited remarkable cycles throughout the hindcast period. Strong correlations at inter-annual timescales were identified during ENSO and IOD extreme events. The SAM decadal variability showed a substantial relationship with the wave parameters, especially from the late 1980s to the early 2000s. A number of authors (e.g., Young *et al.*, 2011, 2012; Wentz *et al.*, 2007) have found increasing trends in wave height and wind speed. Whether these trends are related to either long-term trends or atmospheric oscillations varying at decadal timescales is an issue that

remains open. Our results support the relationship between increases in wave height and the intensification of the SAM in recent decades. Nevertheless, decadal timescales are in a region of the spectrum that does not allow us to make conclusive inferences. A longer-duration dataset is needed to further investigate this question. The SAM also affected the wave parameters at seasonal, annual, and inter-annual timescales. The western cluster was the most impacted by all climate patterns tested. During significant fluctuations of the ZW3, when the atmospheric flow rapidly changed from meridional to zonal and vice versa, strong correlations with the wave parameters were highlighted at seasonal and intra-seasonal timescales. The PDO presented the weakest correlation with the wave parameters, influencing more the peak wave direction with clockwise rotation during its positive phase.

The MAV and IAV results revealed high variability in coastal areas, especially in sheltered regions where little or no significant trend in H_s was identified. In general, an increasing trend in H_s was observed around the country, with values varying between 1 and 6 cm/decade near the shoreline. Correlation coefficients confirmed that coastal areas are generally more affected by the climate modes than offshore regions, and consequently are more vulnerable to climate changes. These results suggest, for instance, that habitats such as the mangrove forests, which extend down to approximately 38°S in New Zealand, might experience greater stress during certain phases of atmospheric oscillations, since successful seedling establishment is sensitive to wave energy (Balke *et al.*, 2013). However, as shown by Lovelock *et al.* (2010), atmospheric oscillations can also favour mangrove forests expansion. Changes in the wave climate might impact on the physiological structure and survivorship of marine organisms. Kelps, for example, differ in morphology according to their wave exposure (Nanba *et al.*, 2011), and relationships between storm waves during ENSO events and mortality of kelp forests have been documented by Dayton *et al.* (1992). In New Zealand, Schiel and Thompson (2012) suggested that the growth rate of kelp is associated with wave height and wave direction.

In terms of coastal engineering, beach erosion, which increasingly has been shown to vary around the Pacific (Barnard *et al.*, 2015) and in New Zealand with wave climate variations (e.g., de Lange, 2001), represents a major problem for the expanding coastal population of the country. Our results also provide further support to the existence of climate-cycle driven temporal patterns in sand spit erosion and accretion, which have occurred in opposing phases between the east and west coasts of the upper north island of New Zealand (Bryan *et al.*, 2008). The opposing cycles of erosion and accretion between the Ohiwa spit and Mokau spit in Bryan *et al.* (2008), which are located in the northern and western clusters (locations given in Figure 2.1), respectively, were hypothesised to be caused by the shift to positive PDO in the early 1980s. Our results suggest that opposing changes to wave heights in the western and northern clusters could more likely be driven by changes to the IOD and ENSO, since both showed a strengthening of the signal in these sectors during this time period (Figures 2.6a and 2.6b). The SOI also becomes more negative during this time (Figure 2.9c), which is correlated with an increase in wave height on the west coast and decrease on the northeast coast. The increase in the correlation of H_s with the DMI in the west coast (Figure 2.6a), which occurred at the 4-year cycle at the beginning of the 1980s, might also have contributed to the observed increased erosion. Erosion processes are known to be nonlinear, with recovery timescale much longer than the accretion timescale (Yates *et al.*, 2009), and so a period of severe erosion may not be balanced by a period of severe accretion in the same way as a period of minor erosion is compensated by a period of mild accretion. Therefore, a more variable wave condition could explain the increase in beach erosion. The PDO is not a strong driver of wave height on the northeast coast, but the correlation is generally opposite between the northern and western clusters. Spits also accrete by alongshore transport (driven by wave angle changes) in addition to cross-shore transport (driven by wave height changes), and so the northeast coast accretion during the 1980s could be associated with the shift to wave directions more toward the north that occur during the positive phases of the PDO in the northern cluster (Figure 2.4).

This chapter showed the importance of considering multiple climate modes to understand the drivers of changes in wave parameters broadly, since the modes superimpose and occasionally trigger each other. We recommend that more work be undertaken on interactions between two or more atmospheric oscillation modes in periods of time that modes share strong anomalies. Nevertheless, these results clearly show the variability of the wave climate around the diverse coastline of New Zealand. They can provide a proxy with which to improve our ability to predict the impacts of future climate change on the wave climate.

Contributions of the author and co-authors to Chapter 3

I was responsible for the data processing, data analysis, and writing. I came up with the idea of the topic addressed in this chapter and defined the methodology employed.

Richard M. Gorman produced and validated the hindcast results employed in Chapter 3.

Scott A. Stephens provided me with some code for estimating significant wave height return values, which I adapted to suit my needs. He also suggested carrying out the extreme value analysis for the model grid points on the 50 m isobath around New Zealand.

Scott A. Stephens, Karin R. Bryan, and Richard M. Gorman reviewed Chapter 3 and made suggestions regarding the writing.

CHAPTER 3: The extreme wave climate around New Zealand

3.1 Introduction

Extreme wave events have been recognised as a major issue for safety in both coastal and offshore regions. With the ongoing concerns about changes in the frequency and magnitude of cyclones across the globe (Simmonds and Keay, 2000), and the high vulnerability of coastal areas to wave attack as the sea level rises (Hannah, 2004; Hannah and Bell, 2012; Hauer *et al.*, 2016), there is a need to understand and predict the behaviour of extreme wave events.

Climatologies have generally been established for the mean state of the ocean, whereas the equivalent for extreme events is not as common despite the valuable information that these can provide for the management of coastal erosion and flooding (Horrillo-Caraballo *et al.*, 2012), for example. One impediment to examining extreme values is that the different statistical characteristics of extreme and non-extreme wave events (Young *et al.*, 2012) require them to be analysed separately.

One of the most common ways to assess extreme wave events is to calculate return-period values for significant wave height (H_s) (e.g., Alves and Young 2003; Guedes Soares and Scotto, 2004). The 100-year return value of H_s , for example, is the H_s value exceeded, on average, once in 100 years (Carter and Draper, 1988). Such values are required for engineering design because extreme waves can have major impacts on safety, operability of shipping and structures, and the economics of offshore facilities (Young *et al.*, 2012). Several studies have estimated return values of H_s on a global spatial scale using modelled results (e.g., Caires and Sterl, 2005), satellite altimetry data (e.g., Izaguirre *et al.*, 2011; Vinoth and Young, 2011; Young *et al.*, 2012) and buoy measurements (e.g., Hemer, 2010). However, global models and satellite measurements do not generally provide sufficiently high-resolution data for predicting return values precisely near coastal areas. Although many local studies have been conducted for specific areas (e.g.,

the Portuguese coast (Ferreira and Guedes Soares, 1998), the Persian Gulf (Moeini *et al.*, 2010), the Australian region (Hemer *et al.*, 2017), and the Kuwaiti waters (Neelamani *et al.*, 2007)), several regions in the world still lack investigation, especially in the Southern Hemisphere (e.g., New Zealand).

The international interest in the water bodies surrounding New Zealand has grown with the implementation of various trade agreements (World Bank Group, 2016), which increase traffic along key shipping routes, and with the recognised importance of the Southern Ocean in regulating the Earth's climate (Lavergne *et al.*, 2014). New Zealand is an island nation highly influenced by its surrounding oceans. The country lies at the mid-latitudes of the Southern Hemisphere and is affected by a range of atmospheric systems. Large waves, generated by extratropical cyclones, propagate without major obstacles through the Southern Ocean, and affect a large portion of the New Zealand coastline (Godoi *et al.*, 2016; Gorman *et al.*, 2003a, 2003b). Additionally, waves formed by tropical cyclones also play a significant role, especially on the north coast. A recent study (Godoi *et al.*, 2016) showed the influence of climatic patterns on the average wave climate around New Zealand in addition to an increasing trend in H_s along the coast. New Zealand's coastal population has been growing in the last decades (Bryan *et al.*, 2008), and therefore, improved predictions for coastal planning are required to deal with the threat posed by extreme wave events in this complex environment.

The paucity of wave data around New Zealand has made it difficult to accurately provide an extreme wave climatology (synthesis of extreme wave conditions based on long-term statistics) and conduct extreme wave predictions (Stephens and Gorman, 2006). Buoy measurements are generally taken as ground truth (e.g., Hemer, 2010). However, short duration records and insufficient number of buoys preclude reliable estimates of return values in many cases. Satellite altimetry data can also be problematic; among the drawbacks is the temporal coverage of measurements: the infrequent re-visit (typically 10 days) of the satellite to a particular location makes it difficult to adequately capture storm peaks. Stephens and Gorman (2006) conducted an extreme wave analysis for six sites off

the New Zealand coast by using results from a 20-year hindcast, providing evidence of the importance of modelled results when a long dataset is required.

The accuracy of extreme predictions depends on the accuracy and length of input data (Stephens and Gorman, 2006). Using results from the 45-year (September/1957–August/2002) high resolution wave hindcast (hereafter 45WH), conducted by Gorman *et al.* (2010), we have created an extreme wave climatology for the New Zealand continental shelf waters, and analysed trends and patterns in extreme events. In order to complement our study, the extreme estimates carried out by Stephens and Gorman (2006) have been extended to shallower waters. The 45WH covers a considerably longer time period than the hindcast used by Stephens and Gorman (2006) and has higher space-time resolution in shallow waters, which make the new modelled data more suitable for predicting extreme events and establishing an extreme wave climatology.

3.2 Dataset

In order to conduct the extreme wave analysis, modelled time series of H_s and mean wave period (T_{m-10} , hereafter T_{mean}) were extracted from the regional grid domain (Figure 3.1) of the 45WH. T_{mean} was chosen over the peak wave period (T_p) because the latter was sometimes undefined in the hindcast data because of missing values close to the shore. As T_{m-10} is more weighted to lower frequencies than T_{m-01} and T_{m-02} , it is more representative of swell, and so a better proxy for T_p . Only the full calendar years (1958–2001) of the 45WH have been used. The 45WH was conducted using the WAVEWATCH III v. 3.14 model (Tolman, 2009) forced with 1.125° spatial resolution wind and ice fields from the ERA-40 reanalysis project (Uppala *et al.*, 2005) on a global grid at $1.125^\circ \times 1.125^\circ$ resolution. One-way nested within the global grid, a regional grid domain, with $0.125^\circ \times 0.09375^\circ$ (approximately 10 km) resolution, encompassed part of the Tasman Sea and parts of the Southern and southwestern Pacific oceans. The regional grid provided a higher-resolution representation of nearshore wave processes, although the same ERA-40 inputs were used as for the global simulation. Mean wave parameters were output at 1 h and 3 h intervals for the regional and global domains, respectively.

These have been validated against buoy measurements, located mainly around New Zealand and North America, and satellite altimetry data, obtained from the TOPEX/Poseidon, ERS1 and ERS2 missions. A mean root-mean-square error of 0.50 m and mean correlation of 0.83 were obtained from comparisons of H_s between the regional results and New Zealand buoy data (Godoi *et al.*, 2016; Gorman *et al.*, 2010). Comparisons to altimeter data over the regional hindcast area show positive bias in H_s , of up to +0.3 m, in offshore waters of the Tasman Sea and Southern Ocean, and negative bias near the coast, of down to -0.3 m. The spatial pattern of bias is similar to the results of Chawla *et al.* (2013). Additional details of the model simulation and its validation can be found in Gorman *et al.* (2010) and Godoi *et al.* (2016).

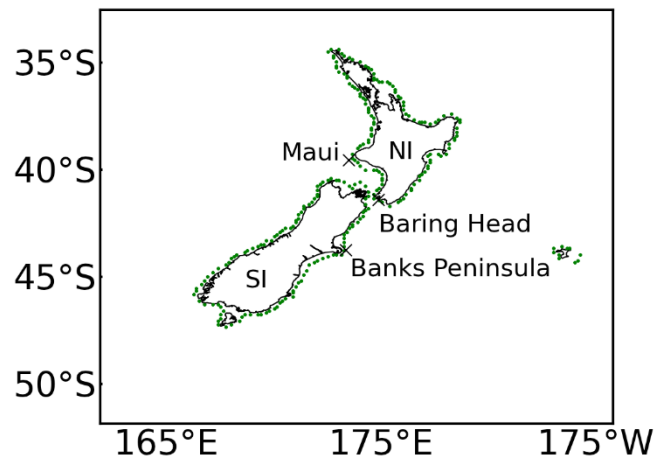


Figure 3.1. Regional grid domain of the 45-year wave hindcast. Green dots represent the model grid points on the 50 m isobath, whereas crosses indicate the buoy locations. NI and SI stand for North Island and South Island, respectively.

Large waves were generally underestimated by the model in comparison to buoy measurements (Gorman *et al.*, 2010). This is consistent with the triple-collocation study of Caires and Sterl (2003), who showed that ERA-40 tended to underpredict high wind speeds compared to ERS-1 and TOPEX measurements, while the wave model correspondingly underpredicted the upper range of significant wave heights from buoy and altimeter records. The underestimation of large waves in the 45WH may have arisen from two factors. The first is the relatively

low space-time resolution of the ERA-40 winds, which does not take abrupt changes in direction and substantial wind speed gradients into account (Godoi *et al.*, 2016); and the second is the use of the formulation proposed by Tolman and Chalikov (1996) in the hindcast, which underestimates the energy input during intense storm conditions dominated by young wind-sea (Ardhuin *et al.*, 2007). Uppala *et al.* (2005) observed that the detection of tropical cyclones in the Southern Hemisphere exceeded 90% in comparison to a best-track dataset (Neumann, 1993) for the period from 1973 onwards. However, the percentages of detection in ERA-40 for the periods 1958–66 and 1967–72 were 75% and 82%, respectively. Furthermore, ERA-40 tends to underestimate wind speeds above 14 m/s (Caires *et al.*, 2004). Regarding the second factor, Stopa *et al.* (2016) compared the performance of various sets of parameterisations for the same wind input. The ST4 parameterisation (Ardhuin *et al.*, 2010) did best across the H_s range, while ST2 (Tolman and Chalikov, 1996) had high positive bias in the lower range, decreasing for larger wave heights. This seems consistent with insufficient swell dissipation and underestimation of wind-sea, in ST2. It also shows that while ST4 is a better choice now that it is available, the deficiencies of ST2 are not as significant for extreme climate as for mean climate. In order to determine properly the individual contributions of the wind fields and the set of parameterisations used in the present work to the underestimation of extreme waves, a set of tests would be required. These include doing several model runs using the same set of parameterisations combined with wind fields from different sources (not only ERA-40), as well as testing different sets of parameterisations forced with ERA-40 wind fields (similar to what was done by Stopa *et al.* (2016)). Then, the results should be compared to observed data. Another way of validating a specific set of parameterisations is to test them against other sets that have been validated already. Conducting these tests is beyond the scope of this thesis.

Although the underestimation of large waves is acknowledged, the lack of long buoy records to account for extreme events in the study region forced the use of uncalibrated modelled data in our study. A possible solution for calibrating the model data would have been estimating an approximate bias for extreme H_s from

comparisons between model and buoy data. However, implementing this solution in shallow waters based on just a few buoy records is likely to lead to erroneous calibration, especially when land-sheltering effects prevail due to buoy proximity to the coast and headlands. As a consequence of these effects in addition to short buoy records, the bias varies considerably around the coast, and so would have caused spurious calibrations (as shown by Stephens and Gorman (2006)). Despite the recognised underprediction of extreme events by the model, its results still allowed exploration of the spatial distribution of extreme events, their trends and clustering patterns. Although a calibration procedure was not performed, model and buoy data were compared in terms of the probability of occurrence of extremes at the locations where buoy data do exist and span more than 10 years (Figure 3.1).

Buoy records from twelve sites around New Zealand were analysed regarding their suitability for extreme wave predictions (not shown), and only three of them (Table 3.1, Figure 3.1) were considered to be of sufficiently long duration. The others were short records due to either short recording periods or large gaps of missing data after spike removal, hence they will not be discussed further. Buoy data whose H_s values were out of the range 0–25 m were considered spikes. H_s time series were extracted from the buoy and model data at the coordinates shown in Table 3.1.

Table 3.1. Buoy deployments. NIWA stands for National Institute of Water and Atmospheric Research Ltd.

Site	Longitude (°)	Latitude (°)	Recording period	Source
Baring Head	174.8467	-41.4022	03 Aug 1998 – 19 Dec 2013	NIWA
Banks Peninsula	173.3348	-43.7558	06 Feb 1999 – 28 Feb 2014	NIWA
Maui	173.45	-39.55	31 Aug 1976 – 30 Apr 1987	Shell, BP, Todd University of Auckland

Besides the H_s time series extracted at the buoy sites, two additional datasets from the model data have been used to assess extreme events, the annual maxima H_s and Peaks-Over-Threshold (POT) data. The latter are defined here as maxima H_s from independent storms, with maxima H_s being considered only if above the 99th percentile (of the full hourly dataset) and separated by a minimum interval of 72 hours. The set of maxima of H_s identified by the POT approach and the annual maxima H_s are also referred to as "extreme H_s ". Due to computational costs, POT data have been produced only at 247 model grid points on the 50 m isobath around New Zealand (Figure 3.1).

3.3 Extreme wave climatology

Monthly and seasonal climatologies of extreme events over the 44-year (1958–2001) period were defined using the POT dataset on the 50 m isobath. Averages of extreme H_s and number of extreme wave events were computed for the 12 months and 4 seasons over all years (summer: Dec, Jan, Feb; autumn: Mar, Apr, May; winter: Jun, Jul, Aug; spring: Sep, Oct, Nov). The mean annual and inter-annual variabilities (MAV and IAV, respectively) of extreme H_s were also calculated. The MAV of extreme H_s was computed by normalizing the average of the annual standard deviation of extreme H_s by the annual average of extreme H_s , while the

IAV was determined by the standard deviation of the annual means of extreme H_s normalised by the overall mean of extreme H_s (Godoi *et al.*, 2016; Stopa *et al.*, 2013). Lastly, monotonic trends in the values of extreme H_s and in the number of extreme events were evaluated using the Mann-Kendall test (Mann, 1945; Kendall, 1955). The magnitude of the trends was computed by employing the Theil-Sen estimator (Theil, 1950; Sen, 1968). Annual average extreme H_s (using POT data) and annual maxima H_s were used to calculate trends in the magnitude of extreme H_s , whilst trends in the number of events were computed using time series of the annual number of extreme H_s peaks (calculated using the POT data).

Figure 3.2 shows the 44-year (1958–2001) mean annual maxima H_s and its corresponding T_{mean} (44-year mean annual T_{mean} associated with annual maxima H_s), providing an overview of different extreme wave climates around New Zealand. The spatial pattern of mean annual maxima H_s (Figure 3.2a) closely resembles the mean wave climate (Godoi *et al.*, 2016; Laing, 2000; Pickrill and Mitchell, 1979), in which the roughest seas occur in southern New Zealand, associated with largest T_{mean} (Figure 3.2b), and calmer conditions occur in regions sheltered from southwesterly swells. Such swells are obstructed by the landmass, creating a distinctive shadow zone and relatively smaller T_{mean} to the north of the country (Figure 3.2b). The largest waves on the north coast are generally associated with tropical cyclones (Gorman *et al.*, 2003a), and are considerably less frequent than the steady swells, generated by extratropical cyclones, that hit most other parts of the New Zealand coastline.

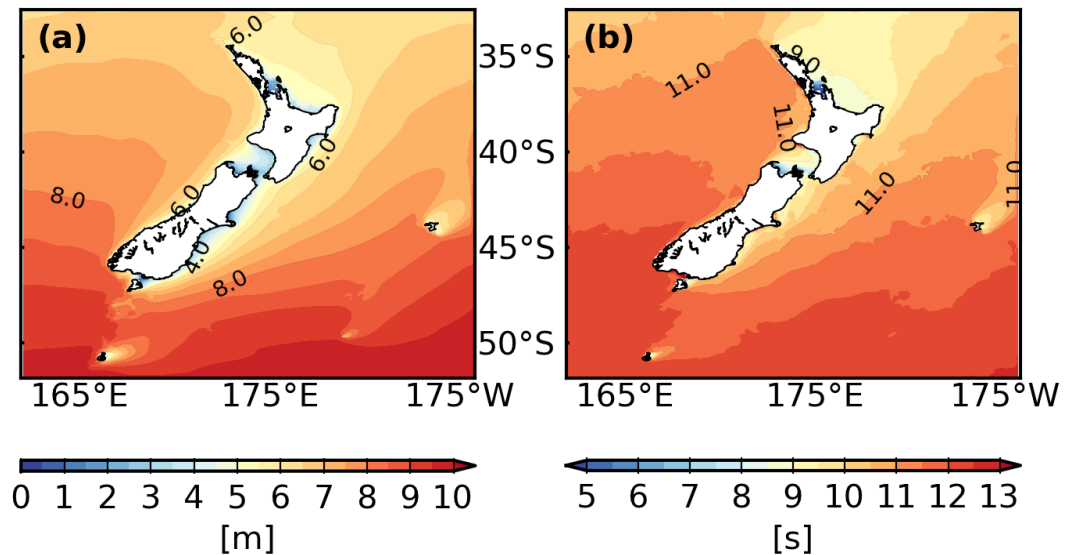


Figure 3.2. Forty-four year (1958–2001) mean (a) annual maxima significant wave height; (b) mean wave period associated with annual maxima significant wave height.

A cluster analysis was performed to thoroughly characterise extreme wave climates around the country (Figure 3.3) by using the 44-year mean annual maxima H_s ($44H_s$) and its corresponding T_{mean} ($44T_{mean}$) (standardised to a Gaussian distribution – zero mean and unit variance) and the k -means algorithm (Hartigan and Wong, 1979; Kanungo *et al.*, 2002). The cluster analysis jointly examines the input parameters and distinguishes clusters by grouping data with similar characteristics. Each colour of Figure 3.3 represents one cluster, and all grid points it comprises are considered to have similar wave climate. The red cluster (spatial averages of $44H_s$ and $44T_{mean}$ equal to 8.94 m and 12.09 s, respectively – Figure 3.3a) represents areas dominated by large swells originated in the Southern Ocean. A shadow zone appears as soon as the propagation of these swells begins to be interrupted by the New Zealand landmass (grey cluster – spatial averages of $44H_s$ and $44T_{mean}$ equal to 7.18 m and 11.11 s, respectively – Figure 3.3a). Further sheltering, associated with a lower-energy wave climate (orange cluster – spatial averages of $44H_s$ and $44T_{mean}$ equal to 5.97 m and 9.87 s, respectively – Figure 3.3a), is observed in the regions affected by a more pronounced refraction of southwesterly swells (on the east and west coasts), or where they are blocked by the landmass (to the north of the northern coast). The most sheltered zone,

dominated by low (or infrequent large) swells and local wind-sea waves, is represented by the blue cluster (spatial averages of $44H_s$ and $44T_{mean}$ equal to 2.69 m and 8.18 s, respectively – Figure 3.3a). The five clusters in Figure 3.3b provide similar information, but also show an additional low-energy wind-sea-wave-dominated environment in sheltered embayed areas (yellow cluster - spatial averages of $44H_s$ and $44T_{mean}$ equal to 1.88 m and 6.94 s, respectively). The patterns described can also be observed in Figure 3.2a. Taking into account both the cluster analysis results (Figure 3.3) and the long-term means (Figure 3.2), as well as the wave climate classification by Pickrill and Mitchell (1979) and Godoi *et al.* (2016), we divide the regions immediately adjacent to the coastline into four main extreme wave climates. These are basically demarcated by the coastline orientation, and can be roughly related to the four cardinal directions (north, east, south, and west). Thus, the analyses have been conducted focusing on these four main wave climates.

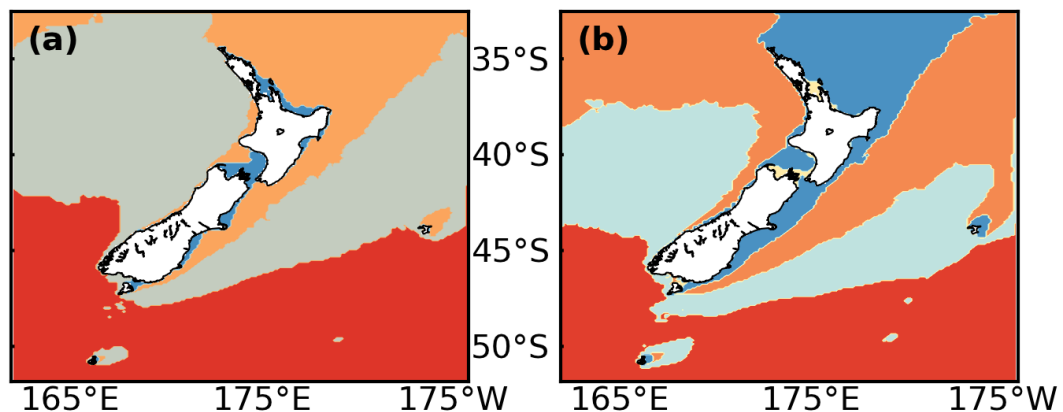


Figure 3.3. Cluster analysis results using 44-year (1958–2001) averages of annual maxima H_s and corresponding mean wave periods (a) 4 clusters; (b) 5 clusters. Each colour represents one cluster.

The annual average of extreme wave events was calculated at the model grid points on the 50 m isobath using POT data (Figure 3.4). Its values varied in the range of 2.8–6.4 events per year in the period 1958–2001, with the highest values found in the region between the two main islands of New Zealand. A large number of events also took place on the northeastern part of the country and on the central

western coast of the South Island, meaning that extreme events were more closely-spaced in these regions. The frequency of extreme events is highly dependent on the time of the year (shown next) and coastline exposure to generating regions.

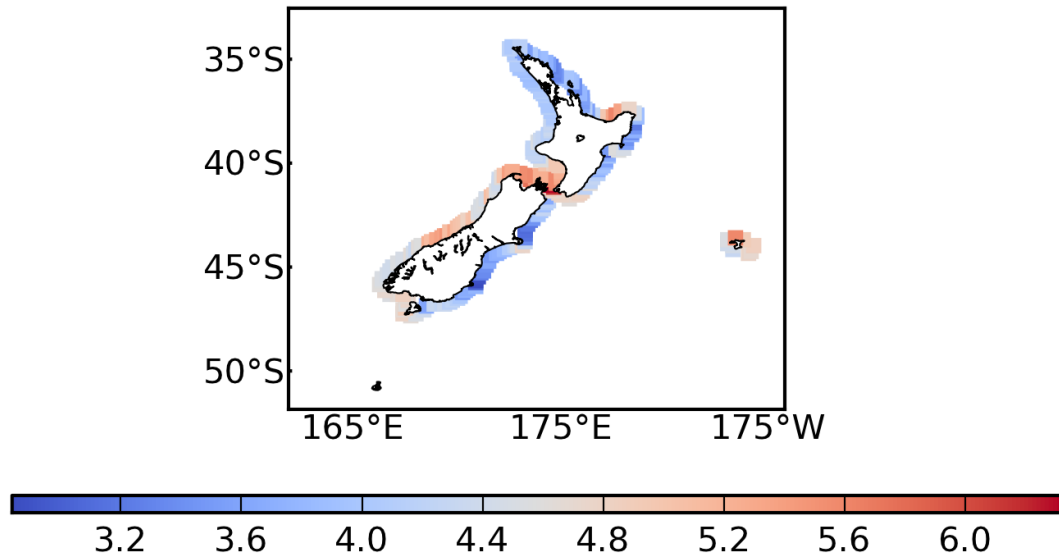


Figure 3.4. Annual average number of extreme wave events at the model grid points on the 50 m isobath (calculated using POT data).

Monthly climatologies of extreme wave events (magnitude of H_s and number of events) calculated using the POT data can be found in Figure 3.5 and Figure 3.6. The southwestern and southern coasts received the most energetic waves followed by the northwestern coast. This can be associated with extratropical cyclones generated by the westerly air flow in mid-latitudes, which produce large wave events in all months. The southernmost region of the North Island also showed intense extreme wave activity throughout all months, which can be associated with southerly swells. The mildest extreme waves were generally found in the sheltered strait between the North and South islands, where southwesterly swells are blocked by the landmass. There was little variation throughout the seasons in the spatial pattern of extreme H_s (not shown). Despite that, 47% of the examined sites received the largest waves in winter, 33% in autumn, 11% in summer, and 9% in spring. There was a remarkable contrast in the frequency of extreme wave events between the summer and winter months (Figure 3.6). Essentially the

whole country was affected by a great number of closely-spaced extreme H_s in winter time, whereas the opposite was true for summer. In fact, the highest frequency of events on the west and south coasts occurred in May (an autumn month), while on the east and north coasts it prevailed in June and July, respectively. The frequency was also high in most parts of the coastline in August. On the other hand, extreme events were least frequent in January and February. Although the wave intensity did not change considerably throughout the year, extreme events were more commonly observed from May to August. This means that there is a higher chance of erosion due to sequences of storms during those months, as well as a higher chance of extreme events coincide with a high tide, leading to multi-hazard effects.

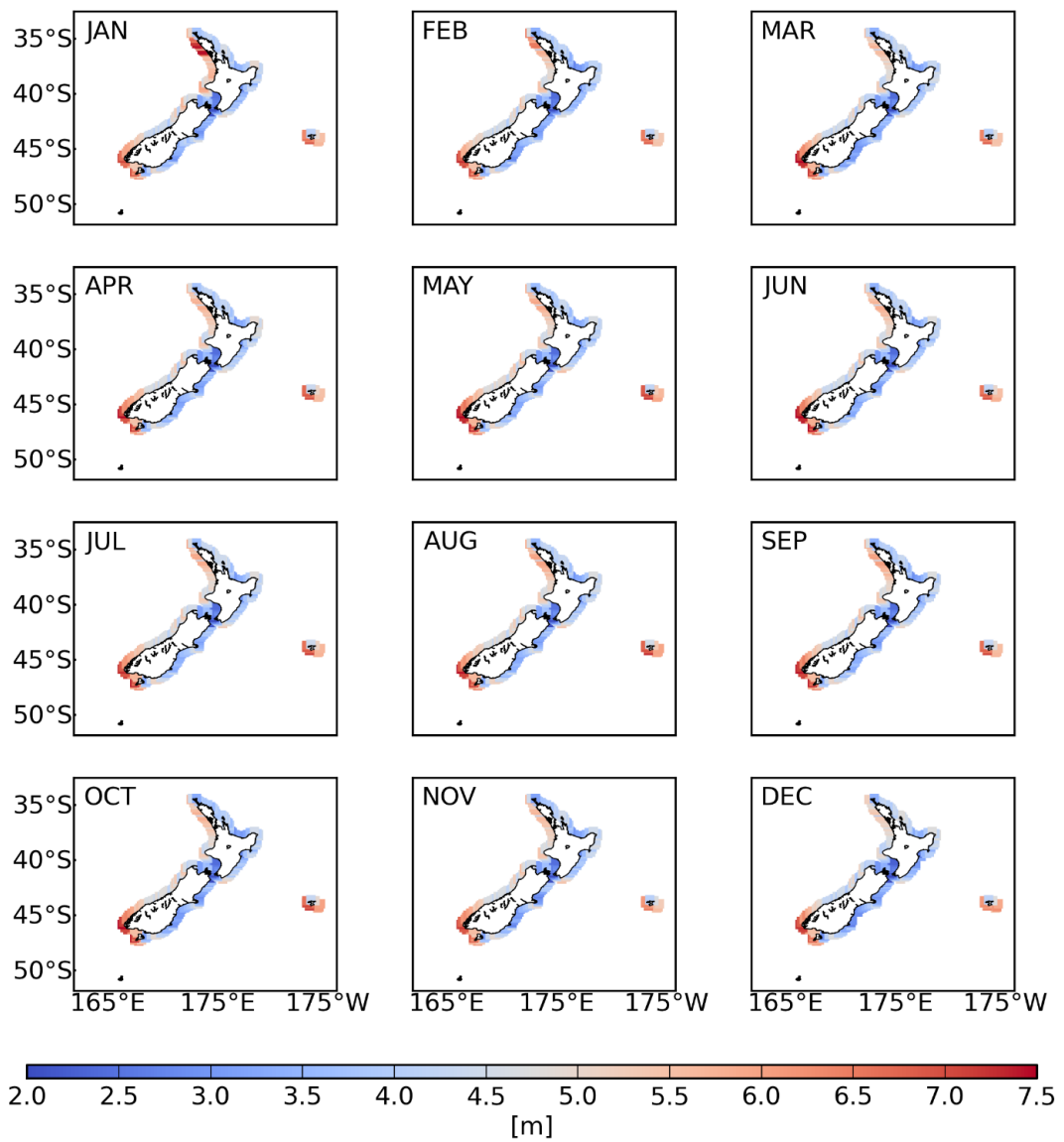


Figure 3.5. Monthly climatology of extreme H_s calculated using POT data on the 50 m isobath.

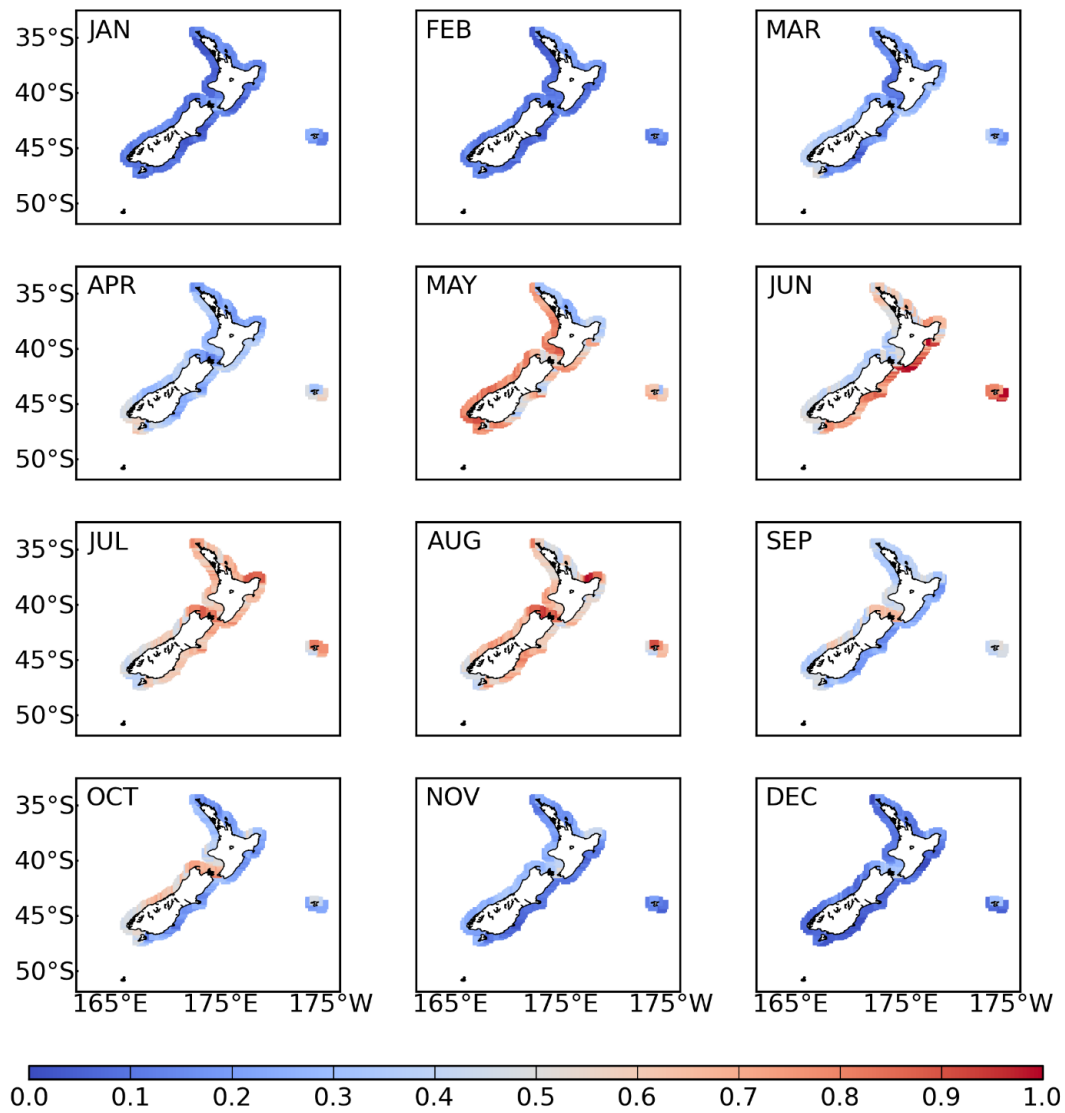


Figure 3.6. Monthly climatology of the number of extreme wave events calculated using POT data on the 50 m isobath.

Like the MAV of mean H_s (Godoi *et al.*, 2016), the MAV of extreme H_s was greatest in regions sheltered from southerly swells, emphasising the role played by locally-generated storms (Figure 3.7a). Extreme waves generated by tropical cyclones propagating to the north of New Zealand hit the north coast, especially in summer (Gorman *et al.*, 2003a), contributing to the large variability in the region. The largest IAV (Figure 3.7b) was found in the central north coast, denoting a relationship with La Niña-like effects (stronger northeasterly winds to the north of New Zealand). The east coast of the South Island had also relatively large IAV, which might be related to the Southern Annular Mode (SAM). Positive phases of the SAM

result in strengthened westerly winds in the Southern Ocean (Kushner *et al.*, 2001; Marshall, 2003), and a trend toward its positive phase has been detected since the mid-1960s (Marshall, 2003).

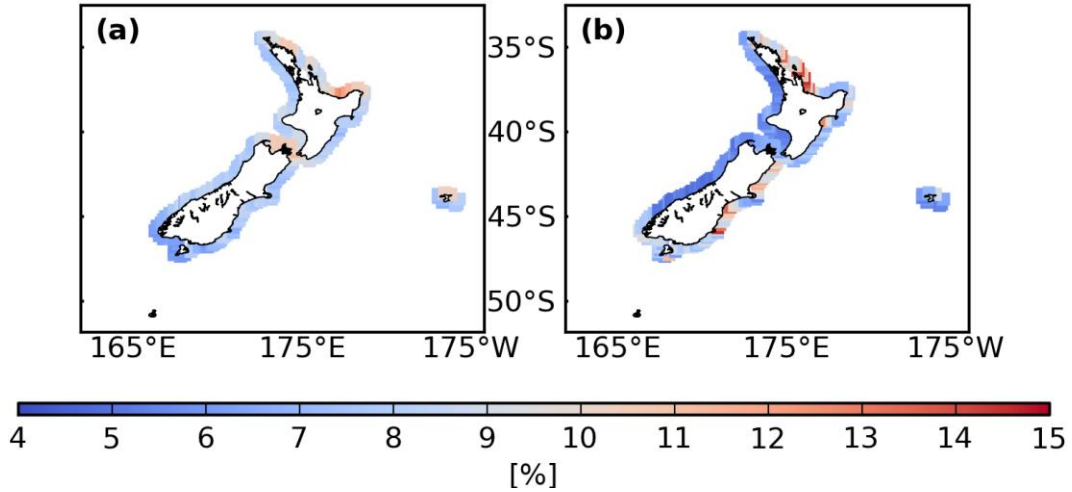


Figure 3.7. (a) Mean annual variability of extreme H_s ; (b) Inter-annual variability of extreme H_s . Both statistics were calculated using POT data on the 50 m isobath.

Trends in extreme H_s calculated from both annual maxima H_s (Figure 3.8a) and the annual average extreme H_s (computed using the POT data) (Figure 3.8b) showed some similarities regarding the spatial distribution along the coast. Notwithstanding, the ranges of magnitude of their trends presented notable distinction, varying from -2.09 to 3.43 cm/yr in the first (Figure 3.8a) and from -0.96 to 0.91 cm/yr in the second (Figure 3.8b). Only statistically significant trends at the 95% confidence level are displayed. There was no statistically significant trend in extreme H_s at most locations around the New Zealand coast. Increasing extreme H_s occurred on the northeastern part of the South Island, while a negative trend was observed in part of the west coast of the South Island in both datasets. Notable increasing trends in annual maxima H_s were also detected on the southeastern coast (Figure 3.8a). Such trends and the increasing extreme H_s observed on the northeastern coast of the South Island are consistent with the positive trend in the SAM, which has led to the strengthening of the westerly winds in the Southern Ocean (Gillett and Thompson, 2003; Hemer, 2010; Marshall, 2003; Schott *et al.*,

2009). Stronger westerly winds generate more intense extratropical cyclones, which also justify the positive trends in the number of extreme events on the south and east coasts (Figure 3.8c). These trends indicate that extreme events became more frequent over the 44 years (1958–2001) analysed. Quantitatively, 33.60% of the POT data showed positive trends in the annual number of extreme events, 65.59% presented no statistically significant trends, and only 0.81% showed negative trends. Regarding the trends in the annual average extreme H_s , 2.02% of the sites on the 50 m isobath had positive trends, whilst 6.48% had negative trends. Only increasing wave heights, varying mostly in the range of 1–6 cm/decade along the New Zealand coastline, were documented by Godoi *et al.* (2016) when the mean of the whole spectrum of waves was analysed. This supports the idea that extreme and mean wave conditions should be treated separately, as done by Ruggiero *et al.* (2010).

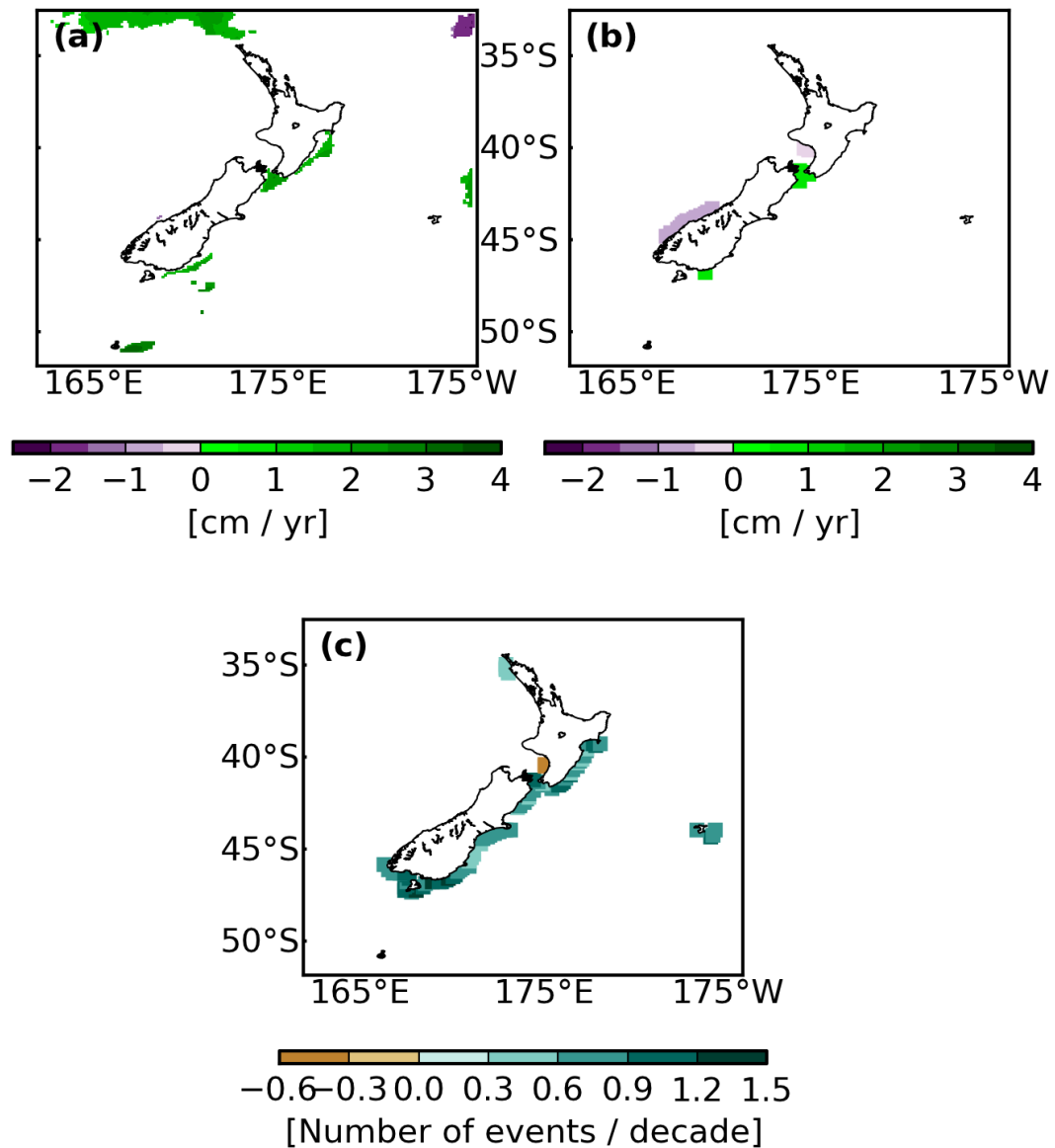


Figure 3.8. Monotonic trends in (a) annual maxima H_s ; (b) the annual average extreme H_s ; (c) the number of extreme wave events. Trends in (a) were computed for the whole regional domain of the 45-year wave hindcast, whereas in (b) and (c) they were calculated using POT data on the 50 m isobath. Only statistically significant values at the 95% confidence level were plotted. Significance was computed using p -value.

3.4 Extreme value analysis

Extreme value theory has been widely used for estimating return values from H_s datasets (e.g., Caires and Sterl, 2005; Hemer, 2010; Izaguirre *et al.*, 2011; Méndez *et al.*, 2006, 2008; Menéndez *et al.*, 2009; Vinoth and Young, 2011). Although several methodologies are available, there is no a universal approach that

suits all datasets. However, there are two commonly-accepted methods in general use: the generalised extreme value (GEV) model fitted to annual maxima (AM), and the generalised Pareto distribution (GPD) fitted to peaks-over-threshold (POT) (Coles, 2001). The reader is referred to the following literature for details of extreme value theory and the limitations and advantages of each method, Caires and Sterl (2005), Coles (2001), Ferreira and Guedes Soares (1998), Holthuijsen (2007), Mathiesen *et al.* (1994), Stephens and Gorman (2006), Vinoth and Young (2011), and Young *et al.* (2012).

The main drawbacks of the two aforementioned techniques are that the AM-GEV method requires long datasets to provide satisfactory estimates, not being practical for many oceanographic purposes (Young *et al.*, 2012), whereas the POT-GPD method needs arbitrary thresholds to be established, which can be problematic in certain circumstances (Mazas and Hamm, 2011). Firstly, identifying stability in the shape and scale parameters of the GPD is not always an easy task and requires experience. Secondly, one should ideally select the lowest threshold at which the GPD is valid, because higher thresholds generate fewer peaks with which the GPD parameters can be estimated, hence reducing the confidence in the return values (Caires and Sterl, 2005; Coles, 2001). By selecting a threshold lower than the lowest threshold at which the GPD is valid, non-extreme peaks (i.e., peaks that do not follow an extreme distribution) are included in the analyses, resulting in underestimated return values. Considering the duration (44 years) of our datasets, both methods seem to be reasonable candidates, hence they have been adopted here. In the case of the POT approach, a long dataset allows us to choose a high threshold in order to avoid its underestimation and ensure satisfactory fitting of the model cumulative distribution function (CDF) to the empirical CDF. Caires and Sterl (2005) state that if the GPD model is valid for peaks over a given threshold, it is also valid for peaks over higher thresholds with the same shape parameter and an adjusted scale parameter. The selected threshold (discussed below) provided about 3–6 H_s peaks per year at the 247 sites along the 50 m isobath, which is a typical number for extreme value analyses of environmental variables (e.g., Coles, 2001).

The use of percentiles to select thresholds is a common practice when dealing with several geographical locations and sufficiently long datasets. Different percentiles have been used in the literature, as, for example, the 90th and 97th used by Caires and Sterl (2005), the 90th and 93rd adopted by Vиноth and Young (2011), and the 99.5th used by Méndez *et al.* (2008). Here, the 99th percentile was selected to identify extreme events using the POT approach. As specified in section 3.2, the POT data are defined as maxima H_s (above the 99th percentile) from independent storms separated by a minimum interval of 72 hours. The 72-hour interval ensures independence between events, and was based on previous work, such as Alves and Young (2003), Méndez *et al.* (2006, 2008), and Stephens and Gorman (2006). Shorter intervals have also been chosen in the literature, such as the 48-hour interval considered by Harley *et al.* (2010) and Swail *et al.* (2006). The extreme value theory requires identical distribution of observations, which implies that waves generated by different atmospheric sources (e.g., cyclone, anti-cyclone, and trade winds) should be treated separately (Vиноth and Young, 2011). Given the number of sites and the relatively long period involved in the present analysis, it was not possible to meet the identical distribution criterion (also the case in other studies, such as Alves and Young (2003) and Stephens and Gorman (2006)). Nevertheless, the coastline orientation facilitates, to a certain extent, that waves generated by different atmospheric sources be separated into different populations, since weather systems affect some coasts more than others.

Finally, H_s return values were estimated for return periods of up to 100 years in the whole regional grid domain using the AM-GEV technique, and at the model grid points on the 50 m isobath using the POT-GPD approach. Both extreme models (GEV and GPD) were fitted to extreme H_s (annual maxima and POT data, respectively) employing the maximum likelihood method.

Very similar 100-year H_s return values were estimated by the two methods at the model grid points on the 50 m isobath (Figure 3.9). Their estimates were compared using two statistical metrics, the Pearson's correlation coefficient (R) and root-mean-square error (RMSE). Although the largest return values were slightly overestimated by the AM-GEV method in comparison to the POT-GPD method,

shown by the deviation of the points from the line of equivalence (1:1) at highest quantiles (Figure 3.9), a high degree of correlation was found ($R=0.99$) in addition to a relatively low RMSE (RMSE=0.17 m), meaning satisfactory agreement between the two datasets. Thus, the 100-year H_s return value estimates calculated at the model grid points along the 50 m isobath are shown only for the POT-GPD method (Figure 3.10a). The largest waves were estimated on the southwestern coast, followed by the west coast of the North Island. The southern and northeastern parts of the North Island also showed large wave estimates. On the other hand, the lowest estimates were obtained near the coastlines surrounding the strait between the two main islands (Cook Strait). The spatial pattern shown by the 100-year return values is similar to that found for the mean conditions, as seen in Godoi *et al.* (2016). Given the satisfactory agreement between both approaches for different wave climates along the 50 m isobath, it is expected that the other model grid points of the regional domain behave likewise. Thus, 100-year H_s return values were estimated for the whole regional domain using only the AM-GEV approach (Figure 3.10b).

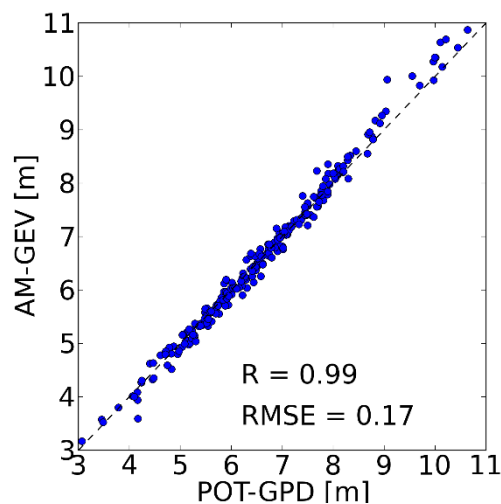


Figure 3.9. Quantile-Quantile comparison of H_s return values for 100-year return period estimated using both the Annual Maxima-Generalised Extreme Value Distribution (AM-GEV) and Peaks-Over-Threshold-Generalised Pareto Distribution (POT-GPD) approaches. Return values were estimated at the model grid points on the 50 m isobath. R and RMSE (m) stand for Pearson’s correlation coefficient and root-mean-square error, respectively.

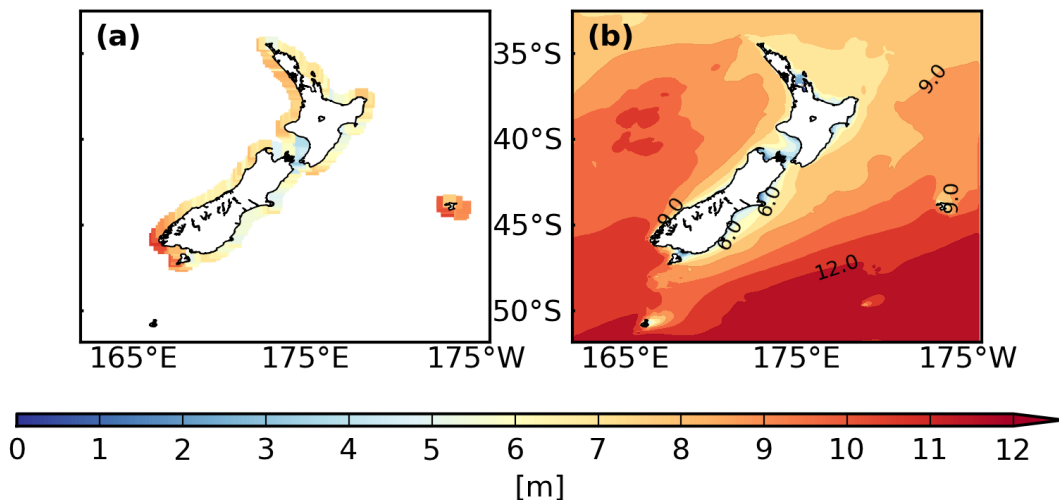


Figure 3.10. Significant wave height return values for 100-year return period (a) estimated at the model grid points on the 50 m isobath using the Peaks-Over-Threshold-Generalised Pareto Distribution approach; (b) estimated for the whole regional domain using the Annual Maxima-Generalised Extreme Value Distribution approach.

The spatial distribution of H_s return values (Figure 3.10b) again showed similar patterns to the mean H_s (Godoi *et al.*, 2016), in which the smallest waves are seen in regions sheltered from southwesterly swells, and the largest ones are observed south of New Zealand. Stephens and Gorman (2006) obtained the same result, but also reported smaller spatial variation compared to the spatial variation in the average waves. We estimated lower 100-year H_s return values than Stephens and Gorman (2006), with the difference being even greater to the south of New Zealand. Although uncalibrated modelled data have been used in both studies, it is important to highlight the considerably higher space-time resolution and longer record (more than twice as long) employed in the present analysis, both relevant characteristics for satisfactory return value estimation. Stephens and Gorman (2006) also used a different extreme value method (Mathiesen *et al.*, 1994), which has since been superseded in general practice by the methods used here. However, it is also worth emphasising that an underprediction by the model relative to buoy measurements is still present.

Three locations (Figure 3.1), where buoy records span more than 10 years, have been selected in order to compare H_s return values estimated from both the

model and buoy data (Figure 3.12). Due to the lengths of the buoy records being relatively short (< 16 years), the AM-GEV approach was disregarded, and only the POT-GPD method has been implemented. As the buoy records are not as long as the model time series, the threshold selection was initially based on the assessment of the stability of the shape and scale parameters obtained from the fitting of the GPD across a range of different thresholds, as demonstrated in Coles (2001). Nevertheless, this methodology provided almost identical return value estimates to when thresholds were selected based on the 99th percentile of the time series (not shown). Thus, the latter has been adopted in order to follow the same procedures applied to the model data. Before estimating H_s return values from the buoy and model data at the buoy sites, a validation of the matching peaks between these two datasets was carried out for overlapping periods (Figure 3.11). Again, the selection of H_s storm peaks was made based on the 99th percentile threshold of the whole time series and on a minimum interval of 72 hours between consecutive peaks. In general, the storm peaks identified in the buoy and model data did not match in time. Thereby, in order to make the validation process possible, buoy and model peaks were considered as matching peaks when they occurred less than 24 hours apart. Due to the relatively short overlapping periods in addition to gaps in the buoy data, only a few peaks could be used in the model validation. In total, 6 (black circles), 3 (green diamonds) and 23 (grey squares) matching peaks were identified at Baring Head, Banks Peninsula and Maui, respectively, during the approximately 3.5, 3 and 11 years of overlapping periods. Although calculating statistics from small samples (time series with only a few data points) is not ideal, and we do acknowledge the non-representativeness of these samples, they nevertheless provide an overview of how well the model reproduced the observed storm peaks during these specific overlapping periods. The validation was performed using the formulae of basic statistics (R, bias, RMSE, and scatter index (SI)) applied in Durrant *et al.* (2009). Not surprisingly, H_s peaks were generally underestimated by the model, as the bias values suggest (Figure 3.11). Additionally, the model did not present any clear trends regarding the magnitude of the

underestimates as the H_s peaks increased. The different sample sizes preclude comparing statistics between these three buoy sites.

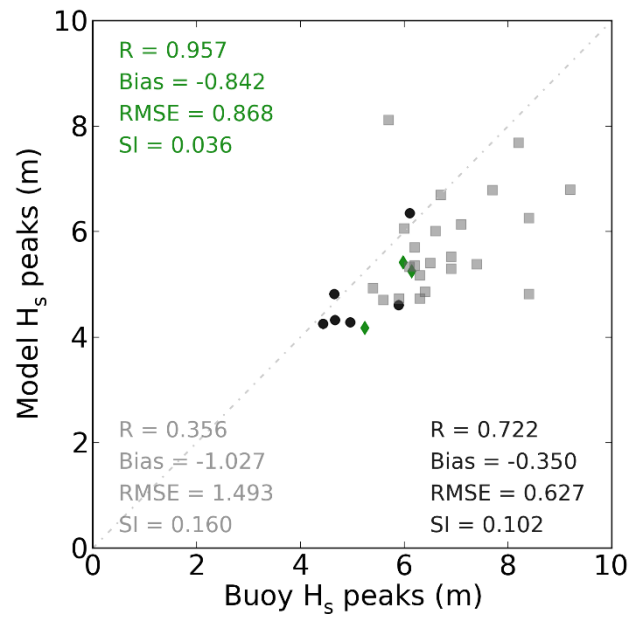


Figure 3.11. Validation of modelled significant wave height peaks during overlapping periods with buoy data for Baring Head (black circles), Banks Peninsula (green diamonds) and Maui (grey squares). Basic statistics (Pearson's correlation coefficient (R), bias in meters, root-mean-square error (RMSE) in meters, and scatter index (SI)) were calculated according to Durrant *et al.* (2009).

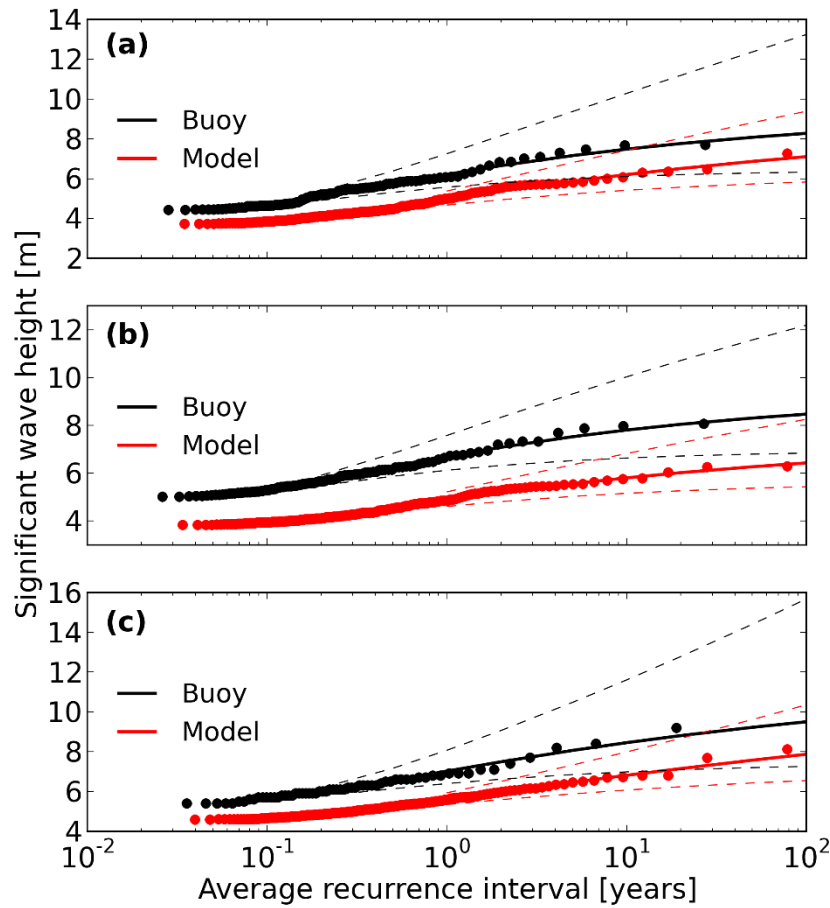


Figure 3.12. Significant wave height return values (solid lines) estimated from the buoy (black) and model (red) data (H_s peaks from independent storms above the 99th percentile) for (a) Baring Head; (b) Banks Peninsula; (c) Maui. Dashed lines represent confidence intervals at the 95% level estimated from the asymptotic covariance matrix of the maximum likelihood estimators. Dots represent the data plotted in their Gringorten plotting positions (Gringorten, 1963).

As expected, H_s return values estimated from the model data underestimated the ones calculated from the buoy data (Figure 3.12) by up to 24.12% for the 100-year return period (at Banks Peninsula). For the same return period, an average across the three sites indicates a bias correction of 18.58% for the model data. However, as briefly discussed in section 3.2, calibration of the model data based on limited buoy records is not recommended, especially when dealing with extreme events. Cavaleri (2009) lists several reasons why storm peaks are not properly captured by wave simulations. In addition to these, the hindcast was carried out using wind fields with relatively coarse space-time resolution and also

adopting a source term package (Tolman and Chalikov, 1996) that results in underestimation of the energy input during intense storm conditions dominated by young wind-sea (Ardhuin *et al.*, 2007). Moreover, H_s return values were computed from datasets spanning different periods of time. Lastly, as revealed by the trend analysis (Figure 3.8), trends in extreme H_s and in the number of extreme events have been detected, especially on the east coast, where two of the buoys are located. Despite all the issues and disregarding the estimates computed for Banks Peninsula, one notes that the 100-year estimates calculated from both datasets indicate a reasonable match when the confidence intervals are taken into account. The largest 100-year H_s return value calculated from the most reliable set of buoy measurements used in this work (buoy data from Maui) was 9.50 m (Figure 3.12c). Considering the error estimates, this value increases to approximately 16 m. This dataset was collected near the west coast of the North Island (Figure 3.1), whereas the largest waves occur in southern New Zealand. Therefore, for design purposes, it is not unreasonable to expect waves around New Zealand with H_s larger than 16 m, especially along the southwestern coast.

3.5 Discussion

Although it is beyond the scope of the present work to investigate the relationship between extreme wave events and climate patterns, some evidence of this connection is documented here and motivates future work.

The IAV of extreme H_s found in the central north coast of New Zealand (Figure 3.7b) is likely associated with La Niña episodes. Larger waves on the north coast have been reported during La Niña conditions (Godoi *et al.*, 2016; Gorman *et al.*, 2003a) as a consequence of stronger northeasterly winds (Gordon, 1986). Furthermore, tropical cyclones tend to be formed closer to the country during La Niña episodes (Revell and Goulter, 1986), and this might favour extreme waves, which in turn tend to be generated by local storms (Young *et al.*, 2011). A strong association between local storms and extreme waves was demonstrated by Young *et al.* (2011) through similar positive trends in wind speed and wave height for 99th percentile conditions. La Niña-like effects can be caused by at least three climate

patterns: the El Niño–Southern Oscillation (ENSO), the Pacific Decadal Oscillation (PDO), and the Indian Ocean Dipole (IOD) (Godoi *et al.*, 2016). Correlations between ENSO and PDO indices have been verified (Godoi *et al.*, 2016; Mantua *et al.*, 1997), suggesting that the PDO can influence the ENSO phases (La Niña and El Niño). The IOD can be externally triggered by the ENSO (Schott *et al.*, 2009), and indirect effects of the first can take place through the second owing to the correlation between these two modes. The opposite is also true, meaning that the IOD is able to promote conditions that facilitate the formation of the ENSO (Izumo *et al.*, 2010).

The negative trends observed in part of the west coast of the South Island (Figures 3.8a and 3.8b) contradict the increase in intensity of cyclones in the Tasman Sea reported by Simmonds and Keay (2000). One would expect stronger cyclones to be associated with an increasing trend in extreme H_s . On the other hand, the negative trend on the west coast found here might be related to a poleward shift of extratropical cyclone storm tracks (Gillett and Thompson, 2003), which is more likely to favour southerly waves (those that impact the east coast) than westerly ones. This poleward shift, consistent with the trend for a more positive SAM (Marshall, 2003), results in a southward displacement of wave generation zones. As a consequence, waves generated more to the south affect the east coast more than the waters immediately adjacent to the west coast, due to their propagation in great circles. Godoi *et al.* (2016) showed that, in terms of mean conditions, significant wave height (H_s) was positively correlated with the SAM on the south and east coasts of the country during the period 1958–2001, whereas a negative correlation was found on the waters immediately adjacent to the west coast, with both correlations being statistically significant. A similar pattern was found for more extreme conditions (top 10% H_s), although correlations with the SAM in the waters immediately adjacent to the South Island were not statistically significant. Moreover, decreasing/increasing trends in westerly/southwesterly waves on the west coast of New Zealand have been documented, in addition to increasing/decreasing trends in southerly/southeasterly waves on the east coast (Hemer *et al.*, 2010). Using satellite data, Young *et al.* (2011) noted statistically significant positive trends in extreme H_s in the region around New Zealand.

Nevertheless, the period (1985–2008) considered in their analysis was shorter than and different from ours, and they used a considerably coarser dataset than the ones employed here. It should be clear that climate trends identified in reanalysis datasets can be greatly influenced by temporal changes in the quality and quantity of the data assimilated into the model. Such changes were also introduced to the fields of the ERA-40 reanalysis (Bengtsson *et al.*, 2004; Uppala *et al.*, 2005) used to force the 45WH. Nonetheless, some of the trends detected here are in agreement with trends reported by authors (e.g., Marshall, 2003; Young *et al.*, 2011) who used data from meteorological stations and satellite altimeters. Furthermore, Marshall (2003) stated that ERA-40 can be used with high confidence, at least as far back as 1973, to examine the recent trend in the SAM, whose main signature occurs in the high latitudes of the Southern Hemisphere. High and mid-latitudes comprise the main wave generation zones responsible for the formation of the waves that consistently impact on the New Zealand coastline.

3.6 Conclusion

Based on 44 years (1958–2001) of a high resolution wave hindcast, an extreme wave climatology and extreme value estimates were established for New Zealand waters. Monthly and seasonal climatologies, mean annual and inter-annual variabilities, and trend analyses compose the extreme wave climatology. Extreme predictions were carried out employing two different approaches, the POT-GPD and AM-GEV. Their results were compared, and the POT-GPD estimates were in addition compared to estimates conducted from buoy data at three specific locations.

The extreme H_s and mean H_s (Godoi *et al.*, 2016) spatial patterns are similar in both offshore and coastal areas, with the roughest seas found in southern New Zealand and calmer conditions observed in regions sheltered from southwesterly swells. This was observed not only in climatological parameters, but also in estimates of H_s return values. Nevertheless, some differences, such as high energetic waves on the northwestern coast in January as well as the intensity of events, stress the importance of exploring extreme and mean conditions separately.

The time of the year and coastline exposure to generating regions are key factors in determining the frequency of extreme events. Except for the north coast, New Zealand was hit by a large number of events in May, while they were least frequent in January and February. Extreme H_s had little seasonal variation, but closely-spaced extreme conditions were more/less frequent in winter/summer around the whole country. Regions where locally-generated storms control the extreme wave climate presented greatest MAV. Given that the IAV of mean wave conditions is correlated with La Niña-like effects on the north coast, which might have different sources (ENSO, IOD and PDO), and with the SAM on the east coast, it is likely that the IAV of extreme H_s is also driven by these oscillations. Statistically significant negative trends in extreme H_s were detected in parts of the west coast of the South Island, indicating a possible relationship with the poleward shift of extratropical cyclone storm tracks (Gillett and Thompson, 2003). Increasing trends detected in parts of the east coast of the same island suggest an association with positive trends in the SAM (Hemer, 2010; Marshall, 2003). The latter also seems to be related to the increasing frequency of extreme waves on the east and south coasts of New Zealand. These assumptions regarding relationships between climate patterns and the extreme wave climate around New Zealand deserve further investigation.

Analogous results were obtained by the POT-GPD and AM-GEV methods when comparing 100-year H_s return values, although the AM-GEV method estimated slightly larger waves at the highest quantiles. Estimates computed from the model data were lower than those calculated from the buoy data for Baring Head, Banks Peninsula and Maui as a result of several factors. These include model inputs with coarse space-time resolution, selection of a source term package (Tolman and Chalikov, 1996) that results in underestimation of the energy input during intense storm conditions dominated by young wind-sea (Ardhuin *et al.*, 2007), and datasets spanning different periods of time.

As stated by Mathiesen *et al.* (1994), water level statistics become important in estimating extreme waves at shallow-water locations, and these were not considered here. Several factors can potentially threaten coastal areas in New

Zealand, such as land subsidence due to groundwater withdrawal, sea-level rise (Bell *et al.*, 2000; Hannah, 2004), and mangrove forests degradation or removal (although relatively uncommon in New Zealand, mangrove forests degradation and/or removal have occurred in isolated episodes – Morrisey *et al.*, 2007; Stokes and Harris, 2015). These combined with extreme wave events result in an increased risk for the expanding coastal population of the country and its associated industrial, residential and tourism developments. Therefore, the results presented here may contribute significantly to safety and economic strategies in addition to providing relevant information for climatological applications.

Contributions of the author and co-authors to Chapter 4

I was responsible for the data processing, data analysis, and writing. Karin R. Bryan and I came up with the idea of the topic addressed in this chapter. I defined the methodology employed.

Richard M. Gorman produced and validated the hindcast results employed in Chapter 4.

Karin R. Bryan and Richard M. Gorman reviewed Chapter 4 and made suggestions regarding the writing.

CHAPTER 4: Relationships between storm wave clustering conditions around New Zealand and climate patterns

4.1 Introduction

A combination of swell and locally-generated waves is frequently observed along open coastlines influenced by different meteorological systems (Harley *et al.*, 2010). Such coastlines are highly impacted by storm waves, which in turn are potentially more hazardous when arriving in clusters because the intervals between the events are not sufficiently long for the beach to recover (Lee *et al.*, 1998; Senechal *et al.*, 2017). When propagating in clusters, storms with relatively short return periods can cause damage equivalent to or greater than that from a single storm with far longer return period (Ferreira, 2005). Consequently, clustered storms may produce catastrophic events in populated coastal areas. Therefore, an improved knowledge of storm wave clusters (SWCs) and of the changes in the frequency and magnitude of these systems over time is needed to support coastal management.

From a meteorological point of view, a cluster is characterised by unstable atmospheric waves that develop and move rapidly along the wake of a large low-pressure system (Mailier *et al.*, 2006). From an oceanographic-morphodynamic point of view, a storm cluster can be defined as two or more consecutive storms between which there is insufficient time for the beach to recover from erosion (Ferreira, 2006). Atmospheric serial storms have been shown to have devastating effects on the European economy (e.g., Mailier *et al.*, 2006; Pinto *et al.*, 2013; Pinto *et al.*, 2014); Past work has also associated cyclone clustering (Mailier *et al.*, 2006; Economou *et al.*, 2015) and clustering of flooding events (Villarini *et al.*, 2013) with climatic patterns, such as the North Atlantic Oscillation. However, SWCs have been explored less because of the lack of data. Therefore, both their nearshore and offshore characteristics are still poorly understood. Despite that, they have been

shown to play a role in the evolution of a number of coastal features, such as cliffs (Nunes *et al.*, 2011), megarips (Loureiro *et al.*, 2012), dunes (Benavente *et al.*, 2013; Dissanayake *et al.*, 2015a, 2015b, 2015c), and shoreline cusps (Balouin *et al.*, 2013).

Several techniques to identify groups of cyclones have been implemented, such as a Bayesian approach (Fawcett and Walshaw, 2008), a running sum of daily cyclone counts (Pinto *et al.*, 2014), and the calculation of a dispersion statistic based on the Poisson process and cyclone counts (Mailier *et al.*, 2006; Kvamstø *et al.*, 2008; Vitolo *et al.*, 2009). Studying cyclone clusters, however, does not necessarily provide useful information on the formation of SWCs. Large waves might not be generated if cyclones change direction continuously along their tracks, since the generation of large waves depends on persistent strong unidirectional winds.

In the past, SWCs were evaluated by measuring the beach morphodynamic response to a sequence of storms. This has been done mainly through either beach profile assessments (e.g., Lee *et al.*, 1998; Loureiro *et al.*, 2009; Karunarathna *et al.*, 2014; Coco *et al.*, 2014) or detailed numerical or empirical modelling of erosion (e.g., Vousdoukas *et al.*, 2011; Splinter *et al.*, 2014; Dissanayake *et al.*, 2015a, 2015b, 2015c), although other approaches have also been implemented, such as the analysis of ARGUS video imaging (Phillips *et al.*, 2015) and the use of the convolution model of Kriebel and Dean (1993), applied by Ferreira (2002). These techniques either require long records of consistently-monitored beach profiles or are computationally-expensive and time-consuming. Most of the studies quoted above used beach recovery periods (i.e., the average time interval the beach takes to recover substantially after an erosion) to identify SWCs. Beach erosion and recovery are not trivial to ascertain because they require surveying before, during and after each storm within the cluster. The local intensity of the storm, the beach state, the tide conditions, and the type and availability of sediment have a strong influence on variability of the beach recovery period, making it highly site-dependent. Furthermore, slightly different combinations of these parameters can lead to significantly different erosion and recovery responses, especially when the initial stage has already been disturbed (Coco *et al.*, 2014). For these reasons, SWCs have been analysed only at a particular beach or, at most, at several beaches.

Considerable variation exists in the time thresholds that determine which storms belong to a single cluster. For example, Birkemeier *et al.* (1999) grouped storms that occurred up to 40 days apart at Duck (USA). Ferreira (2005) stated that either 21 days between storm peaks or 14 days between the end of a storm and the beginning of the subsequent one was enough to ensure that beaches would not recover significantly at his study sites, in Portugal. Karunarathna *et al.* (2014) considered a 9-day cut-off to define clustered storms at Narrabeen Beach (Australia), whereas Almeida *et al.* (2012) aggregated storms that occurred less than 10 days apart on the Portuguese coast.

Located at the interface between the Pacific and Southern Oceans, with the Tasman Sea to the west, patterns of storm clustering around New Zealand are likely to be complex, depending on the origin of generating weather systems. As an island nation, New Zealand is reliant on shipping for trading goods. Moreover, the implementation of recent trade agreements (summarised in, e.g., World Bank Group, 2016) has led to increased ship traffic, and the energetic seas surrounding New Zealand (Gorman *et al.*, 2003b) mean that assessing conditions and providing predictions for maritime safety has become increasingly important. New Zealand's mid-latitude position and distance from other landmasses allow several weather systems to affect the country, causing frequent storms and extreme wave events (Godoi *et al.*, 2017). These wave conditions have been shown to vary considerably in association with climate patterns (Godoi *et al.*, 2016). Changes in the Southern Hemisphere atmospheric circulation related to the Southern Annular Mode (SAM) (Thompson and Solomon, 2002), such as a poleward shift of the westerly jet and associated fields (Kushner *et al.*, 2001), affect New Zealand directly. The SAM is the dominant mode of atmospheric variability in the Southern Hemisphere (Marshall, 2003) and is associated with the formation of extratropical cyclones, the main source of the storm waves that affect the New Zealand coastline. However, SWCs and their characteristics have not been investigated in the New Zealand region yet. The lack of high temporal resolution beach profiles and other datasets for most New Zealand beaches limits the ability to study clustering through erosion

responses. As a first step, we use our long-term (1957–2002) wave hindcast (Gorman *et al.*, 2010) to investigate the drivers of storm clustering.

Given the recognised threat posed by SWCs to coastal environments and infrastructure, as well as to offshore operations (e.g., oil rigs and fishery boats), this chapter explores the relationships of SWCs to climate patterns in New Zealand waters. A SWC climatology supports not only the monitoring and management of coastal areas in terms of flooding and sediment transport, but also the planning of naval and marine operations, besides assisting in the selection of sites for wave energy extraction. Our investigation was carried out using the results of our long-term wave hindcast and considers how conditions might change in association with five climate patterns, as characterised by the El Niño–Southern Oscillation (ENSO), Indian Ocean Dipole (IOD), Southern Annular Mode (SAM), Pacific Decadal Oscillation (PDO), and Zonal Wavenumber-3 Pattern (ZW3). Firstly, duration and number of clusters in addition to the potential for cluster-induced coastal erosion were assessed through average values computed over the period 1958–2001. To account for changes in the frequency and magnitude of SWC generating systems (cyclones) and those changes that have an indirect impact on them, like changes in atmospheric ozone and greenhouse gases (Arblaster and Meehl, 2006), monotonic trends in SWC parameters (cluster duration, number of storms within the cluster, and cumulative storm energy) were calculated. Then, correlations of climate indices with clustered storms and SWC parameters were carried out at multiple timescales to better understand the causes of variability in clustering.

4.2 Methodology

A 45-year (September 1957 – August 2002) wave hindcast (Gorman *et al.*, 2010), hereafter 45WH, was conducted using version 3.14 (Tolman, 2009) of the WAVEWATCH III model (Tolman, 1991) forced with wind and ice fields from the ERA-40 reanalysis (Uppala *et al.*, 2005). A regional domain, with $0.125^\circ \times 0.09375^\circ$ spatial resolution, was one-way nested within a global domain at $1.125^\circ \times 1.125^\circ$ resolution. The regional domain encompassed the waters surrounding New Zealand, which include part of the Tasman Sea and parts of the Southern Ocean

and southwestern Pacific Ocean (Figure 4.1). Results of the simulation were output at 1 h and 3 h intervals for the regional and global domains, respectively, and then validated against satellite altimetry data from the TOPEX/Poseidon, ERS1 and ERS2 missions, and against buoy measurements from sites around New Zealand and North America. Details of the 45WH can be found in Gorman *et al.* (2010) and Godoi *et al.* (2016).

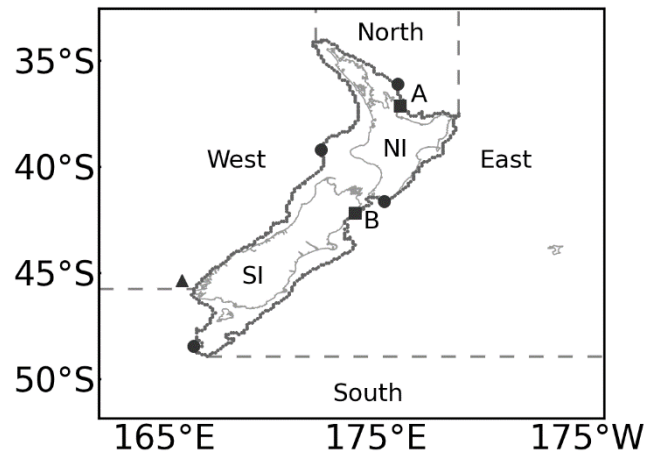


Figure 4.1. Regional domain of the 45-year (1957–2002) wave hindcast. Filled circles represent the locations used in the wavelet spectral analysis. Filled squares A and B indicate the sites used as examples for showing time series of occurrence of clustered storms in Figure 4.2b and 4.2c, respectively. Grey dots illustrate the model grid points on the 200 m isobath, with the filled triangle marking the first point (0) of the sequence of Figure 4.2a. Dashed lines represent coastline delimiters, plotted here as a guide for Figure 4.2a. NI and SI stand for North Island and South Island, respectively.

Modelled time series of significant wave height (H_s) were extracted from the 45WH at the 418 model grid points on the 200 m isobath around New Zealand (Figure 4.1) for the 44-year period 1958–2001. A range of H_s thresholds has been selected in the literature to define storm waves (Ferreira, 2005), usually based on the wave climate of the study region. As different wave climates are found along the New Zealand coastline (Godoi *et al.*, 2016, 2017), H_s thresholds should vary accordingly. A simple way of obtaining H_s thresholds that match the local wave climate is to select them based on percentiles rather than establishing a single

value for the whole study region. Thus, storm wave events were identified using the Peaks-Over-Threshold (POT) approach considering the 95th percentile threshold of each site. In other words, H_s maxima from independent storms were obtained when they were above the 95th percentile of the time series, following, e.g., Phillips *et al.* (2015) and Harley *et al.* (2009). A timeframe also needs to be considered for ensuring independence between storms, since successive H_s peaks occurring in a short interval are likely to be part of the same event. To this end, H_s maxima were selected only when they occurred at least 72 hours apart. The 72-hour interval was motivated by past studies where 72 hours is the time lag below which the storms are autocorrelated (Mathiesen *et al.*, 1994; Lopatoukhin *et al.*, 2000). This is a well-established threshold in the literature, used in the identification of both storm and extreme waves (Alves and Young, 2003; Stephen and Gorman, 2006; Méndez *et al.*, 2006; Godoi *et al.*, 2017).

Here, we aim at understanding some general characteristics of SWCs around the whole coastline of New Zealand. This is unlikely to be accomplished with the implementation of the techniques discussed in the previous section because they require beach recovery periods to be defined. Therefore, a simple and objective criterion has been chosen to assess storm wave clustering without considering erosion processes and recovery periods of individual beaches. This criterion is based on the assessment of the index of dispersion (I_d) of time intervals between storm peaks.

The I_d is a measure of the normal variability of intervals between storm peaks, and is the quantity (with time dimension) defined as the ratio of the variance $\langle(\Delta T - \langle\Delta T\rangle)^2\rangle$ of the time interval ΔT between storm peaks to the mean interval $\langle\Delta T\rangle$. The method itself is not innovative, since it has been applied by other authors (Mailier *et al.*, 2006; Kvamstø *et al.*, 2008; Vitolo *et al.*, 2009) in different contexts and using different approaches. However, the way the method has been employed here differs from previous work. Two assumptions were made in order to select appropriate values for the time interval between storm peaks used for grouping storms into clusters. This interval needed to be short enough to be considerably lower than both the I_d value and the mean interval at each location analysed, and

long enough to allow SWCs to be identified. Values of $0.5I_d$ were found to satisfy both requirements for all time series of storm wave occurrence assessed, as shown in Figure 4.2a. Hence, they have been adopted in this work, and storms were grouped into clusters when the time interval between them was shorter than $0.5I_d$. Sensitivity tests for intervals equal to $0.4I_d$ and $0.6I_d$ were also conducted to verify the variability of the overall mean of the number of SWCs in the study region during the period 1958–2001 (not shown). The overall mean values did not change considerably (133.8, 140.7, and 139.9 for $0.4I_d$, $0.5I_d$, and $0.6I_d$, respectively) because SWCs became generally longer rather than more numerous when the intervals increased, whereas the number of SWCs only slightly reduced when the intervals were shortened. So, our original choice ($0.5I_d$) was kept. Values of $0.5I_d$ varied between 9.7 and 25.4 days, with an average of 15.1 days among all sites. Although the beach recovery period is not a key factor in the determination of SWCs in our analysis, values of $0.5I_d$ were found to be within the range of beach recovery periods proposed in the literature (Birkemeier *et al.*, 1999; Ferreira, 2005; Almeida *et al.*, 2012; Karunarathna *et al.*, 2014). Figure 4.2a shows the values of $0.5I_d$ (dashed line), the mean interval (solid line), and the standard deviation of the time interval (dotted line) calculated for each of the 418 model grid points on the 200 m isobath over the period 1958–2001. The standard deviation of the time interval between storm peaks was plotted instead of its variance to allow better visualisation of the values of the other curves. One notes that the values of the standard deviation were generally closer to the mean values on the north coast than on the other coasts (Figure 4.2a). This indicates a smaller variability in storm occurrence (more consistent wave climate) on the north coast than on the others, which results from a typically low-energy wave environment on the north coast that is regularly disturbed by tropical cyclone-generated waves in summer (Godoi *et al.*, 2016). Examples of clustering at sites A and B (Figure 4.1) during the 1970s are displayed in Figure 4.2b and Figure 4.2c, respectively. The examples show the temporal distribution of clustered and non-clustered storm occurrences identified at the sites with the largest (site A) and smallest (site B) differences (16.6 and 5.5 days) between the mean interval between storm peaks and $0.5I_d$. By using this

approach, for two sites with the same mean interval between storm peaks, the one with a less consistent wave climate (larger variability in the time interval between storm peaks) will have a higher I_d value and, consequently, more clustered storms. In this case, a higher I_d means a higher chance of erosion or any other cluster-induced damage as well as a higher chance of multi-hazard effects, since the longer duration of SWCs relative to individual storms will mean that conditions will be more likely to coincide with a high tide.

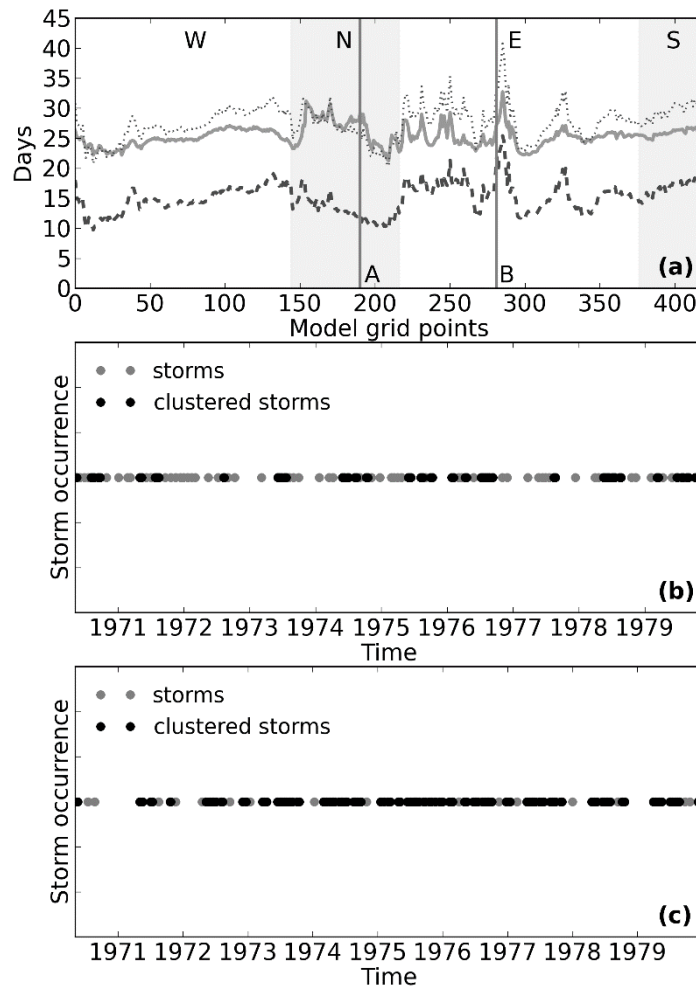


Figure 4.2. (a) Statistics computed for time series of storm wave occurrence at the 418 model grid points on the 200 m isobath: half of the index of dispersion of time intervals between storm peaks (dashed line), mean interval between storm peaks (solid line), and standard deviation of the time interval between storm peaks (dotted line). Vertical lines A and B mark the largest and smallest differences between the mean interval between storm peaks and half of the index of dispersion; the locations of the model grid points associated with these differences are displayed in Figure 4.1 as A and B. W, N, E, and S stand for west, north, east, and south, respectively, delimited according to Figure 4.1. Shaded and non-shaded areas of the graph comprise the model grid points along each section of the coastline (W: 0-143; N: 144-216; E: 217-375; S: 376-417), with 0 being located on the southwestern coast (triangle in Figure 4.1) and the subsequent numbers follow a clockwise rotation; (b) Time series of occurrence of storms and clustered storms at site A; (c) Time series of occurrence of storms and clustered storms at site B. Grey circles represent storm waves, whereas black circles indicate storm waves pertaining to clusters.

Although the focus of this chapter is not on beach processes, such as erosion and sediment transport, two measures, based on offshore H_s and storm duration (period in which H_s remained above the 95th percentile), were used to provide an overview of the potential for coastal erosion. These were the average cumulative storm energy per cluster and average storm power index per cluster. Both the cumulative storm energy (CSE) (Mendoza and Jimenez, 2006; Harley *et al.*, 2009, 2010; Phillips *et al.*, 2015) and storm power index (SPI) (Dolan and Davis, 1994; Karunarathna *et al.*, 2014) were first calculated for each storm. To do so, the formulae presented by Harley *et al.* (2010) and Karunarathna *et al.* (2014) were employed here (Equations (1) and (2), respectively); where ρ is the mass density of sea water (1025 kg/m^3), g is the gravitational acceleration (9.8 m/s^2), Δt is the temporal resolution of the dataset (1 h), v is the total number of H_s values i above the 95th percentile during the storm, $H_{s_{max}}$ is the storm peak H_s value, and D is the storm duration. The cumulative effect of all storms pertaining to a single cluster was determined by summing up their respective CSE/SPI values. Lastly, the cumulative energy obtained for all SWCs of each site on the 200 m isobath was temporally averaged over the period 1958–2001. The SPI overestimates the energy content of a storm because it only considers the maximum H_s (Mendoza and Jimenez, 2006). Conversely, H_s of each recording time during a storm is used in the computation of the CSE. Nonetheless, for the sake of the ability to compare to studies that have applied the SPI, this is also calculated here.

$$CSE = \frac{1}{16} \rho g \Delta t \sum_{i=1}^v H_{s_i}^2 \quad (1)$$

$$SPI = H_{s_{max}}^2 D \quad (2)$$

To verify changes in SWCs over the period 1958–2001, trends in annual averages of SWC parameters (number of storms within the cluster, CSE, and cluster duration) were calculated using the Mann-Kendall test (Mann, 1945; Kendall, 1955) and the Theil-Sen estimator (Theil, 1950; Sen, 1968). The Mann-Kendall test was employed to estimate monotonic upward/downward trends, while the Theil-Sen estimator was used to calculate the slope (magnitude) of the trends. Trends were

computed for three time periods: the pre-satellite (1958–1978) and satellite (1979–2001) eras spanned by the dataset, and a long-term period (1958–2001). Statistical significance of trends was assessed using p -value.

Storm wave clustering during different phases of the ENSO, IOD, SAM, PDO, and ZW3 was investigated through correlations of the climate pattern indices (Southern Oscillation Index (SOI), Dipole mode Index (DMI), SAMI, PDO index, and ZW3 index) with storm cluster indices (explained below) and SWC parameters. Monthly climate indices were sourced from the National Oceanic and Atmospheric Administration (NOAA), Japan Agency for Marine-Earth Science and Technology (JAMSTEC), British Antarctic Survey (BAS), Japan Meteorological Agency (JMA), and Raphael (2004), respectively. Except for the ZW3 index, which is available only from 1979, all the other climate indices were collected for the period 1958–2001. In order to perform the correlations, a monthly storm cluster index was created for every location analysed by assigning weights to each month based on the number of clustered storms within that month. Firstly, the number of storms in each month of the 44-year period was found using the POT approach and the 72-h interval, and those that were clustered were identified using the index of dispersion (as described above). This resulted in two time series, a monthly time series of the number of storms and a monthly time series of the number of clustered storms. Then, the latter was divided by the former yielding a monthly storm cluster index. The same procedure was carried out for the 418 sites on the 200 m isobath. Then, correlations of monthly anomalies between the storm cluster indices and climate indices were performed. Additionally, seasonally-averaged monthly anomalies of storm cluster indices were correlated with both seasonal and lagged-seasonal (1-season lag) averages of monthly anomalies of climate indices. Lastly, correlations of annually-averaged monthly anomalies between SWC parameters (number of storms within the cluster, CSE, and cluster duration) and climate indices were carried out. Correlations were performed using the Pearson's correlation coefficient (R). As demonstrated by Godoi *et al.* (2016, 2017), and Pickrill and Mitchell (1979), the mean and extreme wave climates around New Zealand can be classified into four main wave climates according to their exposure to wave generation zones.

Thus, four model grid points on the 200 m isobath (48.469°S/166.375°E, 39.188°S/172.375°E, 36.094°S/176.000°E, and 41.625°S/175.375°E), corresponding to the major coastline orientations (Figure 4.1), were selected so that correlations of monthly anomalies between their storm cluster indices and climatic indices could be computed at several timescales using the squared wavelet coherence spectra.

4.3 Overview of storm wave clustering around New Zealand

SWCs were most frequently observed to the northeast of New Zealand and on the central eastern coast of the South Island (Figure 4.3a), where approximately 4 SWCs occurred per year. Karunarathna *et al.* (2014) identified 80 SWCs at Narrabeen Beach between 1981 and 2000, resulting in 4 SWCs per year on average. Their results are comparable to our sites with largest occurrences of SWCs (the authors note SWCs are fairly common at Narrabeen Beach). Interestingly, wave conditions at both Narrabeen Beach, on the east coast of Australia, and the northeast coast of New Zealand are affected by tropical cyclones. Although these regions have different coastline orientations and, in general, different weather systems control their wave climates, their equivalent annual average number of SWC in addition to their locations suggest important contributions from tropical cyclones. On the other hand, Narrabeen Beach and the central eastern coast of the South Island have similar coastline orientations (E/SE). Additionally, both regions are impacted by swells generated by extratropical cyclones propagating over the Southern Ocean. However, tropical cyclones rarely influence the wave climate of the central eastern coast of the South Island. A detailed investigation is required to confirm relationships between the SWCs that occur at Narrabeen Beach and those that arrive in New Zealand. This is necessary because of the distances from these regions to wave generation zones and because of the dispersion of waves as they propagate out of generating areas.

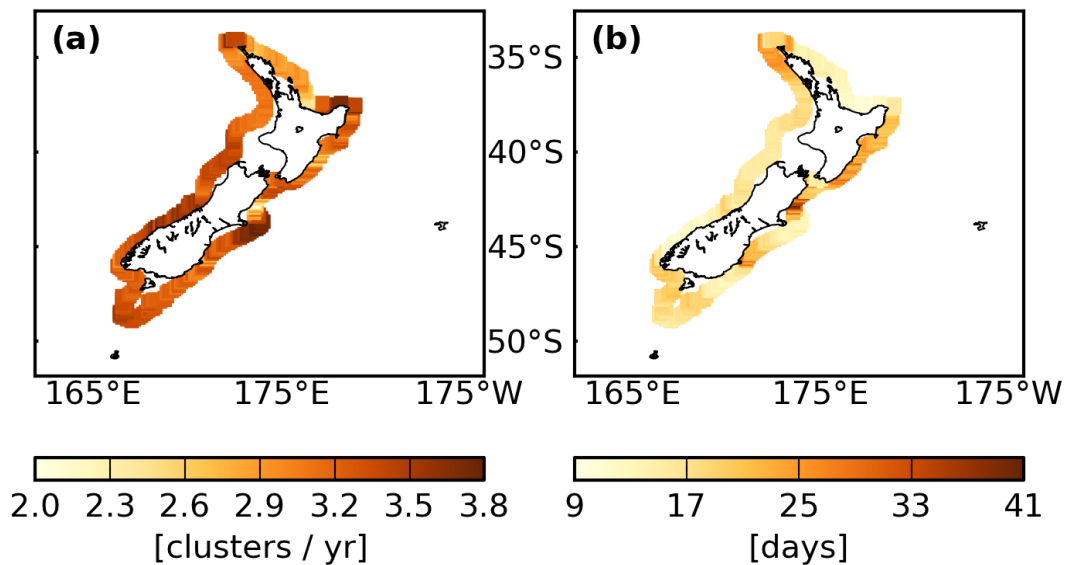


Figure 4.3. Considering the period 1958–2001: (a) annual average number of storm wave clusters; (b) average storm wave cluster duration. The averages were calculated at the model grid points on the 200 m isobath.

A secondary maximum in cluster occurrence was experienced on the central western coast of the South Island. This agrees with the extreme wave conditions documented by Godoi *et al.* (2017), who showed that extreme waves are more closely-spaced in this region and on the northeastern coast than in other regions around the country. A common feature between these two regions is that swells from the south quadrant undergo considerable refraction prior to arriving at the coast. SWCs had generally longer durations on the east coast than on the other coasts (Figure 4.3b). They were least frequent (Figure 4.3a) where they lasted longest (Figure 4.3b), up to about 40 days on average, as can be noted to the north of the large peninsula on the central eastern coast of the South Island. This segment of the coastline is sheltered from the main swell direction (SW) and presents a relatively low-energy wave climate (Godoi *et al.*, 2016, 2017).

As expected, both the average CSE per cluster and average SPI per cluster (Figure 4.4) showed a similar spatial distribution of potential for cluster-induced coastal erosion. These results highlight the regions around the country where SWCs played the most critical role in terms of coastal hazards, which were southern New Zealand followed by the west coast of the North Island. This is directly related to

the intense activity of southwesterly swells generated by recurrent extratropical cyclones (Sinclair, 1995). Karunarathna *et al.* (2014) obtained values between 2.86 and 73.83 hm^2h for the SPI per cluster for events representative of the scale of beach profile change at Narrabeen Beach. Their range was 45.4% larger than ours (4.17–52.99 hm^2h). Regarding the average CSE values per cluster, 59% of the sites we investigated were less than 1.19 MJh/m^2 , while 12% were in the most hazardous condition range (2.17–2.67 MJh/m^2) (Figure 4.4b).

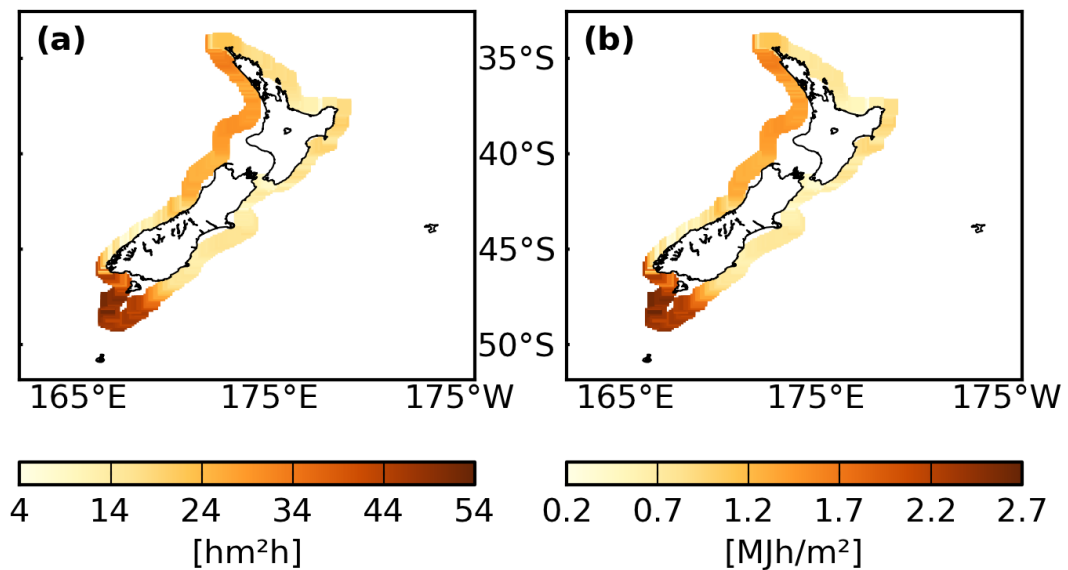


Figure 4.4. Measures of the potential for cluster-induced coastal erosion: (a) average storm power index per cluster (in hecto m^2h); (b) average cumulative storm energy per cluster (in mega Jh/m^2). The averages were calculated using all storm wave clusters occurred during the period 1958–2001 for each model grid point on the 200 m isobath.

The 45WH was carried out using reanalysed data from ERA-40 as boundary conditions. The quantity and quality of such data vary in time, and this may produce spurious trends. Under these circumstances, the well-known temporal inhomogeneity issue, concerning the introduction of satellite data to the reanalysis dataset (Bromwich and Fogt, 2004), was explored by evaluating trends for different periods. Contrasting results were obtained when trends in SWC parameters were calculated for the pre-satellite (1958–1978) and satellite (1979–2001) eras (Figure 4.5 – left and middle columns, respectively). Trends were generally positive during

the pre-satellite period and negative during the satellite period, although only a low percentage of the analysed sites had statistically significant results (7.42% [4.31%] of the sites showed statistically significant results for trends in CSE during the period 1979–2001 [1958–1978], while the percentages were even lower for trends in the other parameters). Note that opposing trends were generally observed at different locations, suggesting that these can also be due to different climate conditions in the two periods rather than due to data inhomogeneity in the reanalysis. By using only satellite data over the period 1985–2008, Young *et al.* (2011) detected only positive trends in the 99th percentile H_s in the region around New Zealand.

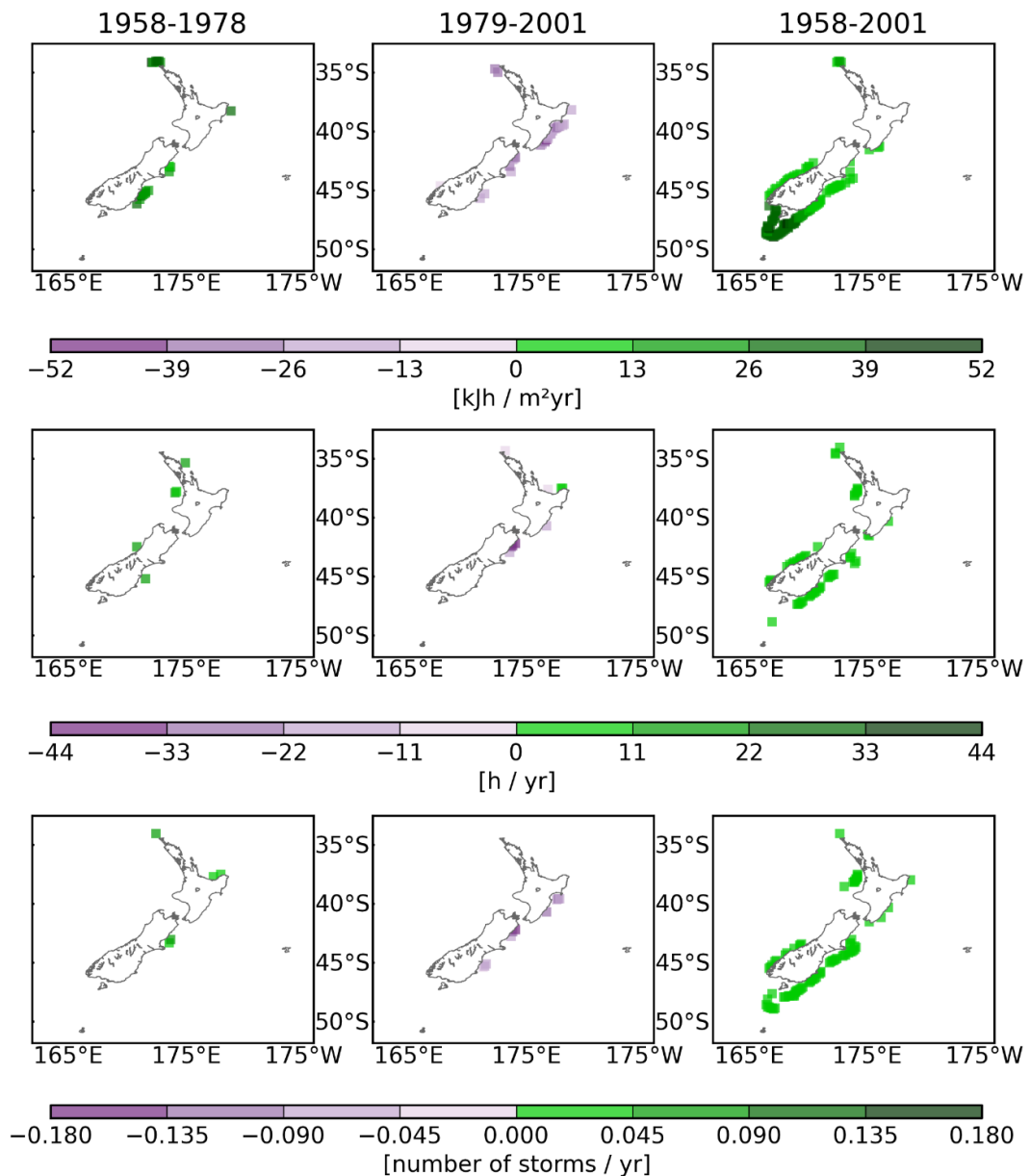


Figure 4.5. Monotonic trends in storm wave cluster parameters, calculated for the pre-satellite period (1958–1978, left column), satellite period (1979–2001, middle column), and long-term period (1958–2001, right column). Top row: cumulative storm energy (in kilo Jh/m²); middle row: cluster duration; bottom row: number of storms within the cluster. Trends were calculated from annual averages of the cluster parameters using the Mann-Kendall test and the Theil-Sen estimator. Only statistically significant values at the 95% confidence level (calculated using p -value) are displayed.

When trends were calculated for the period 1958–2001 (Figure 4.5 – right column), only positive trends were identified, in which case SWCs have become more hazardous, have lasted longer, and have incorporated more storms. Trends

were mostly observed around the South Island, with only a few locations along the North Island (the northernmost and southernmost tips) with statistically significant trends for all parameters (Figure 4.5 – right column). Nevertheless, several sites off the central western coast of the North Island also showed notable trends in cluster duration and in the number of storms within the cluster. Southern New Zealand is not only where the highest potential for cluster-induced coastal erosion was found (Figure 4.4), but also where its largest trends were detected (Figure 4.5 – right column, first row). At some sites in this region, trends might result merely from increasing wave heights (Godoi *et al.*, 2016) and/or changes in wave direction (Hemer *et al.*, 2010), while at other sites, they were associated with an increasing number of storms within the cluster (Figure 4.5 – right column, third row). For the same period (1958–2001), positive trends in the mean H_s were reported for southern New Zealand (Godoi *et al.*, 2016), whereas no trends in extreme waves (maxima H_s above the 99th percentile from independent storms) were observed (Godoi *et al.*, 2017). On the other hand, trends in extreme waves were found along the southeastern coast (Godoi *et al.*, 2017), where increasing trends in energy content, cluster duration, and in the number of storms within the cluster were also detected (Figure 4.5 – right column). Increases in intensity of cyclones in the Tasman Sea (Simmonds and Keay, 2000) are likely related to the trends in the SWC parameters observed on the west coast of the South Island (Figure 4.5 – right column). The latter, however, contradict the trends in directional distribution of waves, which indicate a reduction in northwesterly and westerly waves arriving on this coast (Hemer *et al.*, 2010). The contradicting results between the pre-satellite and satellite eras do not allow us to provide robust detection of the long-term trends. Nonetheless, trends were computed using results from a wave hindcast forced by ERA-40 data, which in turn were found to be suitable for analysing the recent trend in the SAM, at least as far back as 1973 (Marshall, 2003). This provides additional confidence in the long-term trends, since the main signature of the SAM takes place in the high and mid-latitudes of the Southern Hemisphere, where the waves that consistently affect New Zealand are generated.

Trends for a negative SOI after 1976 (Trenberth and Hoar, 1996), for a positive SAM since the mid-1960s (Marshall, 2003), and for a positive PDO since mid-1970s (Pezza *et al.*, 2007) have been documented. These were also verified here for the period 1958–2001 (Figure 4.6), and are in agreement with increases in SWC parameters (as discussed in the next section). The long-term trends identified in those climatic indices only explain a small portion of the variance, which is, for many purposes, less important than the short-term variability. However, when dealing with coastal hazards and flooding, even a small long-term change in storms and extreme events will potentially lead to increased damage.

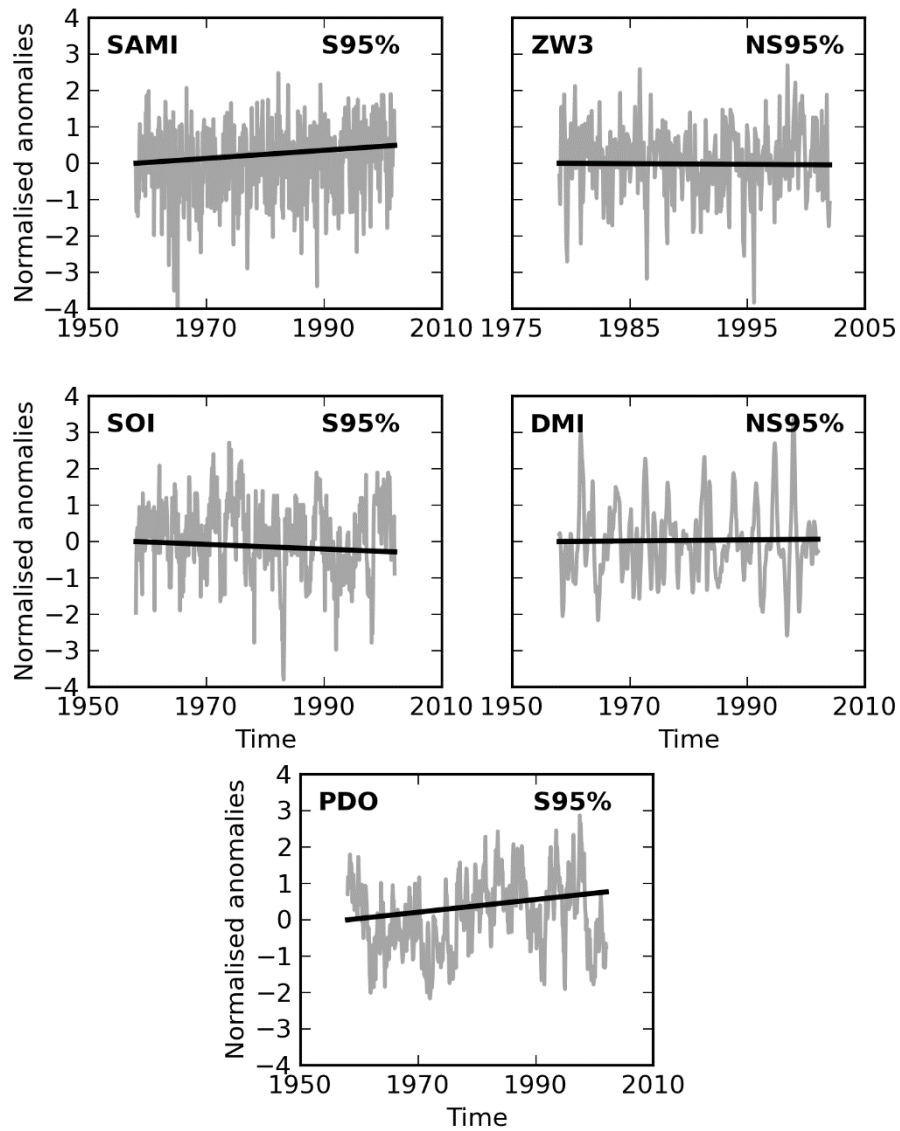


Figure 4.6. Monotonic trends in normalised anomalies of climate indices: Southern Annular Mode index (SAMI), Zonal Wavenumber-3 Pattern (ZW3) index, Southern Oscillation Index (SOI), Dipole mode Index (DMI), and Pacific Decadal Oscillation (PDO) index. The anomalies of climate indices were normalised by the standard deviation. Trends were computed for the period 1979–2001 for the ZW3 index, and for the period 1958–2001 for the other indices. **S95%** and **NS95%** stand for statistically significant and non-significant at the 95% confidence level, respectively.

4.4 Association between climate patterns and storm wave clustering

Monthly and lagged-seasonal correlations between storm cluster indices and climate indices are presented in Figures 4.7 and 4.8. Seasonal correlations did not provide significant additional information in relation to the monthly and

lagged-seasonal ones, and therefore their results are not shown. Statistically significant correlations were found at many sites along the 200 m isobath around New Zealand, albeit clustered storms were generally weakly correlated ($|R| < 0.42$) with climate indices.

With respect to monthly correlations (Figure 4.7), fewer clustered storms occurred on the west coast in association with positive SAM. The strengthening of the circumpolar westerlies is characteristic of a positive SAM (Marshall, 2003; Gupta and England, 2007), and so one would expect the opposite response in the number of clustered storms. Nevertheless, a poleward shift of extratropical cyclone storm tracks has been observed (Gillett and Thompson, 2003), accompanying the trend toward the positive phase of the SAM since the mid-1960s (Marshall, 2003). This shift results in decreases in westerly waves in the regions immediately adjacent to the west coast (Hemer *et al.*, 2010) because of a southward displacement of wave generation zones (Godoi *et al.*, 2017). Consequently, the wave energy coming from the west is reduced on the west coast when the positive phase of the SAM is more pronounced. On the contrary, the number of clustered storms increased on the same coast during negative phases of the ZW3, due to the intensification of the eastward atmospheric zonal flow. The latter becomes more relevant in the lower latitudes of the study region, as demonstrated by strengthened correlations northward (Figure 4.7). The west coast was also affected by SWCs generated during opposite phases of the PDO (positive) and ENSO (negative - El Niño events). Likewise, clustering was more frequent during positive IOD and negative ENSO to the south of New Zealand. The IOD can take place through the ENSO conditions because of the teleconnecting nature of these two modes (Schott *et al.*, 2009; Izumo *et al.*, 2010; Taschetto *et al.*, 2011; Godoi *et al.*, 2016). The signature of this relationship was also observed along the north coast, with enhanced clustering during La Niña events (positive ENSO) and negative IOD. Clustered storms occurred more frequently on the east coast of the North Island during positive phases of the SAM and ZW3, and on the east coast of the South Island during negative ENSO and positive PDO. During positive SAM, the refraction of westerly swells seems to make waves arrive on the east coast of the North Island with more intensity than

on the same coast of the South Island (Godoi *et al.*, 2016, 2017). In a similar fashion, the waves produced by the northward wind stress anomaly to the south of New Zealand related to positive ZW3 (Cai *et al.*, 1999) have a more marked effect on the North Island than on the South Island. Conversely, the larger southwesterly waves generated to the south of New Zealand during negative ENSO and positive PDO (Godoi *et al.*, 2016) have a stronger influence on the east coast of the South Island. Given that the main signatures of the ENSO, IOD, and PDO are observed far away from New Zealand, their associated conditions modify the atmosphere and ocean around the country through teleconnections. Tropic-extratropic teleconnections occur through disturbances in the Hadley cell (Liu and Alexander, 2007). The latter modifies the subtropical atmospheric circulation by changing the moisture and heat sources responsible for dispersion of the Rossby waves that influence the extratropics (Grimm and Ambrizzi, 2009). As Rossby waves are dispersed, cyclone and anti-cyclone winds strengthen. Anomalously strong winds generate larger waves, resulting in more frequent storm waves. As the time between consecutive storms shortens, in this case, more clustered storms are observed.

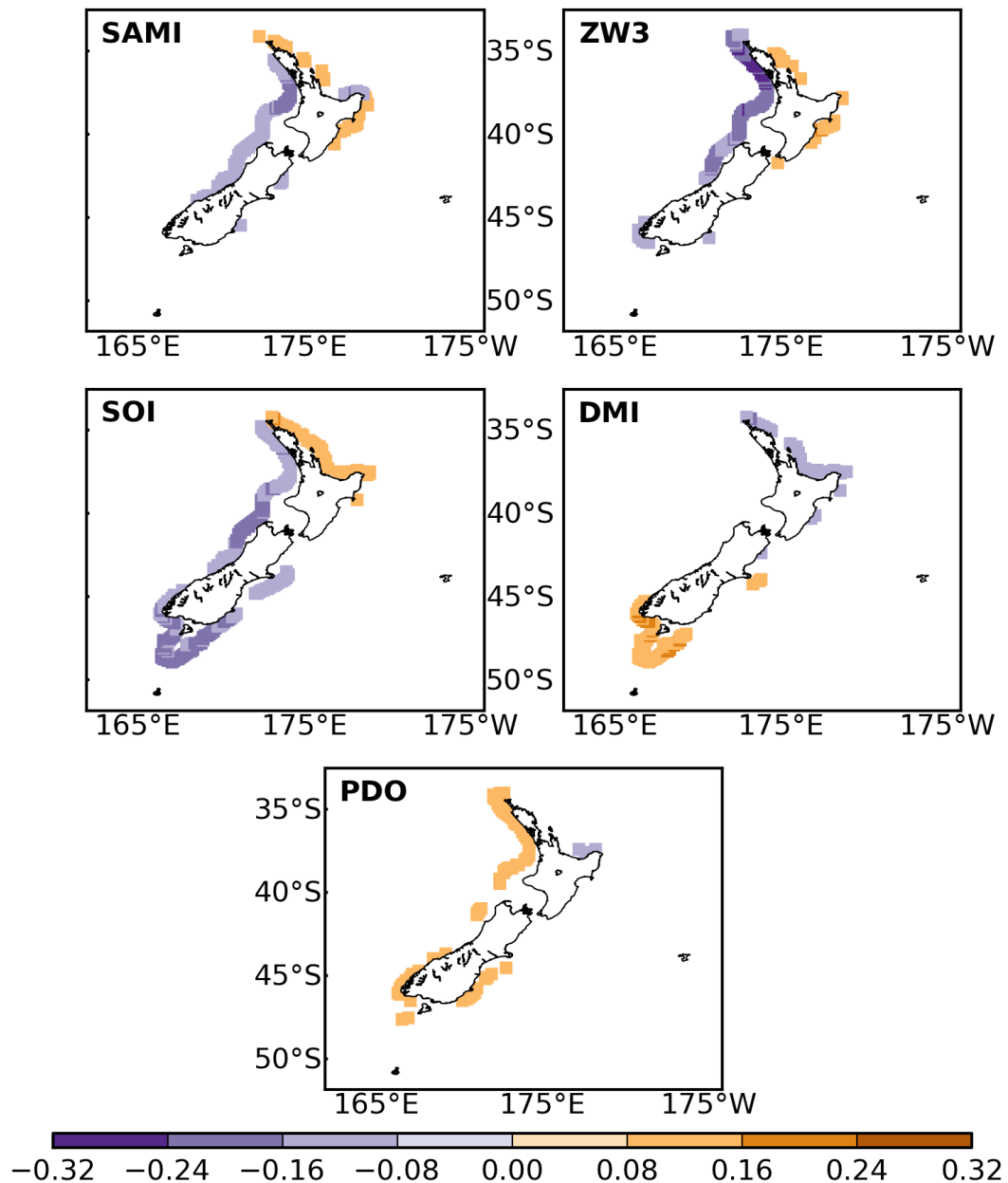


Figure 4.7. Correlations of monthly anomalies between storm cluster indices and climate indices. Correlations were carried out at the model grid points on the 200 m isobath over the period 1958–2001 for the SAMI, SOI, DMI, and PDO index, and over the period 1979–2001 for the ZW3 index. Only statistically significant values at the 95% confidence level are displayed.

The first signature of the ENSO is generally observed in the eastern equatorial Pacific (Bjerknes, 1966; Wyrтки, 1975; Trenberth and Hoar, 1996), and therefore, the ENSO-related changes in the atmosphere and ocean around New Zealand are delayed. Because of the inherent noisiness of the SOI time series at

short timescales, seasonally-averaged SOI values have been found to be more suitable for correlations than monthly-averaged values (Harley *et al.*, 2010). Hence, lagged-seasonal correlations are likely to be better for assessing variations in storm wave clustering around New Zealand related to the ENSO fluctuations. The same is true for the IOD and PDO conditions, which are also strongly influenced by the ENSO variability (Schott *et al.*, 2009; Mantua *et al.*, 1997). Although New Zealand is situated in the latitude band where the largest variabilities related to the SAM and ZW3 are experienced (the high and mid-latitudes of the Southern Hemisphere), lagged-seasonal correlations were also performed for these oscillations. Thus, climate patterns of a given season were correlated with clustered storms of the next season. Correlations with the SOI strengthened substantially along all coasts (Figure 4.8). A similar pattern was observed for the DMI to the south of New Zealand, along the southwestern coast, and in part of the north coast, and for the PDO index at most sites where statistically significant monthly positive correlations had been obtained. This enhancement relative to non-lagged correlation is due to the time that teleconnected phenomena take to respond to the warming and cooling of the Indian and Pacific Oceans' tropical waters. An example of this delayed response is the warming in the tropical Indian Ocean caused by the ENSO-related fluctuations, which takes approximately 3–6 months to occur (Deser *et al.*, 2010). As opposed to the results for the SOI, DMI, and PDO index, lagged-seasonal correlations between clustered storms and SAMI/ZW3 index either weakened or lost statistical significance at most sites where significant monthly correlations had been obtained, with the exception of the positive correlations with the SAMI found now to the south of New Zealand (Figure 4.8). These results demonstrate that the SWCs that hit New Zealand are more synchronised with the SAM and ZW3 fluctuations than with those of the ENSO, IOD, and PDO. Seasonal correlations (not shown) showed slightly higher absolute values (up to $|R| = 0.42$) than the monthly and lagged-seasonal ones for the SAMI, on the west coast, and for the ZW3 index, at a few sites on the north and east coasts.

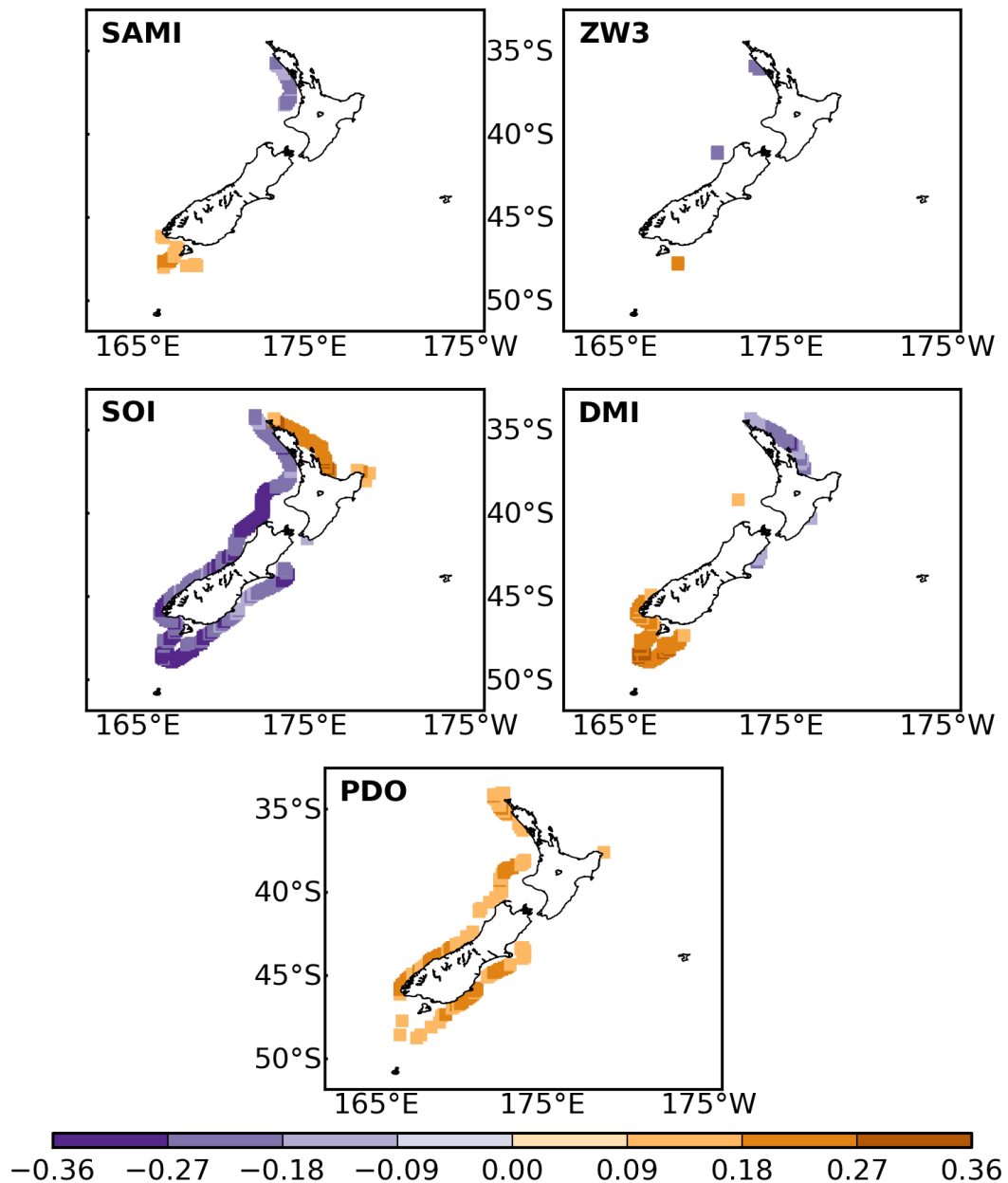


Figure 4.8. Correlations of seasonally-averaged monthly anomalies between storm cluster indices and climate indices lagged by one season. Correlations were carried out at the model grid points on the 200 m isobath over the period 1958–2001 for the SAMI, SOI, DMI, and PDO index, and over the period 1979–2001 for the ZW3 index. Only statistically significant values at the 95% confidence level are displayed.

SWC parameters had a stronger connection with the ENSO and PDO than the other oscillations (Figures 4.9, 4.10, and 4.11). Although the north coast is generally impacted by relatively low-energy SWCs (Figure 4.4), their CSE was highly correlated (R up to 0.64) with La Niña episodes (Figure 4.9). During such episodes,

stronger northeasterly winds are produced to the north of New Zealand (Gorman *et al.*, 2003b), leading to larger waves on the north coast (Gorman *et al.*, 2003b; Godoi *et al.*, 2016). La Niña-like effects also occur during negative PDO because of its inverse relationship with the ENSO (Godoi *et al.*, 2016), and this resulted in more energetic SWCs along part of the north coast (Figure 4.9). Not surprisingly, El Niño-like effects are experienced during positive PDO (Mantua *et al.*, 1997) on the west, south, and east coasts, and entail increased southwesterly winds (Gordon, 1986) and correspondingly larger waves (Laing, 2000). This explains the strong correlations of CSE with the SOI and PDO index along those coasts (Figure 4.9). SWCs were also more energetic on the west coast of the North Island during negative phases of the SAM and ZW3, and to the south of New Zealand during positive phases of the SAM and IOD (Figure 4.9). SWCs tended to last longer along most of the west, south, and east coasts during positive PDO and negative ENSO, while their duration increased on the north coast during La Niña and La Niña-like (negative IOD) events (Figure 4.10). Positive phases of the SAM and IOD (stronger westerly and southwesterly winds, respectively) occurred when there were longer-lasting SWCs to the south of New Zealand. A larger number of storms within the cluster coincided with El Niño episodes and positive PDO along the west and east coasts, and with La Niña events and negative IOD on the north coast (Figure 4.11). The number of storms was also larger on the west coast during negative SAM and in the presence of a more intense zonal flow during negative ZW3, while in southern New Zealand the number of storms increased during El Niño conditions and positive phases of the SAM and IOD. These annual correlations (Figures 4.9, 4.10, and 4.11) support the assumption that trends in SWC parameters (Figure 4.5) are associated with trends in climate oscillations (Figure 4.6). More frequent El Niño-like conditions, during either negative ENSO or positive PDO phases, were consistent with increases in SWC parameters on the south, east, and west coasts of the South Island. Furthermore, strengthened circumpolar westerlies associated with the trend for a positive SAM (Marshall, 2003) were compatible with trends in SWC parameters to the south of New Zealand.

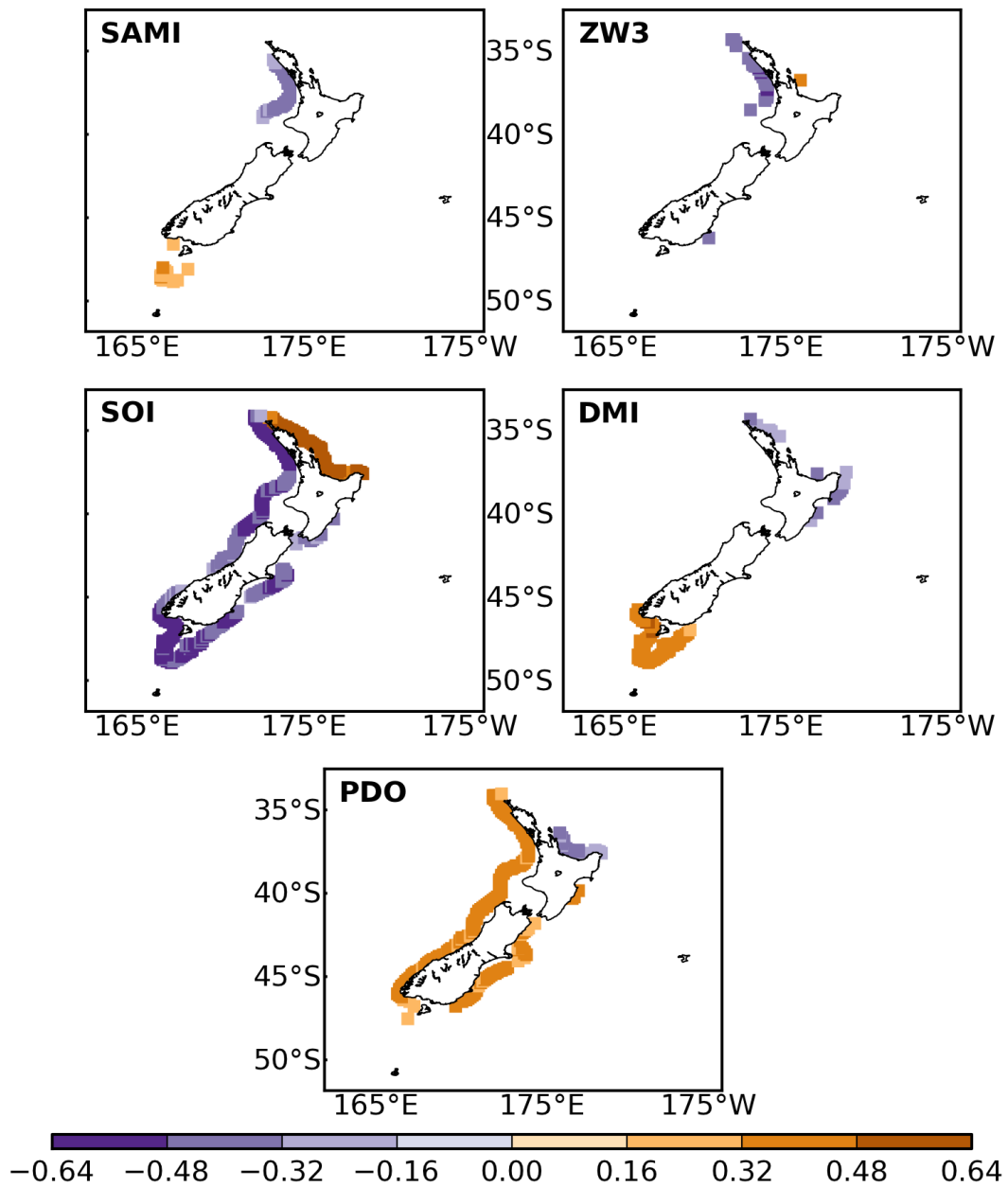


Figure 4.9. Correlations of annually-averaged monthly anomalies between cumulative storm energy per cluster and climate indices. Correlations were carried out at the model grid points on the 200 m isobath over the period 1958–2001 for the SAMI, SOI, DMI, and PDO index, and over the period 1979–2001 for the ZW3 index. Only statistically significant values at the 95% confidence level are displayed.

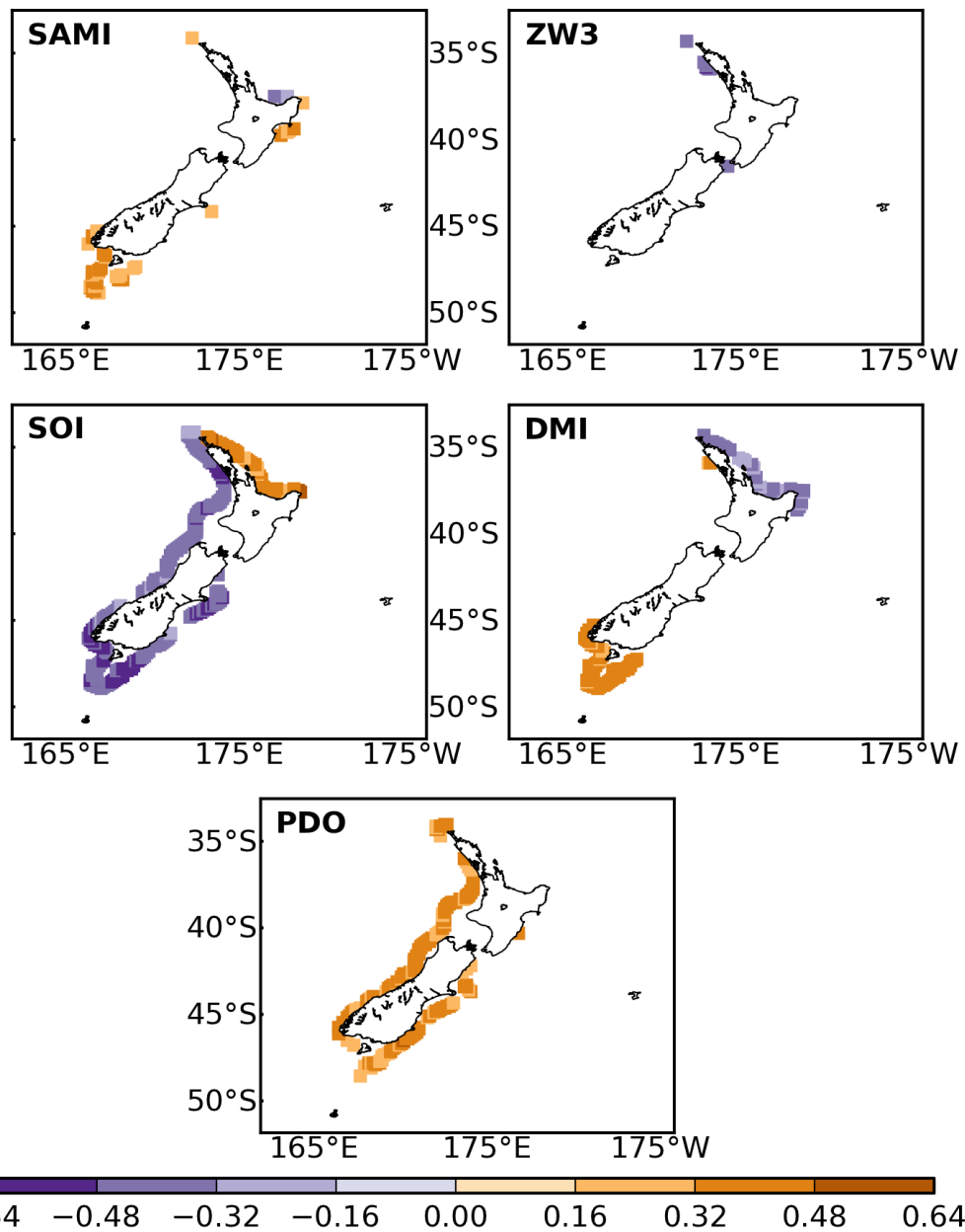


Figure 4.10. Correlations of annually-averaged monthly anomalies between storm cluster duration and climate indices. Correlations were carried out at the model grid points on the 200 m isobath over the period 1958–2001 for the SAMI, SOI, DMI, and PDO index, and over the period 1979–2001 for the ZW3 index. Only statistically significant values at the 95% confidence level are displayed.

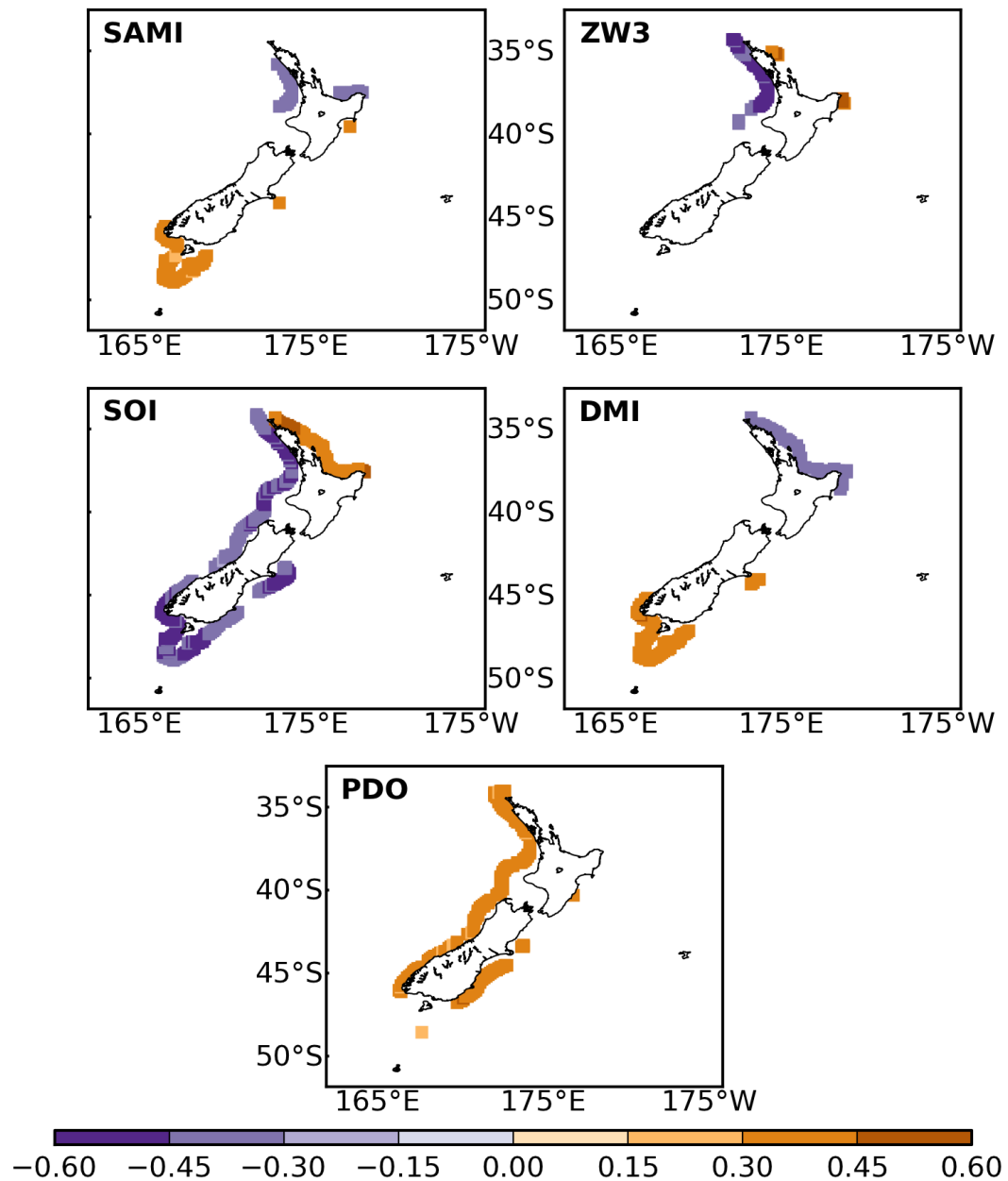


Figure 4.11. Correlations of annually-averaged monthly anomalies between the number of storms within the cluster and climate indices. Correlations were carried out at the model grid points on the 200 m isobath over the period 1958–2001 for the SAMI, SOI, DMI, and PDO index, and over the period 1979–2001 for the ZW3 index. Only statistically significant values at the 95% confidence level are displayed.

Figure 4.12 is an example of the wavelet spectral analysis results obtained for the four model grid points (Figure 4.1) selected as representative of the major coastline orientations, north (N), west (W), east (E), and south (S). It illustrates the correlations of monthly anomalies between storm cluster indices and the SOI at

several timescales, and highlights the periods in which the ENSO conditions were presumably related to the number of clustered storms around New Zealand. The most relevant signals were generally observed at 2–7 year timescales. On the north coast, increased northeasterly winds, typical of La Niña events, were responsible for a more frequent clustering from the late 1960s to the late 1980s (Figure 4.12, top panel). Clustered storms were most correlated with positive SOI during the early and mid-1970s, coinciding with the 1974–1976 La Niña (Jury *et al.*, 2002). Curiously, the extreme 1998–1999 La Niña (Cai *et al.*, 2015) did not seem to have had any relation to storm wave clustering on the north coast, as opposed to the extreme La Niña of 1988–1989 (Cai *et al.*, 2015) (upward arrows, 4-year cycle). Increases in clustered storms due to stronger southwesterly winds during El Niño events were more pronounced on the west coast, with strongest correlations in the early 1980s (Figure 4.12, left panel). An extreme El Niño indeed occurred in 1982–1983 (Wang and Cai, 2013; Cai *et al.*, 2014). The long horizontal band of strong correlations during almost the whole period of analysis (Figure 4.12, left panel) also comprises two other extreme El Niño events, occurred in 1972–1973 (Saji *et al.*, 1999) and 1997–1998 (Wang and Cai, 2013; Cai *et al.*, 2014), as well as the consecutive 1986–1987 and 1987–1988 El Niño episodes (Cai *et al.*, 2015), and the 1991–1992 El Niño, which was only short and ended abruptly (Hayward, 1993). A 2-year cycle associated with the early 1960s El Niño (McPhaden *et al.*, 2015) showed a strong correlation with clustered storms to the south of New Zealand (Figure 4.12, bottom panel). El Niño was also related to clustering on the east coast from the early 1960s to the early 1980s (Figure 4.12, right panel - signals mostly confined between 2- and 4-year cycles), although such relationship was not as strong as on the other coasts.

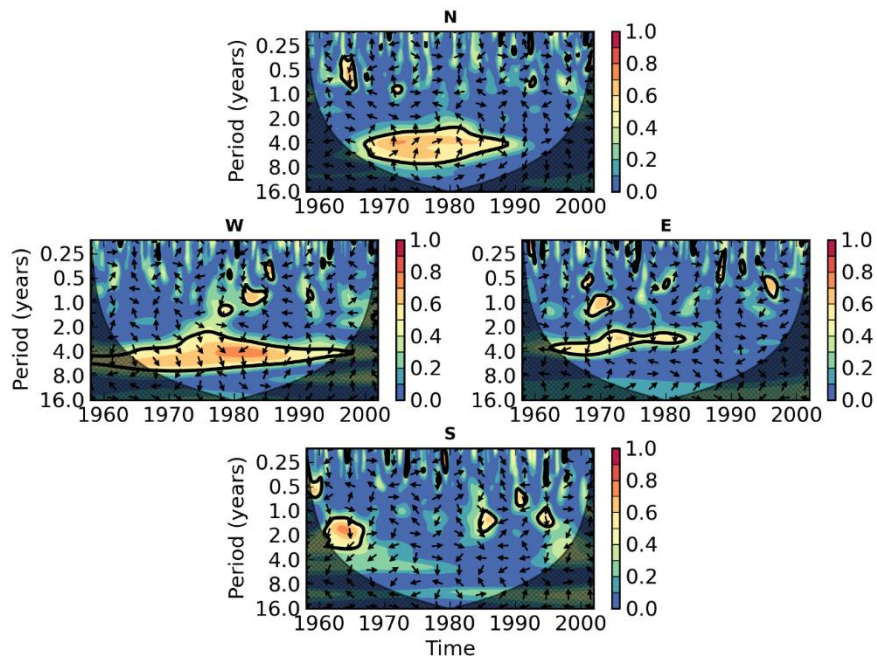


Figure 4.12. Squared wavelet coherence spectra of monthly anomalies of storm cluster indices with monthly anomalies of the SOI. Thick contours represent 90% confidence levels, while hatched areas represent the cone-of-influence. In phase and anti-phase signals are represented by arrows pointing upward and downward, respectively. Arrows pointing rightward represent the ENSO preceding storm wave clusters, whereas the converse is true for arrows pointing leftward. The letters N, W, E, and S on top of each plot stand for north, west, east, and south coasts, respectively.

Spectral analyses for the SAM, ZW3, PDO, and IOD were also performed (not shown), and their most noteworthy results are described as follows. The most striking feature of the coherence spectra obtained for the SAM appeared at timescales between 6 and 16 years, and resulted in a higher occurrence of clustered storms to the south of New Zealand during its positive phase. A large part of this signal is within the cone-of-influence, a region of the spectrum where edge effects become important (Torrence and Compo, 1998), requiring caution in the interpretation of the results. Despite that, considerably high statistically significant correlations (up to 0.9) were found at those timescales during the whole period of analysis, with the strongest signals appearing first in the early 1990s. This strengthening in the correlation on the south coast throughout the time seems to accompany the trend for a positive SAM. On the west coast, a prolonged negative

SAM (Gordon *et al.*, 2007) was strongly correlated (up to 0.8) with increases in clustered storms from the late 1960s to the early 1970s, supporting the negative monthly and seasonal linear correlations discussed previously. Similarly to the spectra for the SAM, the coherence spectra of the ZW3 index with storm cluster indices showed strong correlations (up to 0.8) in the south at timescales longer than 6 years. These correlations appeared in approximately 1987, indicating that increases in clustered storms coincided with positive anomalies in the northward atmospheric flow. Again, although within the cone-of-influence, such correlations were statistically significant. The migration from a more zonal to a more meridional atmospheric flow (a transition to the ZW3 positive phase) in 1997 (Raphael, 2004) was highly correlated (correlation > 0.9) with a brief decrease in clustering on the west coast. The opposite atmospheric change (from meridional to zonal flow) in 1986/1987 (Raphael, 2004) led to more clustered storms on the same coast. A 2-year PDO cycle was associated with a strange and counter-intuitive clustering (fewer clustered storms - correlation > 0.6) to the south of New Zealand throughout the 1980s, when the PDO was predominantly positive (Mantua *et al.*, 1997). On the east coast, the same happened for the PDO decadal variability from the late 1980s to the early 2000s (signal within the cone-of-influence), whilst cycles ranging from 2 to 8 years were related to more clustering from the late 1950s to the early 1970s (correlation > 0.7 - signal partially within the cone-of-influence). Positive IOD was strongly correlated (correlation up to 0.9) with clustering on the west coast from the mid-1970s to the early 2000s. Since the mid-1980s, clustering on the west coast under El Niño-like conditions seemed more associated with positive IOD than negative ENSO. Two extreme positive IOD events occurred in 1994 and 1997 (Saji *et al.*, 1999), and were related to more clustered storms on the west coast owing to the intensification of southwesterly winds. From the early 1980s to the early 1990s, decreases in clustering on the north coast occurred during positive IOD, whereas stronger northeasterly winds (La Niña-like conditions associated with negative IOD) induced more clustered storms. A short-lived statistically significant signal was identified in the coherence spectrum between the storm cluster index to the north of New Zealand and DMI during the extreme 1998–

1999 La Niña. This signal suggests that negative IOD was associated with fewer clustered storms in the region during that period, which could explain the lack of association between clustering and the extreme 1998–1999 La Niña, as previously noted. However, this contradicts the expected behaviour of clustered storms during negative IOD and, therefore, the issue remains open.

4.5 Conclusions

Work on coastal erosion has shown that storms are more hazardous when occurring in clusters because the coastline has insufficient time to recover between storms (Lee *et al.*, 1998; Ferreira, 2005). The reserves of sand in the beachface deplete during the first storm, facilitating erosion during subsequent ones. Here, SWCs and their characteristics in New Zealand waters were explored using results of a 45-year (1957–2002) wave hindcast. Cluster duration, the number of storms within the cluster, and the potential for cluster-induced coastal erosion were analysed through long-term averages and trends. The responses of clustered storms to near and remote atmospheric variability were also addressed, by computing correlation coefficients and applying the wavelet spectral analysis.

Storm waves tended to cluster more to the northeast of New Zealand and on the central eastern coast of the South Island. Recurrent southwesterly swells, generated by extratropical cyclones, produced energetic environments to the south of New Zealand and on the northwestern coast, making these regions the most vulnerable to coastal erosion caused by SWCs. SWCs lasted longest on a segment of the east coast of the South Island sheltered from the prevailing southwesterly swell, where they were also least frequent. Trends calculated for the period 1958–2001 showed that SWCs have incorporated more storms, have become more hazardous, and have lasted longer, principally around the South Island. Although these trends may be affected by the ERA-40 data assimilation temporal inhomogeneity, it is encouraging that they agree with trends in the SAM, PDO, and ENSO.

Teleconnection patterns showed strong links with storm wave clustering around New Zealand. These links arise in several forms, as for example, ENSO-

related effects are experienced in the area because of the pressure seesaw between the Indian and Pacific Oceans (Kousky *et al.*, 1984); the extratropical signature of the ENSO projects onto the SAM (L'Heureux and Thompson, 2006) in the wave generation zone of the primary swell that hits New Zealand; variations associated with the IOD are explained by Rossby wave trains, which propagate from the tropical Indian Ocean and induce changes to the mid-latitude westerlies across southern Australia (Cai *et al.*, 2011). As a result of remote and local forcings, seasonal to decadal variabilities of climate patterns were found to be correlated with clustering around New Zealand, especially during strong phases of the modes. Stronger southwesterly winds during either El Niño events (negative ENSO) or conditions that resemble these, associated with positive phases of the IOD and PDO, caused increases in clustering primarily on the southwestern coast of New Zealand. The opposite phases of these oscillations, especially positive ENSO and negative IOD, affected the north coast through the predominance of increased northeasterly winds. Clustered storms were less synchronised with the ENSO, IOD, and PDO, whose main signatures take place far away from New Zealand, than with the SAM and ZW3 modes, which in turn show their main signatures in the water bodies surrounding the country. The strong eastward atmospheric zonal flow related to negative ZW3 led to a higher occurrence of clustered storms on the west coast, while enhanced westerlies associated with positive SAM had a significant impact on clustering to the south of New Zealand.

As an emerging topic, the spatial and temporal variabilities of storm wave clustering still need further research along most coasts around the world. Due to the strong influence of SWCs on erosion processes, sediment transport, and coastal flooding, a broad understanding of the dynamics of SWCs should underpin coastal management. Moreover, as undoubtedly dangerous systems, SWCs have a direct impact on safety and, consequently, on the economy. It is still not clear how storm wave clustering changes with the seasons and with anomalies associated with concurrent phases of two or more atmospheric oscillations. Future work should also assess relationships between SWCs and climate patterns considering a range of lag periods (only 1-season lag was analysed here). Additionally, our study

focused on the potential effect of clustering on erosion, but has not addressed how this translates into the scale of erosion on a particular beach. The study of the latter necessitates a much wider range of local observations to provide a similarly generalizable outcome. Nevertheless, the results presented here should assist in the prediction of impacts of future climate change in addition to supporting sea-related activities and providing a background for climatological studies.

Contributions of the author and co-authors to Chapter 5

I was responsible for the data processing, data analysis, and writing. Felipe M. de Andrade and I came up with the idea of the topic addressed in this chapter.

Richard M. Gorman produced and validated the hindcast results employed in Chapter 5.

Felipe M. de Andrade suggested the use of a compositing approach to achieve the objective of Chapter 5, and prepared the phases of the climate indices used in the calculation of composites.

Felipe M. de Andrade, Karin R. Bryan, and Richard M. Gorman reviewed the chapter and made suggestions regarding the writing.

CHAPTER 5: Response of the wave climate around New Zealand to wind conditions associated with ENSO-MJO combined activity

5.1 Introduction

Understanding the processes that force variations to the ocean surface gravity wave (henceforth wave) climate is essential for a range of applications, such as wave energy estimation and extraction, planning of naval and marine operations (Cox and Swail, 2001), and coastal hazard risk management. Many studies have shown that wave climate variability is connected with climate pattern fluctuations worldwide (e.g., Woolf *et al.*, 2002; Hemer *et al.*, 2010; Izaguirre *et al.*, 2011; Barnard *et al.*, 2015; Marshall *et al.*, 2015). Such connections are generally assessed by considering correlations with individual atmospheric oscillation modes (as, for instance, in Harley *et al.*, 2010; Stopa *et al.*, 2013; Godoi *et al.*, 2016), although waves might respond very differently when active phases of two or more modes co-occur (Kumar *et al.*, 2016). For example, wave parameters have been shown to relate to the El Niño–Southern Oscillation (ENSO) in many studies (e.g., Gorman *et al.*, 2003b; Hemer *et al.*, 2007; Harley *et al.*, 2010; Fan *et al.*, 2012; Shimura *et al.*, 2013; Stopa *et al.*, 2013; Stopa and Cheung, 2014; Reguero *et al.*, 2015; Godoi *et al.*, 2016; Kumar *et al.* 2016; Mortlock and Goodwin, 2016), while only a few have evaluated their links to the Madden-Julian Oscillation (MJO) (e.g., Stopa *et al.*, 2013; Marshall *et al.*, 2015).

The ENSO (Walker and Bliss, 1932, 1937; Bjerknes, 1961, 1966; Wyrтки, 1975; Neelin *et al.*, 1998) is the dominant mode of inter-annual variability in the ocean-atmosphere coupled system (Ashok *et al.*, 2007). It is well-known for its association with global impacts (Collins *et al.*, 2010) on, for example, rainfall (Ropelewski and Halpert, 1987), air temperature (Trenberth *et al.*, 2002), and waves (Stopa *et al.*, 2013). The ENSO features most prominently in the equatorial waters of the central and eastern Pacific Ocean at timescales ranging principally from 2 to 7 years

(Trenberth and Hurrell, 1994; Cane, 2005; McPhaden *et al.*, 2006a). The ENSO is composed of two active phases, La Niña (cold) and El Niño (warm), determined by sea surface temperature (SST) anomalies in the central and eastern Pacific Ocean (Chase *et al.*, 2006). These anomalies lead to enhanced [reduced] atmospheric convection over the central and eastern Pacific Ocean during El Niño [La Niña] episodes (Trenberth, 1997). Concurrent decreases [increases] in atmospheric convection occur over Indonesia and the western tropical Pacific owing to changes in momentum, heat, and moisture fluxes associated with the Walker circulation (Dai and Wigley, 2000). In the tropics, the ENSO-related atmospheric circulation effects are manifested through the dispersion of baroclinic equatorial waves (Lin *et al.*, 2007), whereas in the extratropics, they take place through the propagation of barotropic teleconnections (Horel and Wallace, 1981; Mo and Paegle, 2001).

The MJO (Madden and Julian, 1971, 1972, 1994) is the dominant mode of atmospheric sub-seasonal variability (10–90 days) (Mo and Nogues-Paegle, 2005), whose main signature occurs along the tropical latitude band. It is characterised by an eastward-propagating oscillation that primarily induces changes in the tropical atmospheric convection (Matthews, 2000; Matthews *et al.*, 2004; Wheeler and Hendon, 2004; Zhang, 2005; Roundy and Kravitz, 2009; Seo and Son, 2012). The MJO phases have been defined according to their associated enhanced convection locations. Specifically, the MJO-related atmospheric convection is observed over the Indian Ocean during phases 2 and 3, over the Maritime Continent during phases 4 and 5, over the western Pacific Ocean during phases 6 and 7, and in the Western Hemisphere and over Africa during phases 8 and 1 (Wheeler and Hendon, 2004). As the MJO propagates, convectively coupled equatorial atmospheric waves, such as Kelvin and Rossby waves (Matthews, 2000; Seo and Son, 2012), are dispersed and barotropic Rossby waves are generated (Seo and Son, 2012). The latter influence remote regions of the globe (Mo and Paegle, 2001; Mori and Watanabe, 2008). Both the MJO and ENSO have been recognised by their teleconnecting nature (Alexander *et al.*, 2002; Grimm, 2003; Matthews *et al.*, 2004; McPhaden *et al.*, 2006a; Grimm and Ambrizzi, 2009; Roundy *et al.*, 2010; Moon *et*

al., 2011; Seo and Son, 2012), meaning that their associated effects are experienced beyond their main regions of occurrence.

The interactions between the MJO and ENSO have been of increasing interest over the last decade. The ocean-atmosphere conditions associated with combined activity in the MJO and ENSO have been found to modulate, for instance, wind patterns (Hendon *et al.*, 2007; Roundy and Kravitz, 2009), atmospheric tropical convection (Roundy *et al.*, 2010), tropical cyclone activity (Klotzbach, 2012; Girishkumar *et al.*, 2015), rainfall (Shimizu and Ambrizzi, 2016), air temperature (Shimizu and Ambrizzi, 2016), oceanic Kelvin waves (Seiki *et al.*, 2009), and sea water temperature (McPhaden *et al.*, 2006b). To the knowledge of the authors, the wave climate variability associated with simultaneous fluctuations of these two oscillations has not yet been investigated, so providing motivation for the present study.

The wave climate around New Zealand is particularly interesting because the country lies at the interface of the Southern Ocean with the Tasman Sea and the Pacific Ocean and, therefore, the waves that affect the country are strongly influenced by the different ocean-atmosphere conditions prevailing in its surrounding water bodies. The long distance from other landmasses allows long-period swells, from all directions, to impact on the New Zealand coastline, especially those generated by mid-latitude storms propagating over the Southern Ocean. The Southern Ocean comprises the most active wave-generating zones in the world (Young, 1999; Chen *et al.*, 2002). Both wind-sea and swell waves that propagate into New Zealand waters have been found to be related to dominant climate oscillations (Godoi *et al.*, 2016). Using results of a long-term wave hindcast, carried out specifically for the New Zealand region, we investigate here how wind anomalies associated with the joint occurrence of the MJO and ENSO influence the wave variability in this unique environment.

Changes in wave conditions around New Zealand were examined by creating significant wave height (H_s) and wind anomalies composites according to simultaneous ENSO-MJO phase pairs. The latter were identified using climate indices representative of the ENSO and MJO states. The next section briefly

describes the datasets used and explains how composites were created. The H_s anomalies associated with combined activity in the ENSO and MJO are discussed in section 3. Finally, the conclusions are presented in section 4.

5.2 Datasets and methodology

Significant wave height fields were obtained from a 45-year (1957–2002) wave hindcast (hereafter 45WH) carried out using version 3.14 (Tolman, 2009) of the WAVEWATCH III model (Tolman, 1991). The 45WH (Gorman *et al.*, 2010) was conducted by one-way nesting a regional grid domain within a global grid. Wind and ice fields from the ERA-40 reanalysis (Uppala *et al.*, 2005) forced the wave simulation, which in turn generated 3-hourly and hourly wave parameters with spatial resolutions of $1.125^\circ \times 1.125^\circ$ (global grid) and $0.125^\circ \times 0.09375^\circ$ (approximately 10 km - regional grid), respectively. These wave parameters have been validated against satellite altimetry data, obtained from the TOPEX/Poseidon, ERS1, and ERS2 missions, and against buoy measurements, sourced from the National Data Buoy Center (NDBC) and local buoys. The 45WH results have been used to assess the mean (Godoi *et al.*, 2016) and extreme (Godoi *et al.*, 2017) wave climates as well as storm wave clustering conditions around New Zealand (Godoi *et al.*, in press). Additional details on the 45WH and its validation can be found in Gorman *et al.* (2010) and Godoi *et al.* (2016, 2017).

The MJO activity was quantified by the real-time multivariate (RMM) daily index (Wheeler and Hendon, 2004), obtained from the Australian Bureau of Meteorology (BoM). The index results from the two leading empirical orthogonal functions (EOFs) of the combined spatially-averaged (15°S – 15°N) normalised fields of zonal wind at 850 hPa, zonal wind at 200 hPa, and outgoing longwave radiation. The principal components associated with the two leading EOFs determine the daily amplitude and phase of the RMM index. In order to select events with potential impacts on the ocean, active MJO days were defined by RMM index amplitudes greater than 1.5 standard deviations, following Marshall *et al.* (2015).

The ENSO activity was measured by the Oceanic Niño Index (ONI), sourced from the National Oceanic and Atmospheric Administration (NOAA). ONI values

represent 3-month running means of SST anomalies in the Niño 3.4 region (5°N–5°S, 120°W–170°W). El Niño (La Niña) episodes are recognised when ONI values remain above (below) 0.5°C (-0.5°C) for at least five consecutive overlapping seasons. These values were converted into daily values, to match the temporal resolution of the RMM index, by assigning the 3-month running mean value of a given month to all days of that month.

Finally, composites were created for the 23-year period 1979–2002 using daily anomalies of both the hourly H_s fields extracted from the 45WH regional domain and the 6-hourly wind fields at 10 m used to force the 45WH global grid. The Atlantic Ocean and any other seas within the area bordered by the east coast of the Americas and the west coast of Africa were excluded from the wind anomaly composites, given that our focus is on the waves that can potentially affect the New Zealand coastline. As in Roundy *et al.* (2010), only the months in which both climate patterns (ENSO and MJO) are potentially most active (November–March) were used when creating the composites, although the inactive phases of the modes (ENSO and MJO neutral phases) were also analysed. Composites were established by averaging H_s and wind daily anomalies over all days of each simultaneous ENSO-MJO phase pair (Table 5.1). Statistical significance of composites was calculated using Student's t-test (Student, 1908; Wilks, 2006).

Table 5.1. Number of days in each ENSO-MJO phase pair over the November–March season during the period 1979–2002.

	El Niño	La Niña	ENSO neutral
MJO phase 1	47	33	66
MJO phase 2	36	53	82
MJO phase 3	67	69	101
MJO phase 4	51	34	74
MJO phase 5	31	37	65
MJO phase 6	32	54	84
MJO phase 7	33	46	123
MJO phase 8	50	22	63
MJO neutral	651	529	946

5.3 Results and Discussion

The mean wind pattern is substantially modified during simultaneous ENSO-MJO fluctuations (Figures 5.1, 5.2, and 5.3). The wind anomalies found along and near the Equator result from circulation anomalies in the Walker cell ascending and descending branches (Grimm and Ambrizzi, 2009). Anomalous heat sources affect winds not only locally, but also remotely through tropic-tropic and tropic-extratropic teleconnections (Grimm and Ambrizzi, 2009, Stan *et al.*, 2017). Meridional variations in the tropical circulation are evident in some phase pairs (e.g., El Niño-MJO phase 8 – Figure 5.1), suggesting corresponding variations in the Hadley cell. Disturbances in the Hadley cell modify the subtropical atmospheric circulation (Liu and Alexander, 2007) and, consequently, the Rossby wave sources responsible for the tropic-extratropic teleconnection genesis (Grimm and Ambrizzi, 2009; Shimizu and Cavalcanti, 2011). In some composites (e.g., El Niño with MJO phases 8 and 1 – Figure 5.1), tropic-extratropic teleconnection signals can be observed in the mid-latitudes of both hemispheres over the Pacific Ocean,

resembling the Pacific-South American (PSA) (Mo and Paegle, 2001) and Pacific-North American (PNA) (Barnston and Livezey, 1987; Mori and Watanabe, 2008) teleconnection patterns. Although relatively weak, wind anomalies are still widespread when the MJO is in its neutral phase (Figures 5.1 and 5.2, bottom right panels), and have opposite patterns during El Niño and La Niña events.

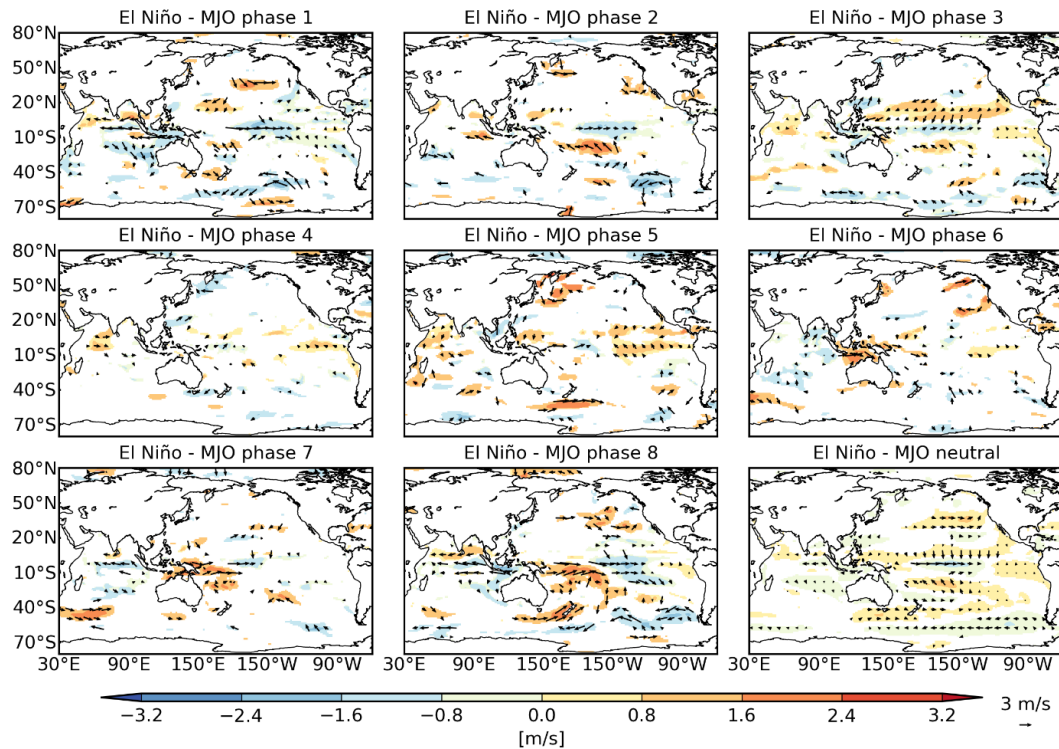


Figure 5.1. Wind at 10 m daily anomaly composites for El Niño with MJO phases over the November–March season during the period 1979–2002. Only statistically significant anomalies at the 95% confidence level are displayed. Statistical significance was calculated using Student’s t-test.

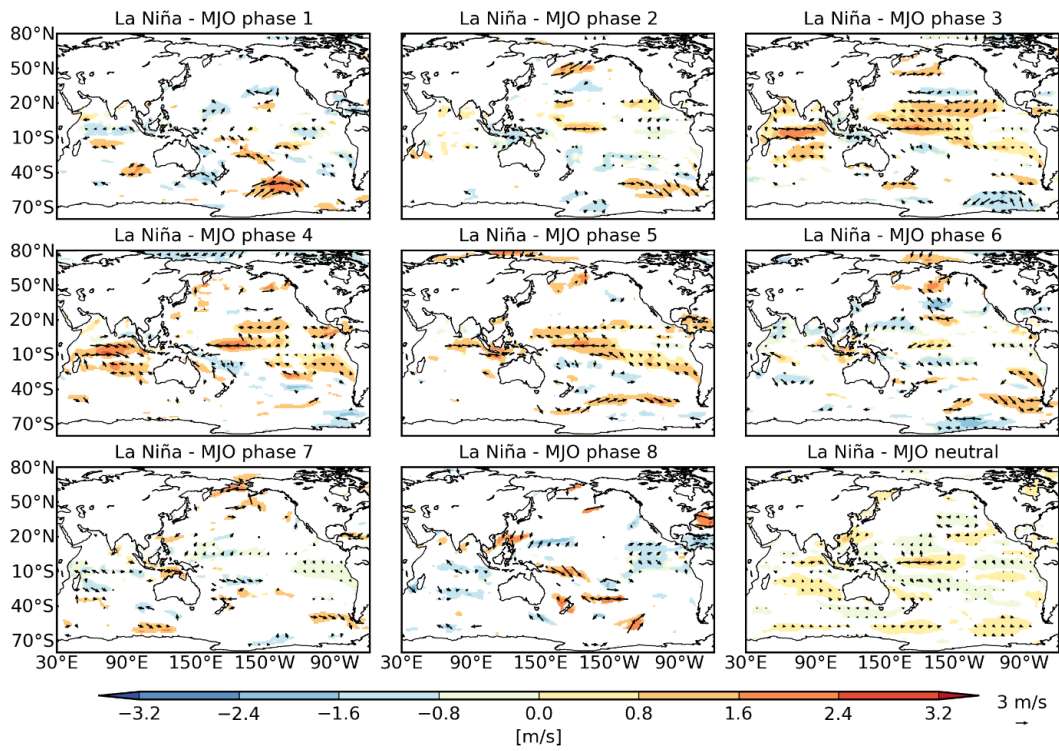


Figure 5.2. Wind at 10 m daily anomaly composites for La Niña with MJO phases over the November–March season during the period 1979–2002. Only statistically significant anomalies at the 95% confidence level are displayed. Statistical significance was calculated using Student’s t-test.

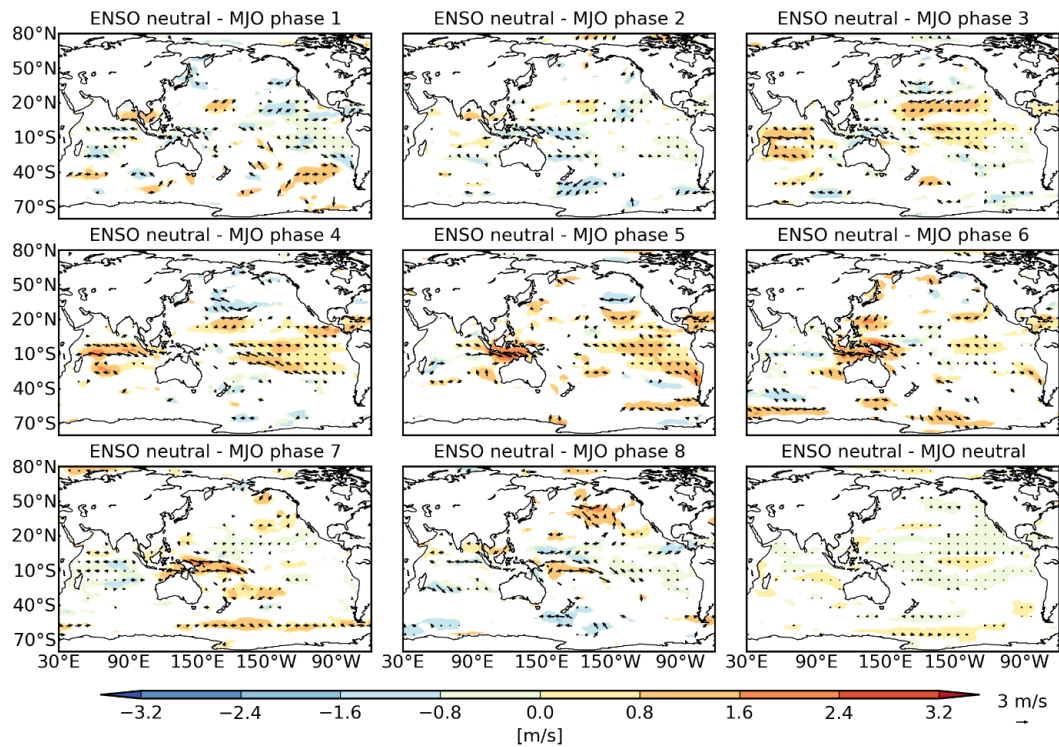


Figure 5.3. Wind at 10 m daily anomaly composites for ENSO neutral with MJO phases over the November–March season during the period 1979–2002. Only statistically significant anomalies at the 95% confidence level are displayed. Statistical significance was calculated using Student’s t-test.

5.3.1 Composites for active ENSO with MJO phases

Larger waves are normally observed along the west and south coasts of New Zealand during El Niño episodes (Laing, 2000; Gorman *et al.*, 2003b; Godoi *et al.*, 2016), which result from anomalously strong southwesterly winds in the vicinity of the country in response to negative atmospheric pressure anomalies (Gordon, 1986). These wind and wave conditions can also be observed when El Niño occurs with MJO phases 8 and neutral (Figures 5.1 and 5.4). Conversely, the positive anomalies in wind and H_s on the west and south coasts associated with El Niño are masked when the MJO is in phases 2, 3, 4, and 6 (Figure 5.4). Furthermore, negative anomalies in H_s appear along and off the east coast and are reinforced off the north coast during El Niño-MJO phase 3 (Figure 5.4) in comparison to when the MJO is inactive (El Niño-MJO neutral). During El Niño-MJO phase 4, the positive H_s anomalies expected during El Niño events even reverse signs off the west coast

and lose statistical significance elsewhere (Figure 5.4). This reflects the negative wind anomalies that show up in the southern Tasman Sea (Figure 5.1, El Niño-MJO phase 4). An anti-cyclone is generated over New Zealand during MJO phases 3 and 4 (Seo and Son, 2012), contributing to reducing the cyclonic circulation effects associated with El Niño (Gordon, 1986).

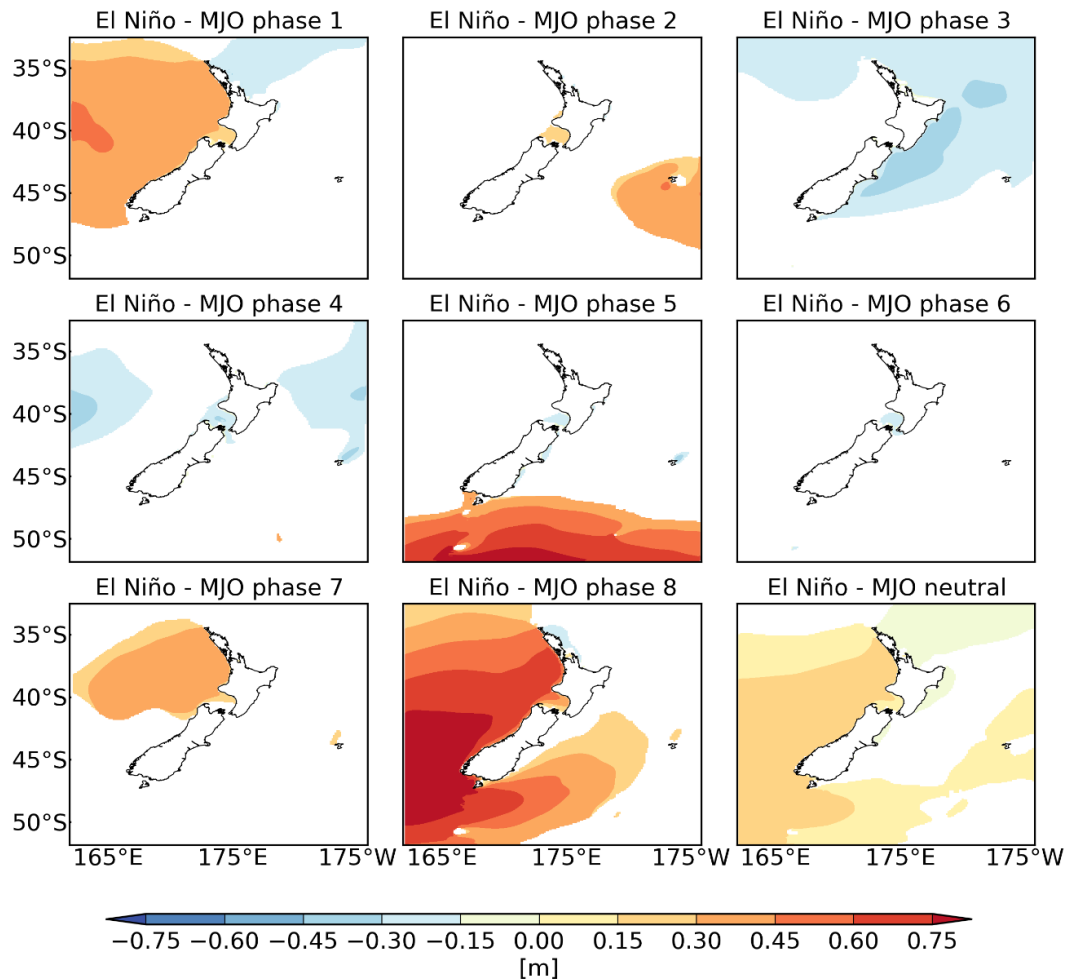


Figure 5.4. Significant wave height daily anomaly composites for El Niño with MJO phases over the November–March season during the period 1979–2002. Only statistically significant anomalies at the 95% confidence level are displayed. Statistical significance was calculated using Student’s t-test.

The most striking feature of the H_s anomaly composites, for the combinations of El Niño events with MJO phases (Figure 5.4), appears during El Niño-MJO phase 8. The whole west and south coasts are characterised by

substantially-increased wave heights, which are caused by an extensive band of stronger westerly and southwesterly winds to the south of Australia and around most parts of New Zealand (Figure 5.1). The largest anomalies in H_s , of more than 0.75 m, are observed along and off the southwestern coast (Figure 5.4, El Niño-MJO phase 8). Larger waves also occur in the waters off the east coast during the same phase pair. The initial stage of these wind and wave conditions seems to occur during the previous MJO phase (El Niño-MJO phase 7), when positive wind anomalies over a small area of the Tasman Sea (Figure 5.1) generate southwesterly waves that affect the west coast of the North Island (Figure 5.4). Disregarding magnitude, the spatial patterns of wind composites during MJO phases 8 and neutral combined with El Niño (Figure 5.1) are roughly similar, especially around New Zealand. The same is true for the spatial patterns of wave composites (Figure 5.4), indicating that El Niño-related atmospheric circulation effects are enhanced by the convective activity associated with the MJO phase 8 over the central equatorial Pacific. This mechanism explains the larger wind and wave anomalies around New Zealand during El Niño-MJO phase 8.

Higher-intensity winds are experienced in the Tasman Sea during El Niño-MJO phase 1 (Figure 5.1), resulting in positive anomalies in H_s along and off the west coast of New Zealand (Figure 5.4). This seems to be the dissipative stage of the preceding ENSO-MJO phase pair (El Niño-MJO phase 8), with positive H_s anomalies still remaining in the area despite their weakening. The west coast of New Zealand is, therefore, affected considerably by more energetic waves throughout the MJO propagation from the western Pacific Ocean (phase 7) to the Western Hemisphere (phase 8) and Africa (phase 1) when El Niño is active. Conversely, the southern coast receives the largest waves during El Niño-MJO phase 8 and El Niño-MJO phase 5. Positive anomalies in the eastward atmospheric flow to the south of the country are produced during El Niño-MJO phase 5 (Figure 5.1), when enhanced atmospheric convection develops over the Maritime Continent. This enhancement accompanies the eastward anti-cyclonic circulation displacement from the tropical western Pacific to the east of New Zealand (Seo and

Son, 2012), which contributes to intensifying the cyclonic circulation associated with El Niño to the south of the country.

Previous work (e.g., Gorman *et al.*, 2003b; Godoi *et al.*, 2016) has shown that the north coast of New Zealand usually receives larger waves during La Niña events, when stronger northeasterly winds dominate the region (Gorman *et al.*, 2003b). A similar wave pattern is noted in the absence of significant MJO activity, in addition to small decreases in H_s on the west and southwest coasts and their seaward areas (Figure 5.5, La Niña-MJO neutral). Positive wind anomalies to the north of New Zealand are relatively weak and mostly from the east during La Niña-MJO neutral (Figure 5.2). Although encompassing a smaller region, these wind anomalies strengthen and experience a gentle counter-clockwise rotation during La Niña-MJO phase 6, leading to stronger anomalies in H_s than during La Niña-MJO neutral (Figure 5.5). The strengthening in wind anomalies results from the atmospheric convective activity reinforcement over the western tropical Pacific, which is excited by both La Niña and MJO phase 6 (Shimizu and Ambrizzi, 2016). The wind anomalies associated with La Niña events combined with MJO phases 7, 8, and 1 cause weaker anomalies in H_s than La Niña-MJO phase 6 (Figure 5.5). In comparison to the latter, an additional patch of positive H_s anomalies is found off the west coast during La Niña-MJO phase 8 due to positive wind anomalies in the Tasman Sea (Figure 5.2).

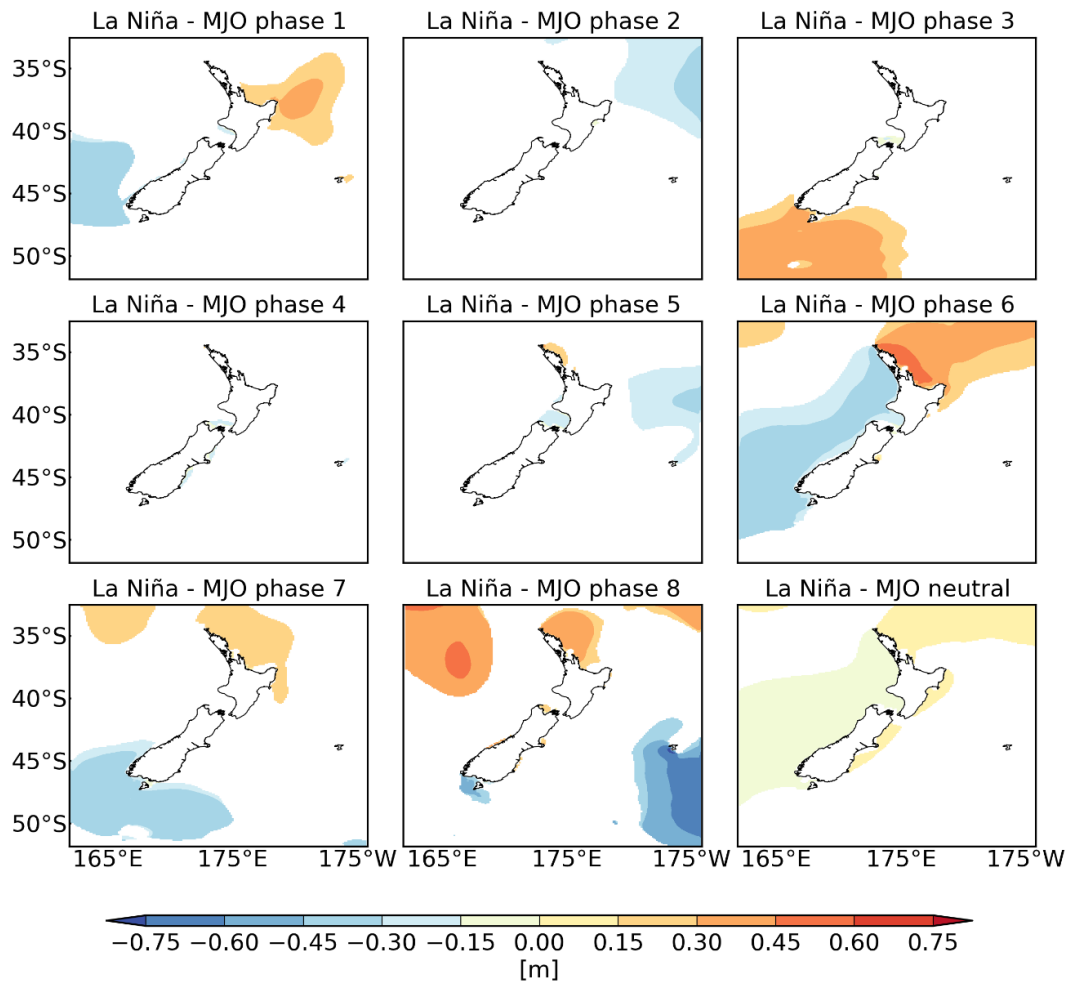


Figure 5.5. Significant wave height daily anomaly composites for La Niña with MJO phases over the November–March season during the period 1979–2002. Only statistically significant anomalies at the 95% confidence level are displayed. Statistical significance was calculated using Student’s t-test.

Part of the usual H_s anomaly pattern experienced in New Zealand waters under El Niño conditions (Gorman *et al.*, 2003b; Godoi *et al.*, 2016) is also found during La Niña-MJO phase 3 (Figure 5.5), and resembles the H_s anomalies observed during El Niño-MJO phase 5 (Figure 5.4). Not surprisingly, a westerly flow is observed to the south of the country in the wind composites for both phase pairs (Figure 5.1 and Figure 5.2), which is induced by an anti-cyclonic circulation (Seo and Son, 2012). This pattern suggests that the MJO-related conditions prevail over the conditions associated with the ENSO during La Niña-MJO phase 3, since easterly winds are generally experienced to the south of New Zealand during La

Niña events (Gordon, 1986). For both variables (H_s and wind), the anomalies associated with La Niña are weaker and occupy a smaller area than those related to El Niño. Another similarity between opposite ENSO phases is found during El Niño-MJO phase 6 (Figure 5.4) and La Niña-MJO phase 4 (Figure 5.5). These combinations have only a minor statistically significant influence on H_s anomalies, which is mostly manifested in the strait between the North and South Islands.

5.3.2 Composites for ENSO neutral with MJO phases

There is no atmospheric convection associated with the ENSO during its inactive periods. Thus, such periods are generally characterised by weak anomalies in atmospheric convection along the equatorial Pacific Ocean, with corresponding little atmospheric circulation variability (Shimizu and Ambrizzi, 2016). Nonetheless, H_s anomalies around New Zealand can still be governed by the atmospheric variability associated with the MJO propagation (Marshall *et al.*, 2015) during ENSO neutral periods. Positive H_s anomalies are most prominent during ENSO neutral-MJO phase 7, occupying a large portion of the study area (Figure 5.6). These are generated by stronger winds to the northeast of New Zealand and, perhaps, by part of the long strip of positive wind anomalies in the Southern Ocean, which extends from the south of Australia all the way to the Drake Passage (Figure 5.3). Negative H_s anomalies are most pronounced during ENSO neutral-MJO phase 2 (Figure 5.6), principally off the east coast of New Zealand, coinciding with weaker winds to the south and southeast of the country (Figure 5.3). Negative anomalies in H_s also appear in a large area of the New Zealand region during the combinations of ENSO neutral with MJO phases 4, 5, and 8 (Figure 5.6). Curiously, the negative anomalies during ENSO neutral-MJO phase 5 cannot be explained by the wind composite for the same phase pair (Figure 5.3), unlike those found for ENSO neutral-MJO phase 4 and ENSO neutral-MJO phase 8. In addition to negative anomalies, positive H_s anomalies occur to the northeast of the country and along some sectors immediately adjacent to the north and east coasts during ENSO neutral-MJO phase 8 (Figure 5.6). The wind anomalies observed during ENSO neutral (Figure 5.3) agree with the circulation anomaly composites obtained by Seo and Son (2012), who analysed the atmospheric circulation patterns associated with

the MJO. During ENSO neutral-MJO neutral, the wave variability associated with other climate oscillations results in relatively small negative H_s anomalies (down to -0.15 m) along and off the west and south coasts of the country, whereas positive anomalies (up to 0.15 m) occur along part of the east coast (Figure 5.6). Such anomalies are a consequence of small variability in wind intensity (Figure 5.3).

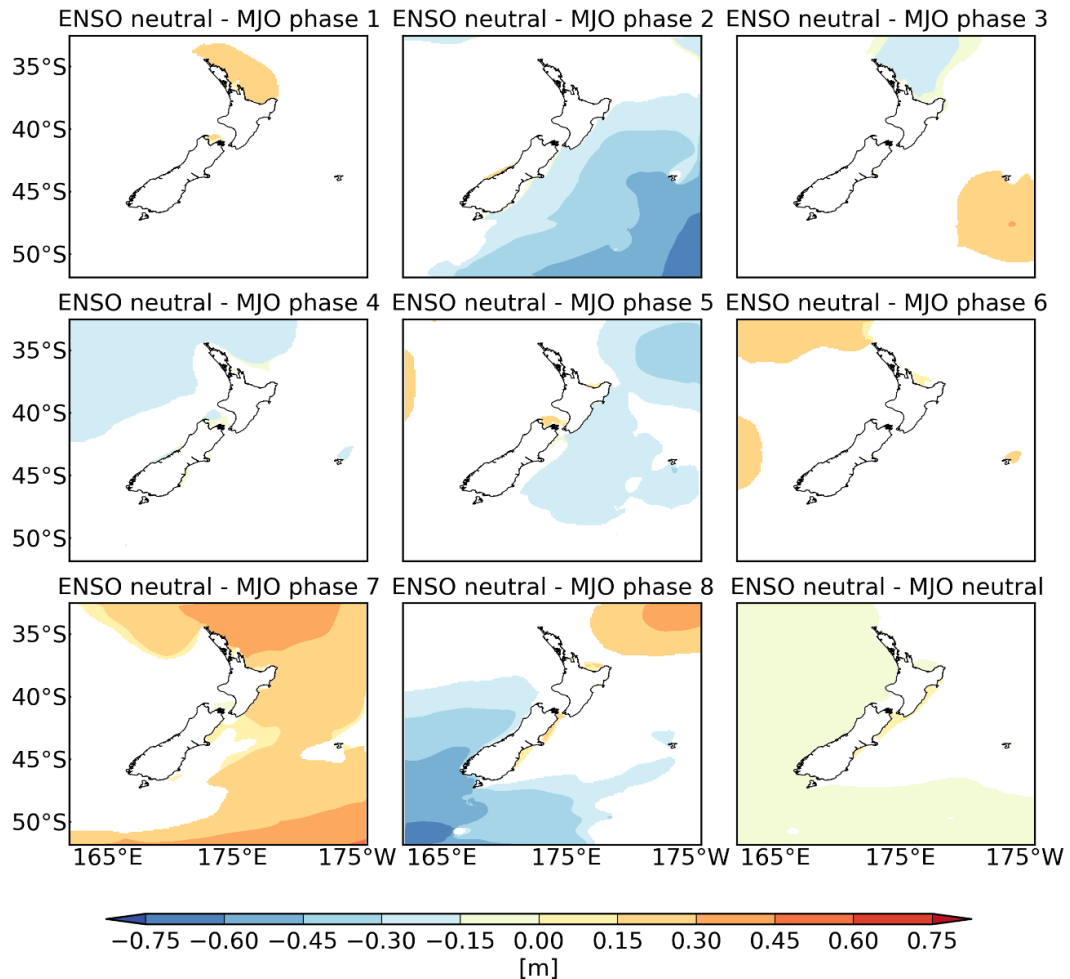


Figure 5.6. Significant wave height daily anomaly composites for ENSO neutral with MJO phases over the November–March season during the period 1979–2002. Only statistically significant anomalies at the 95% confidence level are displayed. Statistical significance was calculated using Student’s t-test.

5.3.3 ENSO-MJO combined activity versus MJO activity

Marshall *et al.* (2015) investigated the association of H_s anomalies with the MJO all over the world. Some of the H_s anomaly patterns reported here agree with

their results for the New Zealand region, not only when the ENSO is inactive, which would be expected, but also during El Niño and La Niña events. In both studies (during the ENSO neutral conditions assessed by us - Figure 5.6), negative H_s anomalies are noted along and off the north coast (MJO phase 3), off the west coast (MJO phase 4), and off the east and northeast coasts (MJO phase 5), whilst positive anomalies are found off the north coast (MJO phase 7 and 8). The predominance of the MJO-related conditions over the El Niño and La Niña ones are shown through nullification of the H_s anomalies expected during active ENSO phases, through reversal of their sign, or through the emergence of statistically significant anomalies where they are non-existent during active ENSO phases. This is evident during MJO phases 4 (negative anomalies off the west coast) and 6 (absence of H_s anomalies) for El Niño episodes, and during MJO phase 5 (negative anomalies off the east coast) for La Niña conditions. Additionally, positive [negative] H_s anomalies along and off the north coast during the MJO phase 7 [3] (Marshall *et al.*, 2015) explain why similar anomalies during La Niña-MJO neutral [El Niño-MJO neutral] are strengthened during La Niña-MJO phase 7 [El Niño-MJO phase 3]. All these features highlight the importance of the MJO to the modulation of ENSO-related low-frequency atmospheric and oceanic disturbances.

5.4 Conclusions

Anomalies in H_s driven by wind anomalies associated with combined activity in the ENSO and MJO were investigated in New Zealand waters during the extended austral summer (November–March) for the period 1979–2002. In order to do so, the composite analysis technique was applied to H_s daily anomaly fields, computed from modelled results sourced from a long-term wave hindcast, and to wind daily anomalies, calculated from the wind fields at 10 m used to force the hindcast simulation.

Atmospheric convection plays a vital role in regulating the large-scale atmospheric circulation (Bony *et al.*, 2015) and, consequently, the physical processes in the ocean. By transferring moisture and heat from the lower to the upper troposphere, atmospheric convection can affect remote areas through

teleconnections, interfering significantly in the local climate of distant regions. Remarkable differences in wind and wave patterns are observed for different ENSO phases as the sub-seasonal atmospheric convection related to the MJO propagates along the tropics. In general, anomalies in both wind and H_s are notably stronger during El Niño than during La Niña in combinations with active MJO phases. This might be because El Niño is associated with substantial atmospheric and oceanic changes contrary to the climatological pattern (e.g., warm SST where cold SST is normally found), while the climatological pattern is strengthened during La Niña. Wind anomalies during the combinations El Niño-MJO phase 8 and La Niña-MJO phase 6 enhance the wave heights around New Zealand relative to when active ENSO phases occur in the absence of significant MJO activity. On the other hand, the combinations El Niño-MJO phase 6 and La Niña-MJO phase 4 culminate in cancelling effects and, therefore, have little impact on H_s anomalies. The positive H_s anomalies expected during El Niño episodes show opposite sign in part of the study area and no statistical significance elsewhere when El Niño occurs with MJO phase 4. Characteristics of the H_s pattern observed during El Niño-MJO phase 5 (positive anomalies to the south of New Zealand) arise with weaker intensity when La Niña coexists with MJO phase 3. When no significant ENSO-related effects occur, the largest positive [negative] H_s anomalies along the coastline occur along the north [south] coast (ENSO neutral-MJO phase 7 [8]). The notable differences in H_s anomalies observed in the New Zealand region between inactive and active phases of the ENSO and MJO demonstrate the importance of accounting for combined effects associated with these oscillations in atmospheric and oceanic predictions.

The magnitude of H_s anomalies obtained during periods in which the ENSO and MJO co-existed may also be influenced by wind anomalies associated with other climate oscillations not included in the present analysis. Moreover, our study has investigated how wind anomalies associated with combined activity in the ENSO and MJO affect wave anomalies around New Zealand, but has not addressed in detail what conditions drive these wind anomalies. Nevertheless, our results show that some particular combinations of the ENSO and MJO are associated with hazardous conditions, especially along the southwestern coastline, and future

hazard predictions should at least consider the co-occurrence of these two oscillations.

CHAPTER 6: Summary

This thesis thoroughly assessed changes to the wave climate around New Zealand and their relationships with atmospheric fluctuations at several timescales. Such changes are of primary importance to the planning of offshore oil industry operations and shipping routes, to the construction and maintenance of coastal structures (mitigation of potential coastal hazards), and to the monitoring of erosion and sediment transport. New Zealand is an island nation, so malfunctioning of these elements might have serious implications for the safety and economics of several industrial and societal sectors, which would lead to New Zealand being critically affected on national and international scales.

The relationships between climate oscillations and changes in several wave parameters and storm wave clustering conditions were evaluated through linear correlations and spectral and compositing analyses. An approach previously used to identify atmospheric clusters was modified and used to identify storm wave clusters. The technique provided the ability to analyse storm wave clustering conditions over a large area; past studies have only been able to focus on the beach scale. A climatology was established to assess past extreme wave events, whereas their expected future behaviour was estimated by employing two extreme value statistical methods. The mean and extreme wave climates were spatially characterised through cluster analyses, facilitating the understanding of the features associated with different wave conditions. Linear and monotonic trends in wave and cluster parameters were calculated to understand their long-term rates of change.

The steps above were accomplished using long-term numerically-modelled data as the main tool. Results comprise the identification of the periods in which larger waves are more frequently observed, as well as of the regions around the country affected by these waves. Areas with greatest annual and inter-annual variabilities of the mean and extreme significant wave height are potentially the most vulnerable to uncertainties under climate changes, and these areas were also identified here. Regions more susceptible to cluster-induced coastal erosion were

also determined. Moreover, significant trends in several parameters of the mean, storm, and extreme wave climates related to hazardous conditions were detected, revealing the need to incorporate these trends in coastal planning by local and regional governments.

More specifically, Chapter 2 showed that the largest mean annual and inter-annual variabilities occur in regions along the coastline dominated by local winds, and that increasing wave heights are found in the great majority of the study region. All wave parameters assessed showed an association with the five climate oscillations considered, with negative phases of the ENSO and ZW3 and positive phases of the SAM, IOD, and PDO being associated with the most pronounced effects.

Chapter 3 showed that the wave hindcast was not able to reproduce the largest waves. Nevertheless, the hindcast data still allowed the investigation of the frequency and spatial pattern of extreme waves. The frequency of extreme waves was shown to vary considerably in the New Zealand region throughout the year, whereas their monthly spatial patterns did not vary substantially. The south and east coasts of the country were shown to have been impacted by more frequent extreme waves. Similar to the mean wave climate, mean annual and inter-annual variabilities were identified along sectors of the coastline dominated by local conditions. Although not investigated, extreme waves around New Zealand seem to be associated with La Niña-like effects and the SAM.

Storm clustering conditions were explored in Chapter 4. They were found to be more hazardous on the south and northwest coasts of New Zealand because of intense and recurrent southwesterly swells. Storm wave clusters have increased in duration besides having become more intense and having incorporated more storms. Strong relationships between these systems and climate patterns were also noted. Increases in clusters to the southwest of New Zealand occurred during El Niño and El Niño-like conditions (positive IOD/PDO), to the north of the country during La Niña and La Niña-like conditions, on the west coast during negative ZW3, and to the south of New Zealand during positive SAM.

In Chapter 5, the wind conditions associated with combined activity in the MJO and ENSO were shown to affect the wave climate around New Zealand significantly. Increases/decreases in wave height as well as an absence of its anomalies, compared to when the MJO is inactive, were found to occur during simultaneous MJO-ENSO phase combinations.

In summary, this thesis led to new understanding of:

- the correlation of the mean wave climate around New Zealand with several climate patterns, especially with the IOD and ZW3;
- how storm wave clusters behave around New Zealand, and how they are affected by atmospheric fluctuations associated with the ENSO, IOD, PDO, SAM, and ZW3. Moreover, for the first time, a simple and objective method was implemented to identify storm wave clusters, and this can be used for any other region of the globe;
- changes in the frequency of extreme wave events along the New Zealand coastline;
- the wave variability around New Zealand in response to atmospheric fluctuations associated with combined activity in the MJO and ENSO.

This thesis uncovered several future avenues of research. Links between the wave climate around New Zealand and atmospheric conditions associated with other climate oscillations should also be assessed in detail. Although the effects of such atmospheric conditions on the wave climate around New Zealand are likely to be less pronounced than the ones addressed here, they might still be significant and deserve investigation. Here, I selected two climate oscillations whose combined activity was likely to have associated conditions that would strongly influence the wave climate around the country. However, I have not investigated other potential combinations. The results presented and discussed throughout this work highlight the need for an extension to shallower waters, so that a more detailed picture of the coastal impacts can be obtained. This can be achieved by using datasets with higher spatial and temporal resolutions. In this case, other effects should also be accounted for, such as tidal variations, wave diffraction and reflection, and wave-current and wave-bottom interactions. In order to do so, a

detailed bathymetry around the whole coastline of New Zealand is required. Additionally, a reasonable number of buoys with long records will be necessary to validate the model. Although wave models have improved substantially, their results will always need validation. Therefore, more efforts should be put into collecting data. An even more realistic scenario of wave impacts on the coast requires the coupling of wave, hydrodynamic, and storm surge models. Nevertheless, this thesis provided new insights into the wave climate of a region not explored so much yet, but with an internationally growing recognition of its relevance (e.g., Rusu and Guedes Soares, 2009).

The present contribution may assist New Zealand to better prepare for multi-hazard effects resultant from the combination of large waves with increases in sea level (Hannah, 2004; Hannah and Bell, 2012; Walsh *et al.*, 2012) and stronger storms (Geng and Sugi, 2003; Emanuel, 2005; Bengtsson *et al.* 2006; Knutson *et al.*, 2010; Stephens and Ramsay, 2014). Furthermore, my results provide a background for climatological studies, which should be consistently updated as more data are made available. Lastly, the techniques used here can be applied in other studies to fully characterise the wave climate of other regions, especially those in the Southern Hemisphere, which have not been as much explored as the ones in Northern Hemisphere.

REFERENCES

- Alexander MA, Bladé I, Newman M, Lanzante JR, Lau N, Scott JD. 2002. The Atmospheric Bridge: The influence of ENSO teleconnections on air-sea interaction over the global oceans. *Journal of Climate* **15(16)**: 2205–2231. doi: 10.1175/1520-0442(2002)015<2205:TABTIO>2.0.CO;2.
- Almeida LP, Vousdoukas MV, Ferreira Ó, Rodrigues BA, Matias A. 2012. Thresholds for storm impacts on an exposed sandy coastal area in southern Portugal. *Geomorphology* **143–144**: 3–12. doi: 10.1016/j.geomorph.2011.04.047.
- Alves JHGM, Young IR. 2003. On estimating extreme wave heights using combined Geosat, Topex/Poseidon and ERS-1 altimeter data. *Applied Ocean Research* **25**: 167–186. doi: 10.1016/j.apor.2004.01.002.
- Amante C, Eakins BW. 2009. ETOPO1 1 Arc-Minute Global Relief Model: procedures, data sources and analysis, *NOAA Technical Memorandum NESDIS NGDC-24*, National Geophysical Data Center, NOAA, Boulder, Colorado. doi: 10.7289/V5C8276M.
- Arblaster JM, Meehl GA. 2006. Contributions of External Forcings to Southern Annular Mode Trends. *Journal of Climate* **19**: 2896–2905. doi: 10.1175/JCLI3774.1.
- Ardhuin F, Herbers THC, van Vledder GP, Watts KP, Jessen R, Graber HC. 2007. Swell and slanting fetch effects on wind wave growth. *Journal of Physical Oceanography* **37**: 908–931. doi: 10.1175/JPO3039.1.
- Ardhuin F, Rogers WE, Babanin AV, Filipot J-F, Magne R, Roland A, van der Westhuysen A, Queffeuilou P, Lee B, Aouf L, Collard F. 2010. Semiempirical dissipation source functions for ocean waves. Part I: definition, calibration, and validation. *Journal of Physical Oceanography* **40(9)**: 1917–1941. doi: 10.1175/2010JPO4324.1.

- Ashok K, Behera SK, Rao SA, Weng H, Yamagata T. 2007. El Niño Modoki and its possible teleconnection. *Journal of Geophysical Research: Oceans* **112(C11007)**. doi: 10.1029/2006JC003798.
- Balke T, Bouma TJ, Herman PMJ, Horstman EM, Sudtongkong C, Webb EL. 2013. Cross-shore gradients of physical disturbance in mangroves: implications for seedling establishment. *Biogeosciences* **10**: 5411–5419. doi: 10.5194/bg-10-5411-2013.
- Balouin Y, Tesson J, Gervais M. 2013. Cuspate shoreline relationship with nearshore bar dynamics during storm events – field observations at Sète beach, France. *Journal of Coastal Research SI65 (Proceedings 12th International Coastal Symposium – Plymouth, England)* **1**: 440–445. doi: 10.2112/SI65-075.1.
- Barnard PL, Short AD, Harley MD, Splinter KD, Vitousek S, Turner IL, Allan J, Banno M, Bryan KR, Doria A, Hansen JE, Kato S, Kuriyama Y, Randall-Goodwin E, Ruggiero P, Walker IJ, Heathfield DK. 2015. Coastal vulnerability across the Pacific dominated by El Niño/Southern Oscillation. *Nature Geoscience* **8**: 801–807. doi: 10.1038/NGEO2539.
- Barnston AG, Livezey RE. 1987. Classification, seasonality and persistence of low-frequency atmospheric circulation patterns. *Monthly weather review* **115(6)**: 1083–1126. doi: 10.1175/1520-0493(1987)115<1083:CSAPOL>2.0.CO;2.
- Bell RG, Goring DG, de Lange WP. 2000. Sea-level change and storm surges in the context of climate change. *The Institution of Professional Engineers New Zealand (IPENZ) Transactions* **27(1)**: 1–10.
- Benavente J, Del Río L, Plomaritis TA, Menapace W. 2013. Impact of coastal storm in a sandy barrier (Sancti Petri, Spain). *Journal of Coastal Research SI65 (Proceedings 12th International Coastal Symposium – Plymouth, England)* **1**: 666–671. doi: 10.2112/SI65-113.1.

- Bender III LC, Guinasso Jr NL, Walpert JN, Howen SD. 2010. A comparison of methods for determining significant wave height – applied to a 3m discus buoy during hurricane Katrina. *J. Atmos. Oceanic Technol.* **27**: 1012–1028. doi: 10.1175/2010JTECHO724.1.
- Bengtsson L, Hagemann S, Hodges KI. 2004. Can climate trends be calculated from reanalysis data? *Journal of Geophysical Research: Atmospheres* **109**: D11111. doi: 10.1029/2004JD004536.
- Bengtsson L, Hodges KI, Roeckner E. 2006. Storm tracks and climate change. *Journal of Climate* **19**: 3518–3543. doi: 10.1175/JCLI3815.1.
- Birkemeier WA, Nicholls RJ, Lee G. 1999. Storms, storm groups and nearshore morphologic change. In: Kraus, N.C., McDougal, W. (Eds.), *Coastal Sediments '99, ASCE* **1–3**: 1109–1122.
- Bjerknes J. 1961. "El Niño" study based on analysis of ocean surface temperatures 1935-57. *Inter-American Tropical Tuna Commission Bulletin* **5(3)**: 217–303.
- Bjerknes J. 1966. A possible response of the atmospheric Hadley circulation to equatorial anomalies of ocean temperature. *Tellus* **18(4)**: 820–829. doi: 10.1111/j.2153-3490.1966.tb00303.x.
- Bony S, Stevens B, Frierson DMW, Jakob C, Kageyama M, Pincus R, Shepherd TG, Sherwood SC, Siebesma AP, Sobel AH, Watanabe M, Webb MJ. 2015. Clouds, circulation and climate sensitivity. *Nature Geoscience* **8**: 261–268. doi:10.1038/ngeo2398.
- Bosserelle C, Charitha P, Haigh I. 2012. Inter-annual variability and longer-term changes in the wave climate of Western Australia between 1970 and 2009. *Ocean Dynamics* **62(1)**: 63–76. doi: 10.1007/s10236-011-0487-3.
- Bretherton FP, Garrett CJR. 1969: Wavetrains in inhomogeneous moving media. *Proc. Roy. Soc. London A* **302**: 529–554. doi: 10.1098/rspa.1968.0034.

- Bromirski PD, Cayan DR, Flick RE. 2005. Wave spectral energy variability in the northeast Pacific. *J. Geophys. Res.* **110**: C03005. doi: 10.1029/2004JC002398.
- Bromwich DH, Fogt RL. 2004. Strong trends in the skill of the ERA-40 and NCEP–NCAR reanalyses in the high and midlatitudes of the southern hemisphere, 1958–2001. *Journal of Climate* **17**: 4603–4619. doi: 10.1175/3241.1.
- Bryan KR, Kench PS, Hart DE. 2008. Multi-decadal coastal change in New Zealand: Evidence, mechanisms and implications. *New Zealand Geographer* **64(2)**: 117–128. doi: 10.1111/j.1745-7939.2008.00135.x.
- Cai W, Baines PG, Gordon HB. 1999. Southern mid- to high-latitude variability, a zonal wavenumber-3 pattern, and the Antarctic circumpolar wave in the CSIRO coupled model. *Journal of Climate* **12**: 3087–3104. doi: 10.1175/1520-0442(1999)012<3087:SMTHLV>2.0.CO;2.
- Cai W, Borlace S, Lengaigne M, van Rensch P, Collins M, Vecchi G, Timmermann A, Santoso A, McPhaden MJ, Wu L, England MH, Wang G, Guilyardi E, Jin F-F. 2014. Increasing frequency of extreme El Niño events due to greenhouse warming. *Nat. Clim. Change* **4**: 111–116. doi: 10.1038/nclimate2100.
- Cai W, Santoso A, Wang G, Weller E, Wu L, Ashok K, Masumoto Y, Yamagata T. 2014. Increased frequency of extreme Indian Ocean Dipole events due to greenhouse warming. *Nature* **510**: 254–258. doi: 10.1038/nature13327.
- Cai W, van Rensch P, Cowan T. 2011. Teleconnection pathways of ENSO and the IOD and the mechanisms for impacts on Australian rainfall. *Journal of Climate* **24**: 3910–3923. doi: 10.1175/2011JCLI4129.1.
- Cai W, Wang G, Santoso A, McPhaden MJ, Wu L, Jin F, Timmermann A, Collins M, Vecchi G, Lengaigne M, England MH, Dommenges D, Takahashi K, Guilyardi E. 2015. Increased frequency of extreme La Niña events under greenhouse warming. *Nat. Clim. Change* **5**: 132–137. doi: 10.1038/nclimate2492.

- Caires S, Sterl A. 2003. Validation of ocean wind and wave data using triple collocation. *Journal of Geophysical Research* **108(C3)**: 3098. doi: 10.1029/2002JC001491.
- Caires S, Sterl A. 2005. 100-Year return value estimates for ocean wind speed and significant wave height from the ERA-40 data. *Journal of Climate* **18**: 1032–1048. doi: 10.1175/JCLI-3312.1.
- Caires S, Sterl A, Bidlot J-R, Graham N, Swail V. 2004. Intercomparison of different wind-wave reanalyses. *Journal of Climate* **17(10)**: 1893–1913. doi: 10.1175/1520-0442(2004)017<1893:IODWR>2.0.CO;2.
- Caires S, Swail VR, Wang XL. 2006. Projection and analysis of extreme wave climate. *Journal of Climate* **19(21)**: 5581–5605. doi: 10.1175/JCLI3918.1.
- Cane MA. 2005. The evolution of El Niño, past and future. *Earth and Planetary Science Letters* **230(3)**: 227–240. doi: 10.1016/j.epsl.2004.12.003.
- Carter DJT, Draper L. 1988. Has the north-east Atlantic become rougher? *Nature* **332**: 494. doi: 10.1038/332494a0.
- Cavaleri L. 2009. Wave modeling – Missing the peaks. *Journal of Physical Oceanography* **39**: 2757–2778. doi: 10.1175/2009JPO4067.1.
- Cavaleri L, Malanotte-Rizzoli P. 1981. Wind-wave prediction in shallow water: theory and applications. *Journal of Geophysical Research* **86(C11)**: 10961–10973. doi: 10.1029/JC086iC11p10961.
- Chase TN, Sr RAP, Avissar R. 2006. Teleconnections in the Earth System. *Encyclopedia of Hydrological Sciences*, John Wiley & Sons. doi: 10.1002/0470848944.hsa190.
- Chawla A, Spindler DM, Tolman HL. 2013. Validation of a thirty year wave hindcast using the Climate Forecast System Reanalysis winds. *Ocean Modelling* **70**: 189–206. doi: 10.1016/j.ocemod.2012.07.005.
- Chen G, Chapron B, Ezraty R, Vandemark D. 2002. A global view of swell and wind sea climate in the ocean by satellite altimeter and scatterometer. *Journal*

- of Atmospheric and Oceanic Technology* **19**: 1849–1859. doi: 10.1175/1520-0426(2002)019<1849:AGVOSA>2.0.CO;2.
- Chiswell SM, Bostock HC, Sutton PJH, Williams MJM. 2015. Physical oceanography of the deep seas around New Zealand: a review. *New Zealand Journal of Marine and Freshwater Research* **49(2)**: 286–317. doi: 10.1080/00288330.2014.992918.
- Coco G, Senechal N, Rejas A, Bryan KR, Capo S, Parisot JP, Brown JA, MacMahan JHM. 2014. Beach response to a sequence of extreme storms. *Geomorphology* **204**: 493–501. doi: 10.1016/j.geomorph.2013.08.028.
- Coggins JHJ, Parsons S, Schiel D. 2015. An assessment of the ocean wave climate of New Zealand as represented in Kidson's synoptic types. *Int. J. Climatol.* **36**: 2481–2496. doi: 10.1002/joc.4507.
- Coles SG. 2001. An Introduction to Statistical Modelling of Extreme Values. Springer, London. doi: 10.1007/978-1-4471-3675-0.
- Collins M, An S-I, Cai W, Ganachaud A, Guilyardi E, Jin F-F, Jochum M, Lengaigne M, Power S, Timmermann A, Vecchi G, Wittenberg A. 2010. The impact of global warming on the tropical Pacific Ocean and El Niño. *Nature Geoscience* **3**: 391–397. doi: 10.1038/NGEO868.
- Cox AT, Swail VR. 2001. A global wave hindcast over the period 1958–1997: Validation and climate assessment. *Journal of Geophysical Research* **106(C2)**: 2313–2329. doi: 10.1029/2001JC000301.
- Cruz J. 2008. Ocean wave energy: current status and future perspectives. Springer. doi: 10.1007/978-3-540-74895-3.
- Dai A, Wigley, TML. 2000. Global patterns of ENSO-induced precipitation. *Geophysical Research Letters* **27(9)**: 1283–1286. doi: 10.1029/1999GL011140.

- Davis RE. 2005. Intermediate-depth circulation of the Indian and South Pacific oceans measured by autonomous floats. *Journal of Physical Oceanography* **35(5)**: 683–707. doi: 10.1175/JPO2702.1.
- Dayton PK, Tegner MJ, Parnell PE, Edwards PB. 1992. Temporal and spatial patterns of disturbance and recovery in a kelp forest community. *Ecological Monographs* **62(3)**: 421–445. doi: 10.2307/2937118.
- de Lange WP. 2001. Interdecadal Pacific Oscillation (IPO): a mechanism for forcing decadal scale coastal change on the northeast coast of New Zealand? *Journal of Coastal Research* SI **34**: 657–664.
- Deser C, Alexander MA, Xie S, Phillips AS. 2010. Sea surface temperature variability: Patterns and mechanisms. *Annu. Rev. Mar. Sci.* **2**: 115–143. doi: 10.1146/annurev-marine-120408-151453.
- Dissanayake P, Brown J, Karunaratna H. 2015a. Impacts of storm chronology on the morphological changes of the Formby beach and dune system, UK. *Nat. Hazards Earth Syst. Sci.* **15**: 1533–1543. doi: 10.5194/nhess-15-1533-2015.
- Dissanayake P, Brown J, Wisse P, Karunaratna H. 2015b. Comparison of storm cluster vs isolated event impacts on beach/dune morphodynamics. *Estuarine, Coastal and Shelf Science* **164**: 301–312. doi: 10.1016/j.ecss.2015.07.040.
- Dissanayake P, Brown J, Wisse P, Karunaratna H. 2015c. Effects of storm clustering on beach/dune evolution. *Marine Geology* **370**: 63–75. doi: 10.1016/j.margeo.2015.10.010.
- Dolan R, Davis R. 1994. Coastal storm hazards. *Journal of Coastal Research* **SI12**: *Coastal Hazards*: 103–114.
- Domingues CM, Church JA, White NJ, Gleckler PJ, Wijffels SE, Barker PM, Dunn JR. 2008. Improved estimates of upper-ocean warming and multi-decadal sea-level rise. *Nature* **453**: 1090–1093. doi: 10.1038/nature07080.

- Drost F, Renwick J, Bhaskaran B, Oliver H, McGregor J. 2007. Simulation of New Zealand's climate using a high-resolution nested regional climate model. *International Journal of Climatology* **27**: 1153–1169. doi: 10.1002/joc.1461.
- Durrant T, Greenslade D, Hemer M, Trenham C. 2014. A global wave hindcast focussed on the Central and South Pacific. *CAWCR Technical Report* **70**.
- Durrant TH, Greenslade DJM, Simmonds I. 2009. Validation of Jason-1 and Envisat remotely sensed wave heights. *J. Atmos. Ocean. Tech.* **26**: 123–134. doi: 10.1175/2008JTECHO598.1.
- Economou T, Stephenson DB, Pinto JG, Shaffrey LC, Zappa G. 2015. Serial clustering of extratropical cyclones in a multi-model ensemble of historical and future simulations. *Quarterly Journal of the Royal Meteorological Society* **141(693)**: 3076–3087. doi: 10.1002/qj.2591.
- Emanuel K. 2005. Increasing destructiveness of tropical cyclones over the past 30 years. *Nature Letters* **436(4)**: 686–688. doi: 10.1038/nature03906.
- Fan Y, Lin S-J, Held IM, Yu Z, Tolman HL. 2012. Global ocean surface wave simulation using a coupled atmosphere-wave model. *Journal of climate* **25**: 6233–6252. doi: 10.1175/JCLI-D-11-00621.1.
- Farge M. 1992. Wavelet transforms and their applications to turbulence. *Annu. Rev. Fluid Mech.* **24**: 395–457. doi: 10.1146/annurev.fl.24.010192.002143.
- Fawcett L, Walshaw D. 2008. Bayesian inference for clustered extremes. *Extremes* **11**: 217–233. doi: 10.1007/s10687-007-0054-y.
- Ferreira Ó. 2002. Prediction of the impact of storm groups and their importance in coastal evolution. *Proceedings of the international conference on Coastal Engineering '02 (ASCE)*: 2725–2730. doi: 10.1680/scc.42377.0152.
- Ferreira Ó. 2005. Storm groups versus extreme single storms: predicted erosion and management consequences. *Journal of Coastal Research* **SI42**: 221–227.

- Ferreira Ó. 2006. The role of storm groups in the erosion of sandy coasts. *Earth Surf. Process. Landforms* **31**: 1058–1060. doi: 10.1002/esp.1378.
- Ferreira JA, Guedes Soares C. 1998. An application of the Peaks Over Threshold method to predict extremes of significant wave height. *Journal of Offshore Mechanics and Arctic Engineering* **120(3)**: 165–176. doi: 10.1115/1.2829537.
- Garreaud R, Battisti DS. 1999. Interannual (ENSO) and Interdecadal (ENSO-like) variability in the Southern Hemisphere tropospheric circulation. *Journal of Climate* **12(7)**: 2113–2123. doi: 10.1175/1520-0442(1999)012<2113:IEAIEL>2.0.CO;2.
- Gemrich J, Thomas B, Bouchard R. 2011. Observational changes and trends in northeast Pacific wave records. *Geophys. Res. Lett.* **38**: L22601. doi: 10.1029/2011GL049518.
- Geng Q, Sugi M. 2003. Possible change of extratropical cyclone activity due to enhanced greenhouse gases and sulfate aerosols — study with a high-resolution AGCM. *Journal of Climate* **16**: 2262–2274. doi: 10.1175/1520-0442(2003)16<2262:PCOECA>2.0.CO;2.
- Gillett NP, Thompson DWJ. 2003. Simulation of recent Southern Hemisphere climate change. *Science* **302(5643)**: 273–275. doi: 10.1126/science.1087440.
- Girishkumar MS, Suprit K, Vishnu S, Thanga Prakash VP, Ravichandran M. 2015. The role of ENSO and MJO on rapid intensification of tropical cyclones in the Bay of Bengal during October–December. *Theor Appl Climatol* **120**: 797–810. doi: 10.1007/s00704-014-1214-z.
- Godoi VA, Bryan KR, Gorman RM. 2015. Spectral Analysis of the influence of the El Niño–Southern Oscillation on the north and south wave climates of New Zealand. *Australasian Coasts & Ports Conference 2015: 22nd Australasian Coastal and Ocean Engineering Conference and the 15th Australasian Port*

and Harbour Conference, Auckland, New Zealand: Engineers Australia and IPENZ. 320–324. ISBN: 9781922107794.

- Godoi VA, Bryan KR, Gorman RM. 2016. Regional influence of climate patterns on the wave climate of the southwestern Pacific: The New Zealand region. *J. Geophys. Res.: Oceans* **121(6)**: 4056–4076. doi: 10.1002/2015JC011572.
- Godoi VA, Bryan KR, Gorman RM. *in press*. Storm wave clustering around New Zealand and its connection to climatic patterns. *International Journal of Climatology*. doi: 10.1002/joc.5380.
- Godoi VA, Bryan KR, Stephens SA, Gorman RM. 2017. Extreme waves in New Zealand waters. *Ocean Modelling* **117C**: 97–110. doi: 10.1016/j.ocemod.2017.08.004.
- Gong D, Wang S. 1999. Definition of Antarctic Oscillation index. *Geophysical Research Letters* **26(4)**: 459–462. doi: 10.1029/1999GL900003.
- Gordon ND. 1986. The Southern Oscillation and New Zealand weather. *Monthly Weather Review* **14**: 371–387. doi: 10.1175/1520-0493(1986)114<0371:TSOANZ>2.0.CO;2.
- Gordon AL, Visbeck M, Comiso JC. 2007. A possible link between the Weddell Polynya and the Southern Annular Mode. *Journal of Climate* **20**: 2558–2571. doi: 10.1175/JCLI4046.1.
- Goring DG, Bell RG. 1999. El Niño and decadal effects on sea-level variability in northern New Zealand: A wavelet analysis. *New Zealand Journal of Marine and Freshwater Research* **33(4)**: 587–598. doi: 10.1080/00288330.1999.9516902.
- Gorman RM, Bryan KR, Laing AK. 2003a. Wave hindcast for the New Zealand region: Nearshore validation and coastal wave climate, *N. Z. J. Mar. Freshwater Res.* **37(3)**: 567–588. doi: 10.1080/00288330.2003.9517190.

- Gorman RM, Bryan KR, Laing AK. 2003b. Wave hindcast for the New Zealand region: Deep-water wave climate. *N. Z. J. Mar. Freshwater Res.* **37(3)**: 589–612. doi: 10.1080/00288330.2003.9517191.
- Gorman RM, Bell RG, Lane EM, Gillibrand PA, Stephens SA. 2010. New Zealand wave climate – simulating the past and future. Paper presented at *New Zealand Coastal Society Annual Conference*, New Zealand Coastal Society, Whitianga, New Zealand, 17–19 November, 2010.
- Grimm AM. 2003. The El Niño impact on the summer monsoon in Brazil: regional processes versus remote influences. *Journal of Climate* **16(2)**: 263–280. doi: 10.1175/1520-0442(2003)016<0263:TENIOT>2.0.CO;2.
- Grimm AM, Ambrizzi T. 2009. Teleconnections into South America from the tropics and extratropics on interannual and intraseasonal timescales. *Past Climate Variability in South America and Surrounding Regions. Developments in Paleoenvironmental Research*. Springer, Dordrecht Netherlands, **14**: 159–191. doi: 10.1007/978-90-481-2672-9_7.
- Gringorten II. 1963. A plotting rule for extreme probability paper. *J. Geophys. Res.* **68(3)**: 813–814. doi: 10.1029/JZ068i003p00813.
- Grinsted A, Moore JC, Jevrejeva S. 2004. Application of the cross wavelet transform and wavelet coherence to geophysical time series. *Nonlinear Processes in Geophysics* **11**: 561–566. doi: 10.5194/npg-11-561-2004.
- Guedes Soares C, Scotto MG. 2004. Application of the r largest-order statistics for long-term predictions of significant wave height. *Coastal Engineering* **51**: 387–394. doi: 10.1016/j.coastaleng.2004.04.003.
- Gupta AS, England MH. 2007. Coupled ocean–atmosphere feedback in the Southern Annular Mode. *Journal of Climate* **20**: 3677–3692. doi: 10.1175/JCLI4200.1.
- Hannah J. 2004. An updated analysis of long-term sea level change in New Zealand. *Geophys. Res. Lett.* **31**: L03307. doi: 10.1029/2003GL019166.

- Hannah J, Bell RG. 2012. Regional sea level trends in New Zealand. *J. Geophys. Res.* **117**: C01004. doi: 10.1029/2011JC007591.
- Harley MD, Turner IL, Short AD, Ranasinghe R. 2009. An empirical model of beach response to storms – SE Australia. *Coasts and Ports 2009: In a Dynamic Environment*: 600–606.
- Harley MD, Turner IL, Short AD, Ranasinghe R. 2010. Interannual variability and controls of the Sydney wave climate. *International Journal of Climatology* **30**: 1322–1335. doi: 10.1002/joc.1962.
- Hartigan JA, Wong MA. 1979. Algorithm AS 136: A K-Means clustering algorithm. *Journal of the Royal Statistical Society – Series C (Applied Statistics)* **28(1)**: 100–108. doi: 10.2307/2346830.
- Hasselmann K, Barnett TP, Bouws E, Carlson H, Cartwright DE, Enke K, Ewing JA, Gienapp H, Hasselmann DE, Kruseman P, Meerburg A, Mueller P, Olbers DJ, Richter K, Sell W, Walden H. 1973. Measurements of wind-wave growth and swell decay during the Joint North Sea Wave Project (JONSWAP). *Dtsch. Hydrogr. Z.* **8(12)**: Suppl. A, 95.
- Hasselmann S, Hasselmann K, Allender JH, Barnett TP. 1985. Computations and parameterizations of the nonlinear energy transfer in a gravity-wave spectrum, Part II: parameterizations of the nonlinear energy transfer for application in wave models. *Journal of Physical Oceanography* **15(11)**: 1378–1391. doi: 10.1175/1520-0485(1985)015<1378:CAPOTN>2.0.CO;2.
- Hauer ME, Evans JM, Mishra DR. 2016. Millions projected to be at risk from sea-level rise in the continental United States. *Nature Climate Change* 1–5. doi: 10.1038/nclimate2961.
- Hayward TL. 1993. Preliminary observations of the 1991–1992 El Niño in the California Current. *California Cooperative Oceanic Fisheries Investigations Reports* **34**: 21–29.

- Hemer MA. 2010. Historical trends in Southern Ocean storminess: long-term variability of extreme wave heights at Cape Sorell, Tasmania. *Geophys. Res. Lett.* **37(18)**: L18601. doi: 10.1029/2010GL044595.
- Hemer MA, Church JA, Hunter JR. 2007. Waves and climate change on the Australian coast. *Journal of Coastal Research* **50**: 432–437.
- Hemer MA, Church JA, Hunter JR. 2010. Variability and trends in the directional wave climate of the Southern Hemisphere. *Int. J. Climatol.* **30(4)**: 475–491. doi: 10.1002/joc.1900.
- Hemer MA, Zieger S, Durrant T, O'Grady J, Hoeke RK, McInnes KL, Rosebrock U. 2017. A revised assessment of Australia's national wave energy resource. *Renewable Energy* **114(A)**: 85–107. doi: 10.1016/j.renene.2016.08.039.
- Hendon HH, Wheeler MC, Zhang C. 2007. Seasonal dependence of the MJO-ENSO relationship. *Journal of Climate* **20**: 531–543. doi: 10.1175/JCLI4003.1.
- Holthuijsen LH. 2007. Waves in oceanic and coastal waters. Cambridge University Press, New York. doi: 10.1017/CBO9780511618536.
- Horel JD, Wallace JM. 1981. Planetary-scale atmospheric phenomena associated with the Southern Oscillation. *Monthly Weather Review* **109(4)**: 813–829. doi: 10.1175/1520-0493(1981)109<0813:PSAPAW>2.0.CO;2.
- Horrillo-Caraballo JM, Pan S, Reeve DE, Simmonds D, Greaves D, Fox A. 2012. Modelling extreme wave events (present and future scenarios) in southwest England. *Paper presented at Proceedings of 33rd Conference on Coastal Engineering*, Santander, Spain, 1–6 July 2012. Published in Lynett, Patrick and Smith, Jane McKee eds, Coastal Engineering 2012, Proceedings of 33rd Annual Conference, 33, Coastal Engineering Research Council. doi: 10.9753/icce.v33.waves.46.
- Izaguirre C, Méndez FJ, Menéndez M, Losada JJ. 2011. Global extreme wave height variability based on satellite data. *Geophysical Research Letters* **38(10)**: L10607. doi: 10.1029/2011GL047302.

- Izumo T, Vialard J, Lengaigne M, Montegut CB, Behera SK, Luo J, Cravatte S, Masson S, Yamagata T. 2010. Influence of the state of the Indian Ocean Dipole on the following year's El Niño. *Nat. Geosci.* **3**: 168–172. doi: 10.1038/ngeo760.
- Jury MR, Enfield DB, Mélice J-L. 2002. Tropical monsoons around Africa: stability of El Niño-Southern Oscillation associations and links with continental climate. *Journal of Geophysical Research* **107(C10)**: 3151. doi: 10.1029/2000JC000507.
- Kanungo T, Mount DM, Netanyahu NS, Piatko CD, Silverman R, Wu AY. 2002. An efficient K-Means clustering algorithm: Analysis and implementation. *IEEE Transactions on Pattern Analysis and Machine Intelligence* **24(7)**: 881–892. doi: 10.1109/TPAMI.2002.1017616.
- Karoly DJ. 1989. Southern Hemisphere circulation features associated with El Niño-Southern Oscillation events. *Journal of Climate* **2(11)**: 1239–1252. doi: 10.1175/1520-0442(1989)002<1239:SHCF>2.0.CO;2.
- Karunaratna H, Pender D, Ranasinghe R, Short AD, Reeve DE. 2014. The effects of storm clustering on beach profile variability. *Marine Geology* **348**: 103–112. doi: 10.1016/j.margeo.2013.12.007.
- Kendall MG. 1955. Rank correlation methods. Charles Griffin and Company, London, 2nd edition.
- Kidson JW. 1988. Interannual variations in the Southern Hemisphere circulation. *Journal of Climate* **1(12)**: 1177–1198. doi: 10.1175/1520-0442(1988)001<1177:IVITSH>2.0.CO;2.
- Klotzbach PJ. 2012. El Niño-Southern Oscillation, the Madden-Julian Oscillation and Atlantic basin tropical cyclone rapid intensification. *J. Geophys. Res.* **117**: D14104, doi: 10.1029/2012JD017714.
- Knutson TR, McBride JL, Chan J, Emanuel K, Holland G, Landsea C, Held I, Kossin JP, Srivastava AK, Sugi M. 2010. Tropical cyclones and climate change. *Nature Geoscience* **3**: 157–163. doi: 10.1038/ngeo779.

- Komen GJ, Cavaleri L, Donelan M, Hasselmann K, Hasselmann S, Janssen PAEM. 1994. Dynamics and Modelling of Ocean Waves. Cambridge University Press: Cambridge. doi: 10.1002/qj.49712253016.
- Kousky VE, Kagano MT, Cavalcanti IFA. 1984. A review of the Southern Oscillation: oceanic-atmospheric circulation changes and related rainfall anomalies. *Tellus* **36A(5)**: 490-504. doi: 10.1111/j.1600-0870.1984.tb00264.x.
- Kriebel DL, Dean RG. 1993. Convolution method for time-dependent beach-profile response. *J. Waterway, Port., Coastal, Ocean Eng.* **119(2)**: 204–226. doi: 10.1061/(ASCE)0733-950X(1993)119:2(204).
- Kumar P, Min S-K, Weller E, Lee H, Wang XL. 2016. Influence of climate variability on extreme ocean surface wave heights assessed from ERA-Interim and ERA-20C. *Journal of Climate* **29**: 4031–4046. doi: 10.1175/JCLI-D-15-0580.1.
- Kushner PJ, Held IM, Delworth TL. 2001. Southern Hemisphere atmospheric circulation response to global warming. *Journal of Climate* **14**: 2238–2249. doi: 10.1175/1520-0442(2001)014<0001:SHACRT>2.0.CO;2.
- Kvamstø NG, Song Y, Seierstad IA, Sorteberg A, Stephenson DB. 2008. Clustering of cyclones in the ARPEGE general circulation model. *Tellus* **60A(3)**: 547–556. doi: 10.1111/j.1600-0870.2008.00307.x.
- Laing AK. 1993. Estimates of wave height data for New Zealand waters by numerical modelling. *New Zealand Journal of Marine and Freshwater Research* **27(2)**: 157–175. doi: 10.1080/00288330.1993.9516554.
- Laing AK. 2000. New Zealand wave climate from satellite observations. *N. Z. J. Mar. Freshwater Res.* **34(4)**: 727–744. doi: 10.1080/00288330.2000.9516973.
- Lavergne C, Palter JB, Galbraith ED, Bernardello R, Marinov I. 2014. Cessation of deep convection in the open Southern Ocean under anthropogenic climate change. *Nature Climate Change* **4**: 278–282. doi: 10.1038/NCLIMATE2132.

- Lee G, Nicholls RJ, Birkemeier WA. 1998. Storm-driven variability of the beach-nearshore profile at Duck, North Carolina, USA, 1981-1991. *Marine Geology* **148**: 163-177. doi: 10.1016/S0025-3227(98)00010-3.
- L'Heureux ML, Thompson DWJ. 2006. Observed relationships between the El Niño–Southern Oscillation and the extratropical zonal-mean circulation. *Journal of Climate* **19**: 276–287. doi: 10.1175/JCLI3617.1.
- Likas A, Vlassis N, Verbeek JJ. 2003. The global K-Means clustering algorithm. *Pattern Recognition* **36(2)**: 451–461. doi: 10.1016/S0031-3203(02)00060-2.
- Limpasuvan V, Hartmann DL. 1999. Eddies and the annular modes of climate variability. *Geophysical Research Letters*. **26(20)**: 3133–3136. doi: 10.1029/1999GL010478.
- Lin H, Derome J, Brunet G. 2007. The nonlinear transient atmospheric response to tropical forcing. *Journal of Climate* **20(22)**: 5642–5665. doi: 10.1175/2007JCLI1383.1.
- Liu PC. 1994. Wavelet spectrum analysis and ocean wind waves. *Wavelet analysis and its applications* **4**. Academic Press, New York. doi: 10.1016/B978-0-08-052087-2.50012-8.
- Liu Z, Alexander M. 2007. Atmospheric bridge, oceanic tunnel, and global climatic teleconnections. *Rev. Geophys.* **45**: RG2005. doi: 10.1029/2005RG000172.
- Lopatoukhin LJ, Rozhkov VA, Ryabinin VE, Swail VR, Boukhanovsky AV, Degtyarev AB. 2000. Estimation of extreme wave heights. *World Meteorological Organisation, Intergovernmental Oceanographic Commission (of UNESCO)*. WMO/TD-No. 1041. JCOMM Technical Report No. 9. 73 p.
- Loureiro C, Ferreira Ó, Cooper JAG. 2009. Contrasting morphologic behaviour at embayed beaches in Southern Portugal. *Journal of Coastal Research* **SI56** (Proceedings of the 10th International Coastal Symposium): 83–87.

- Loureiro C, Ferreira Ó, Cooper JAG. 2012. Extreme erosion on high-energy embayed beaches: Influence of megarips and storm grouping. *Geomorphology* **139–140**: 155–171. doi: 10.1016/j.geomorph.2011.10.013.
- Lovelock CE, Sorrell BK, Hancock N, Hua Q, Swales A. 2010. Mangrove forest and soil development on a rapidly accreting shore in New Zealand. *Ecosystems* **13(3)**: 437–451. doi: 10.1007/s10021-010-9329-2.
- Madden RA, Julian PR. 1971. Detection of a 40–50 day oscillation in the zonal wind in the tropical Pacific. *Journal of the atmospheric sciences* **28**: 702–708. doi: 10.1175/1520-0469(1971)028<0702:DOADOI>2.0.CO;2.
- Madden RA, Julian PR. 1972. Description of global-scale circulation cells in the tropics with a 40–50 day period. *Journal of the atmospheric sciences* **29**: 1109–1123. doi: 10.1175/1520-0469(1972)029<1109:DOGSCC>2.0.CO;2.
- Madden RA, Julian PR. 1994. Observations of the 40–50-day tropical oscillation – A review. *Monthly Weather Review* **122**: 814–837. doi: 10.1175/1520-0493(1994)122<0814:OOTDIO>2.0.CO;2.
- Mailier PJ, Stephenson DB, Ferro CAT. 2006. Serial clustering of extratropical cyclones. *Monthly Weather Review* **134**: 2224–2240. doi: 10.1175/MWR3160.1.
- Mann HB. 1945. Nonparametric tests against trend. *Econometrica* **13(3)**: 245–259. doi: 10.2307/1907187.
- Mantua NJ, Hare SR. 2002. The Pacific Decadal Oscillation. *Journal of Oceanography* **58(1)**: 35–44. doi: 10.1023/A:1015820616384.
- Mantua NJ, Hare SR, Zhang Y, Wallace JM, Francis RC. 1997. A Pacific interdecadal climate oscillation with impacts on salmon production. *Bull. Am. Meteorol. Soc.* **78(6)**: 1069–1079. doi: 10.1175/1520-0477(1997)078<1069:APICOW>2.0.CO;2.

- Marshall GJ. 2003. Trends in the Southern Annular Mode from observations and reanalyses. *J. Clim.* **16(24)**: 4134–4143. doi: 10.1175/1520-0442(2003)016<4134:TITSAM>2.0.CO;2.
- Marshall AG, Hendon HH, Durrant TH, Hemer MA. 2015. Madden Julian Oscillation impacts on global ocean surface waves. *Ocean Modelling* **96**: 136–147. doi: 10.1016/j.ocemod.2015.06.002.
- Massel SR. 2001. Wavelet analysis for processing of ocean surface wave records. *Ocean Engineering* **28**: 957–987. doi: 10.1016/S0029-8018(00)00044-5.
- Mathiesen M, Goda Y, Hawkes PJ, Mansard E, Martín MJ, Peltier E, Thompson EF, Vledder GV. 1994. Recommended practice for extreme wave analysis. *J. Hydraul. Res.* **32(6)**: 803–814. doi: 10.1080/00221689409498691.
- Matthews AJ. 2000. Propagation mechanisms for the Madden-Julian Oscillation. *Quarterly Journal of the Royal Meteorological Society* **126(569)**: 2637–2651. doi: 10.1002/qj.49712656902.
- Matthews AJ, Hoskins BJ, Masutani M. 2004. The global response to tropical heating in the Madden-Julian oscillation during the northern winter. *Quarterly Journal of the Royal Meteorological Society* **130(601)**: 1991–2011. doi: 10.1256/qj.02.123.
- Mazas F, Hamm L. 2011. A multi-distribution approach to POT methods for determining extreme wave heights. *Coastal Engineering* **58**: 385–394. doi: 10.1016/j.coastaleng.2010.12.003.
- McPhaden MJ, Timmermann A, Widlansky MJ, Balmaseda MA, Stockdale TN. 2015. The curious case of the El Niño that never happened: a perspective from 40 years of progress in climate research and forecasting. *Bulletin of the American Meteorological Society*. 1647–1665. doi: 10.1175/BAMS-D-14-00089.1.
- McPhaden MJ, Zebiak SE, Glantz MH. 2006a. ENSO as an integrating concept in earth science. *Science* **314(5806)**: 1740–1745. doi: 10.1126/science.1132588.

- McPhaden MJ, Zhang X, Hendon HH, Wheeler MC. 2006b. Large scale dynamics and MJO forcing of ENSO variability. *Geophysical Research Letters* **33**: L16702. doi: 10.1029/2006GL026786.
- Mei CC, Stiassnie M, Yue DK-P. 2005. Theory and applications of ocean surface waves – Part 1: Linear aspects. Advanced Series on Ocean Engineering **23**. World Scientific Publishing Co. Pte. Ltd, Singapore.
- Méndez FJ, Menéndez M, Luceño A, Losada IJ. 2006. Estimation of the long-term variability of extreme significant wave height using a time-dependent Peak Over Threshold (POT) model. *Journal of Geophysical Research* **111**: C07024. doi: 10.1029/2005JC003344.
- Méndez FJ, Menéndez M, Luceño A, Medina R, Graham NE. 2008. Seasonality and duration in extreme value distributions of significant wave height. *Ocean Engineering* **35**: 131–138. doi: 10.1016/j.oceaneng.2007.07.012.
- Mendoza ET, Jimenez JA. 2006. Storm-induced beach erosion potential on the Catalanian coast, *Journal of Coastal Research* **SI48** (Proceedings of the 3rd Spanish Conference on Coastal Geomorphology): 81-88. Las Palmas de Gran Canaria – Spain, ISSN 0749–0208.
- Menéndez M, Méndez FJ, Izaguirre C, Luceño A, Losada IJ. 2009. The influence of seasonality on estimating return values of significant wave height. *Coastal Engineering* **56**: 211–219. doi: 10.1016/j.coastaleng.2008.07.004.
- Menéndez M, Méndez FJ, Losada IJ, Graham NE. 2008. Variability of extreme wave heights in the northeast Pacific Ocean based on buoy measurements. *Geophysical Research Letters* **35**: L22607. doi: 10.1029/2008GL035394.
- Mo KC, Nogues-Paegle J. 2005. Pan-America. In: *Intraseasonal variability in the atmosphere-ocean climate system*. Springer Praxis Books (Environmental Sciences). Springer, Berlin, Heidelberg: 95–124. doi: 10.1007/3-540-27250-X_4.

- Mo KC, Paegle JN. 2001. The Pacific-South American modes and their downstream effects. *International Journal of Climatology* **21(10)**: 1211–1229. doi: 10.1002/joc.685.
- Mo KC, White GH. 1985. Teleconnections in the Southern Hemisphere. *Monthly Weather Review* **113(1)**: 22–37. doi: 10.1175/1520-0493(1985)113<0022:TITSH>2.0.CO;2.
- Moeini MH, Etemad-Shahidi A, Chegini V. 2010. Wave modeling and extreme value analysis off the northern coast of the Persian Gulf. *Applied Ocean Research* **32**: 209–218. doi: 10.1016/j.apor.2009.10.005.
- Moon J-Y, Wang B, Ha K-J. 2011. ENSO regulation of MJO teleconnection. *Clim. Dyn.* **37**: 1133–1149. doi: 10.1007/s00382-010-0902-3.
- Mori M, Watanabe M. 2008. The growth and triggering mechanisms of the PNA: A MJO-PNA coherence. *Journal of the Meteorological Society of Japan* **86(1)**: 213–236. doi: 10.2151/jmsj.86.213.
- Morris M, Stanton B, Neil H. 2001. Subantarctic oceanography around New Zealand: preliminary results from an ongoing survey. *New Zealand Journal of Marine and Freshwater Research* **35(3)**: 499–519. doi: 10.1080/00288330.2001.9517018.
- Morrisey D, Beard C, Morrison M, Craggs R, Lowe M. 2007. The New Zealand Mangrove: Review of the Current State Of Knowledge. Auckland Regional Council Technical Publication Number 325.
- Mortlock TR, Goodwin ID. 2016. Impacts of enhanced central Pacific ENSO on wave climate and headland-bay beach morphology. *Continental Shelf Research* **120**: 14–25. doi: 10.1016/j.csr.2016.03.007.
- Munk WH, Miller GR, Snodgrass FE, Barber NF. 1963. Directional recording of swell from distant storms. *Phil. Trans. R. Soc. A* **255**: 505–584. doi:10.1098/rsta.1963.0011.

- Nanba N, Fujiwara T, Kuwano K, Ishikawa Y, Ogawa H, Kado R. 2011. Effect of water flow velocity on growth and morphology of cultured *Undaria pinnatifida* sporophytes (Laminariales, Phaeophyceae) in Okirai Bay on the Sanriku coast, Northeast Japan. *J. Appl. Phycol.* **23(6)**: 1023–1030. doi: 10.1007/s10811-010-9635-2.
- Neelamani S, Al-Salem K, Rakha K. 2007. Extreme waves for Kuwaiti territorial waters. *Ocean Engineering* **34**: 1469–1504. doi: 10.1016/j.oceaneng.2006.08.013.
- Neelin JD, Battisti DS, Hirst AC, Jin F-F, Wakata Y, Yamagata T, Zebiak SE. 1998. ENSO theory. *Journal of Geophysical Research: Oceans* **103(C7)**: 14261–14290. doi: 10.1029/97JC03424.
- Neumann CJ. 1993. "Global overview" – Chapter 1, Global guide to tropical cyclone forecasting. *WMO/TD-No560*. Report No. TCP-31. World Meteorological Organization, Geneva, Switzerland.
- Nunes M, Ferreira Ó, Loureiro C, Baily B. 2011. Beach and cliff retreat induced by storm groups at Forte Novo, Algarve (Portugal). *Journal of Coastal Research* **SI64** (Proceedings of the 11th International Coastal Symposium): 795–799. Szczecin, Poland, ISSN 0749–0208.
- Pezza AB, Simmonds I, Renwick JA. 2007. Southern Hemisphere cyclones and anticyclones: Recent trends and links with decadal variability in the Pacific Ocean. *International Journal of Climatology* **27(11)**: 1403–1419. doi: 10.1002/joc.1477.
- Phillips MS, Turner IL, Cox RJ, Splinter KD, Harley MD. 2015. Will the sand come back?: Observations and characteristics of beach recovery. *Australasian Coasts & Ports Conference 2015: 22nd Australasian Coastal and Ocean Engineering Conference and the 15th Australasian Port and Harbour Conference, Auckland, New Zealand: Engineers Australia and IPENZ*: 676–682. ISBN: 9781922107794.

- Pickrill RA, Mitchell JS. 1979. Ocean wave characteristics around New Zealand. *New Zealand Journal of Marine and Freshwater Research* **13(4)**: 501-520. doi: 10.1080/00288330.1979.9515827.
- Pinto JG, Gómara I, Masato G, Dacre HF, Woollings T, Caballero R. 2014. Large-scale dynamics associated with clustering of extratropical cyclones affecting Western Europe. *J. Geophys. Res. Atmos.* **119**: 13,704–13,719. doi: 10.1002/2014JD022305.
- Pinto JG, Bellenbaum N, Karremann MK, Della-Marta PM. 2013. Serial clustering of extratropical cyclones over the North Atlantic and Europe under recent and future climate conditions. *J. Geophys. Res. Atmos.* **118(22)**: 12,476–12,485. doi: 10.1002/2013JD020564.
- Quan S, Kvitek RG, Smith DP, Griggs GB. 2013. Using vessel-based LIDAR to quantify coastal erosion during El Niño and Inter-El Niño periods in Monterey Bay, California. *Journal of Coastal Research* **29(3)**: 555–565. doi: 10.2112/JCOASTRES-D-12-00005.1.
- Raphael MN. 2004. A zonal wave 3 index for the Southern Hemisphere. *Geophys. Res. Lett.* **31**: L23212. doi: 10.1029/2004GL020365.
- Rapizo H, Babanin AV, Schulz E, Hemer MA, Durrant TH. 2015. Observation of wind-waves from a moored buoy in the Southern Ocean. *Ocean Dynamics* **65**: 1275–1288. doi: 10.1007/s10236-015-0873-3.
- Rapp D. 2008. Assessing climate change: temperatures, solar radiation, and heat balance. Springer.
- Reguero BG, Losada IJ, Méndez FJ. 2015. A global wave power resource and its seasonal, interannual and long-term variability. *Applied Energy* **148**: 366–380. doi: 10.1016/j.apenergy.2015.03.114.
- Reguero BG, Menéndez M, Méndez FJ, Mínguez R, Losada IJ. 2012. A Global Ocean Wave (GOW) calibrated reanalysis from 1948 onwards. *Coastal Engineering* **65**: 38–55. doi: 10.1016/j.coastaleng.2012.03.003.

- Revell CG, Goulter SW. 1986. South Pacific tropical cyclones and the Southern Oscillation. *Monthly Weather Review* **114(6)**: 1138–1145. doi: 10.1175/1520-0493(1986)114<1138:SPTCAT>2.0.CO;2.
- Rind. 2008. The consequences of not knowing low- and high-latitude climate sensitivity. *Bull. Amer. Meteor. Soc.* **89**: 855–864. doi: 10.1175/2007BAMS2520.1.
- Ropelewski CF, Halpert MS. 1987. Global and regional scale precipitation patterns associated with the El Niño/Southern Oscillation. *Monthly weather review* **115(8)**: 1606–1626. doi: 10.1175/1520-0493(1987)115<1606:GARSPP>2.0.CO;2.
- Ropelewski CF, Jones PD. 1987. An extension of the Tahiti-Darwin Southern Oscillation Index. *Monthly Weather Review* **115(9)**: 2161–2165. doi: 10.1175/1520-0493(1987)115<2161:AEOTTS>2.0.CO;2.
- Roundy PE, Kravitz JR. 2009. The association of the evolution of intraseasonal oscillations to ENSO phase. *Journal of Climate* **22**: 381–395. doi: 10.1175/2008JCLI2389.1.
- Roundy PE, MacRitchie K, Asuma J, Melino T. 2010. Modulation of the global atmospheric circulation by combined activity in the Madden-Julian Oscillation and the El Niño-Southern Oscillation during boreal winter. *Journal of Climate* **23**: 4045–4059. doi: 10.1175/2010JCLI3446.1.
- Ruggiero P, Komar PD, Allan JC. 2010. Increasing wave heights and extreme value projections: The wave climate of the U.S. Pacific Northwest. *Coastal Eng.* **57**: 539–552. doi: 10.1016/j.coastaleng.2009.12.005.
- Russell JL, Dixon KW, Gnanadesikan A, Stouffer RJ, Toggweiler JR. 2006. The Southern Hemisphere westerlies in a warming world: Propping open the door to the deep ocean. *Journal of Climate* **19**: 6382–6390. doi: 10.1175/JCLI3984.1.

- Rusu E, Guedes Soares C. 2009. Numerical modelling to estimate the spatial distribution of the wave energy in the Portuguese nearshore. *Renewable Energy* **34(6)**: 1501–1516. doi: 10.1016/j.renene.2008.10.027.
- Saha S, Moorthi S, Pan H, Wu X, Wang J, Nadiga S, Tripp P, Kistler R, Wollen J, Behringer D, Liu H, Stokes D, Grumbine R, Gayno G, Wang J, Hou Y, Chuang H, Juang HH, Sela J, Iredell M, Treadon R, Kleist D, Van Delst P, Keyser D, Derber J, Ek M, Meng J, Wei H, Yang R, Lord S, van den Dool H, Kumar A, Wang W, Long C, Chelliah M, Xue Y, Huang B, Schemm J, Ebisuzaki W, Lin R, Xie P, Chen M, Zhou S, Higgins W, Zou C, Liu Q, Chen Y, Han Y, Cucurull L, Reynolds R, Rutledge G, Goldberg M. 2010. The NCEP climate forecast system reanalysis. *Bull. Am. Meteorol. Soc.* **91**: 1015–1057. doi: 10.1175/2010BAMS3001.1.
- Saji NH, Goswami BN, Vinayachandran PN, Yamagata T. 1999. A dipole mode in the tropical Indian Ocean. *Nature* **401**: 360–363. doi: 10.1038/43854.
- Sallée J-B, Matear RJ, Rintoul SR, Lenton A. 2012. Localized subduction of anthropogenic carbon dioxide in the Southern Hemisphere oceans. *Nature Geoscience* **5**: 579–584. doi: 10.1038/NGEO1523.
- Sasaki YN, Minobe S, Schneider N, Kagimoto T, Nonaka M, Sasaki H. 2008. Decadal sea level variability in the South Pacific in a global eddy-resolving ocean model hindcast. *Journal of Physical Oceanography* **38(8)**: 1731–1747. doi: 10.1175/2007JPO3915.1.
- Schiel DR, Thompson GA. 2012. Demography and population biology of the invasive kelp *Undaria pinnatifida* on shallow reefs in southern New Zealand. *Journal of Experimental Marine Biology and Ecology* **434–435**: 25–33. doi: 10.1016/j.jembe.2012.07.023.
- Schott FA, Xie S, McCreary JP. 2009. Indian Ocean circulation and climate variability. *Rev. Geophys.* **47**: RG1002. doi: 10.1029/2007RG000245.

- Seiki A, Takayabu YN, Yoneyama K, Sato N, Yoshizaki M. 2009. The oceanic response to the Madden-Julian Oscillation and ENSO. *SOLA* **5**: 93–96. doi: 10.2151/sola.2009–024.
- Semedo A, Sušelj K, Rutgersson A, Sterl A. 2011. A global view on the wind sea and swell climate and variability from ERA-40. *Journal of Climate* **24**: 1461–1479. doi: 10.1175/2010JCLI3718.1.
- Sen PK. 1968. Estimates of the regression coefficient based on Kendall's Tau. *Journal of the American Statistical Association* **63(324)**: 1379–1389. doi: 10.1080/01621459.1968.10480934.
- Senechal N, Castelle B, Bryan KR. 2017. Storm clustering and beach response. In *Coastal Storms: Processes and Impacts*. Wiley-Blackwell: New York, USA.
- Seo K-H, Son S-W. 2012. The global atmospheric circulation response to tropical diabatic heating associated with the Madden–Julian Oscillation during northern winter. *Journal of the Atmospheric Sciences* **69(1)**: 79–96. doi: 10.1175/2011JAS3686.1.
- Shimizu MH, Ambrizzi T. 2016. MJO influence on ENSO effects in precipitation and temperature over South America. *Theor. Appl. Climatol.* **124**: 291–301. doi: 10.1007/s00704-015-1421-2.
- Shimizu MH, Cavalcanti IFA. 2011. Variability patterns of Rossby wave source. *Clim. Dyn.* **37**: 441–454. doi: 10.1007/s00382-010-0841-z.
- Shimura T, Mori N, Mase H. 2013. Ocean waves and teleconnection patterns in the Northern Hemisphere. *Journal of Climate* **26**: 8654–8670. doi: 10.1175/JCLI-D-12-00397.1.
- Simmonds I, Keay K. 2000. Variability of Southern Hemisphere extratropical cyclone behavior, 1958–97. *J. Clim.* **13(2)**: 550–561. doi: 10.1175/1520-0442(2000)013<0550:VOSHEC>2.0.CO;2.

- Sinclair MR. 1995. A climatology of cyclogenesis for the Southern Hemisphere. *Mon. Weather Rev.* **123 (6)**: 1601–1619. doi: 10.1175/1520-0493(1995)123<1601:ACOCFT>2.0.CO;2.
- Sinclair MR, Renwick JA, Kidson JW. 1997. Low-frequency variability of Southern Hemisphere sea level pressure and weather system activity. *Mon. Weather Rev.* **125**: 2531–2543. doi: 10.1175/1520-0493(1997)125%3C2531:LFVOSH%3E2.0.CO;2.
- Snodgrass FE, Groves GW, Hasselmann KF, Miller GR, Munk WH, Powers WH. 1966. Propagation of ocean swell across the pacific. *Phil. Trans. R. Soc. A* **259(1103)**: 431–497. doi:10.1098/rsta.1966.0022.
- Splinter KD, Carley JT, Golshani A, Tomlinson R. 2014. A relationship to describe the cumulative impact of storm clusters on beach erosion. *Coastal Engineering* **83**: 49–55. doi: 10.1016/j.coastaleng.2013.10.001.
- Stammerjohn SE, Martinson DG, Smith RC, Yuan X, Rind D. 2008. Trends in Antarctic annual sea ice retreat and advance and their relation to El Niño-Southern Oscillation and Southern Annular Mode variability. *Journal of Geophysical Research* **113(C3)**: C03S90. doi: 10.1029/2007JC004269.
- Stan C, Straus DM, Frederiksen JS, Lin H, Maloney ED, Schumacher C. 2017. Review of tropical-extratropical teleconnections on intraseasonal time scales. *Reviews of Geophysics* **55**. doi: 10.1002/2016RG000538.
- Stephens SA, Gorman RM. 2006. Extreme wave predictions around New Zealand from hindcast data. *New Zealand Journal of Marine and Freshwater Research* **40(3)**: 399–411. doi: 10.1080/00288330.2006.9517431.
- Stephens SA, Ramsay DL. 2014. Extreme cyclone wave climate in the Southwest Pacific Ocean: Influence of the El Niño Southern Oscillation and projected climate change. *Global and Planetary Change* **123(A)**: 13–26. doi: 10.1016/j.gloplacha.2014.10.002.

- Sterl A, Caires S. 2005. Climatology, variability and extrema of ocean waves: the web-based KNMI/ERA-40 wave atlas. *International Journal of Climatology* **25(7)**: 963–977. doi: 10.1002/joc.1175.
- Sterl A, Komen GJ, Cotton PD. 1998: Fifteen years of global wave hindcasts using winds from the European Centre for Medium-Range Weather Forecasts reanalysis: validating the reanalyzed winds and assessing the wave climate. *Journal of Geophysical Research: Oceans* **103**: 5477–5492. doi: 10.1029/97JC03431.
- Stokes DJ, Harris RJ. 2015. Sediment properties and surface erodibility following a large-scale mangrove (*Avicennia marina*) removal. *Continental Shelf Research* **107**: 1–10. doi: 10.1016/j.csr.2015.07.011.
- Stopa JE, Ardhuin F, Babanin A, Zieger S. 2016. Comparison and validation of physical wave parameterizations in spectral wave models. *Ocean Modelling* **130**: 2–17. doi: 10.1016/j.ocemod.2015.09.003.
- Stopa JE, Cheung KF, Tolman HL, Chawla A. 2013. Patterns and cycles in the Climate Forecast System Reanalysis wind and wave data. *Ocean Modelling* **70**: 207–220. doi:10.1016/j.ocemod.2012.10.005.
- Stopa JE, Cheung KF. 2014. Periodicity and patterns of ocean wind and wave climate. *Journal of Geophysical Research: Oceans* **119**: 5563–5584. Doi: 10.1002/2013JC009729.
- Storlazzi CD, Shope JB, Erikson LH, Hegermiller CA, Barnard PL. 2015. Future wave and wind projections for United States and United States-affiliated Pacific Islands. *U.S. Geological Survey Open-File Report 2015-1001*: 1–426. doi: 10.3133/ofr20151001.
- Student. 1908. The probable error of a mean. *Biometrika* **6(1)**: 1–25. doi: 10.2307/2331554.
- Swail VR, Cardone VJ, Ferguson M, Gummer DJ, Harris EL, Orelup EA, Cox AT. 2006. The MSC50 wind and wave reanalysis. *Proc. 9th International Workshop*

On Wave Hindcast and Forecasting, September 25-29, Victoria, B.C. Canada.

- Taschetto AS, Gupta AS, Hendon HH, Ummenhofer CC, England MH. 2011. The contribution of Indian Ocean sea surface temperature anomalies on Australian summer rainfall during El Niño events. *Journal of Climate* **24**: 3734–3747. doi: 10.1175/2011JCLI3885.1.
- Taylor PH, Barker VE, Bishop D, Eatock Taylor R. 2009. 100-year waves, teleconnections and wave climate variability. *paper presented at 11th International Workshop on Wave Hindcasting and Forecasting*, Environment Canada, Canadian Federal Program of Energy R&D, WMO/IOC Joint Technical Commission for Oceanography and Marine Meteorology (JCOMM), Halifax, Nova Scotia, Canada.
- Theil H. 1950. A rank-invariant method of linear and polynomial regression analysis. *Proceedings of the Royal Netherlands Academy of Sciences* **53(Part I)**: 386–392; **(Part II)**: 521–525; **(Part III)**: 1397–1412.
- Thompson DWJ, Solomon S. 2002. Interpretation of recent Southern Hemisphere climate change. *Science* **296**: 895–899. doi: 10.1126/science.1069270.
- Tolman, HL. 1991. A third-generation model for wind waves on slowly varying, unsteady, and inhomogeneous depths and currents. *Journal of Physical Oceanography* **21**: 782–797. doi: 10.1175/1520-0485(1991)021<0782:ATGMFW>2.0.CO;2.
- Tolman HL. 2009. User manual and system documentation of WAVEWATCH III version 3.14, NOAA/NWS/NCEP/MMAB Tech. Note 276, 194 pp + Appendices, NOAA, Camp Springs, Md. [Available at <http://polar.ncep.noaa.gov/waves/wavewatch/wavewatch.shtml>.]
- Tolman HL, Chalikov DV. 1996. Source terms in a third-generation wind-wave model. *J. Phys. Oceanogr.* **26 (11)**: 2497–2518. doi: 10.1175/1520-0485(1996)026(2497:STIATG)2.0.CO;2.

- Torrence C, Compo GP. 1998. A practical guide to wavelet analysis. *Bull. Am. Meteorol. Soc.* **79(1)**: 61–78. doi: 10.1175/1520-0477(1998)079<0061:APGTWA>2.0.CO;2.
- Trenberth KE. 1997. The definition of El Niño. *Bulletin of the American Meteorological Society* **78(12)**: 2771–2777. doi: 10.1175/1520-0477(1997)078<2771:TDOENO>2.0.CO;2.
- Trenberth KE. 1980. Planetary waves at 500 mb in the Southern Hemisphere. *Monthly Weather Review* **108(9)**: 1378–1389. doi: 10.1175/1520-0493(1980)108<1378:PWAMIT>2.0.CO;2.
- Trenberth KE, Caron JM, Stepaniak DP, Worley S. 2002. Evolution of El Niño–Southern Oscillation and global atmospheric surface temperatures. *Journal of Geophysical Research: Atmospheres* **107(D8)**. doi: 10.1029/2000JD000298.
- Trenberth KE, Hoar TJ. 1996. The 1990–1995 El Niño–Southern Oscillation event: Longest on record. *Geophysical Research Letters* **23(1)**: 57–60. doi: 10.1029/95GL03602.
- Trenberth KE, Hurrell JW. 1994. Decadal atmosphere–ocean variations in the Pacific. *Climate Dynamics* **9(6)**: 303–319. doi: 10.1007/BF00204745.
- Uppala SM, Kallberg PW, Simmons AJ, Andrae U, Bechtold VDC, Fiorino M, Gibson JK, Haseler J, Hernandez A, Kelly GA, Li X, Onogi K, Saarinen S, Sokka N, Allan RP, Andersson E, Arpe K, Balmaseda MA, Beljaars ACM, Berg LVD, Bidlot J, Bormann N, Caires S, Chevallier F, Dethof A, Dragosavac M, Fisher M, Fuentes M, Hagemann S, Hólm E, Hoskins BJ, Isaksen L, Janssen PAEM, Jenne R, McNally AP, Mahfouf J-F, Morcrette J-J, Rayner NA, Saunders RW, Simon P, Sterl A, Trenberth KE, Untch A, Vasiljevic D, Viterbo P, Woollen J. 2005. The ERA-40 re-analysis. *Quart. J. Roy. Meteorol. Soc.* **131(612)**: 2961–3012. doi: 10.1256/qj.04.176.

- van Loon H, Jenne RL. 1972. The zonal harmonic standing waves in the Southern Hemisphere. *Journal of Geophysical Research* **77(6)**: 992–1003. doi: 10.1029/JC077i006p00992.
- Veltcheva A, Guedes Soares C. 2015. Wavelet analysis of non-stationary sea waves during Hurricane Camille. *Ocean Engineering* **95**: 166–174. doi: 10.1016/j.oceaneng.2014.11.035.
- Villarini G, Smith JA, Vitolo R, Stephenson DB. 2013. On the temporal clustering of US floods and its relationship to climate teleconnection patterns. *International Journal of Climatology* **33(3)**: 629–640. doi: 10.1002/joc.3458.
- Vinoth J, Young IR. 2011. Global estimates of extreme wind speed and wave height. *Journal of Climate* **24**: 1647–1665. doi: 10.1175/2010JCLI3680.1.
- Vitolo R, Stephenson DB, Cook IM, Mitchell-Wallace K. 2009. Serial clustering of intense European storms. *Meteorologische Zeitschrift* **18(4)**: 411–424. doi: 10.1127/0941-2948/2009/0393.
- Vousdoukas MI, Almeida LP, Ferreira Ó. 2011. Modelling storm-induced beach morphological change in a meso-tidal, reflective beach using XBeach. *Journal of Coastal Research* **SI64** (Proceedings of the 11th International Coastal Symposium): 1916–1920. Szczecin, Poland, ISSN 0749–0208.
- Walker GT, Bliss EW. 1932. World weather V. *Memoirs of the Royal Meteorological Society* **4(36)**: 53–84.
- Walker GT, Bliss EW. 1937. World weather VI. *Memoirs of the Royal Meteorological Society* **4(39)**: 119–139.
- Walsh KJE, McInnes KL, McBride JL. 2012. Climate change impacts on tropical cyclones and extreme sea levels in the South Pacific — A regional assessment. *Global and Planetary Change* **80–81**: 149–164. doi: 10.1016/j.gloplacha.2011.10.006.

- WAMDI Group. 1988. The WAM Model – A third generation ocean wave prediction model. *Journal of Physical Oceanography* **18**: 1775–1810. doi: 10.1175/1520-0485(1988)018<1775:TWMTGO>2.0.CO;2.
- Wang G, Cai W. 2013. Climate-change impact on the 20th-century relationship between the Southern Annular Mode and global mean temperature. *Scientific Reports* **3**: 1–6. doi: 10.1038/srep02039.
- Webster PJ, Moore AM, Loschnigg JP, Leben RR. 1999. Coupled ocean-atmosphere dynamics in the Indian Ocean during 1997–98. *Nature* **401**: 356–360. doi: 10.1038/43848.
- Wentz FJ, Ricciardulli L, Hilburn K, Mears C. 2007. How much more rain will global warming bring? *Science* **317(5835)**: 233–235. doi: 10.1126/science.1140746.
- Wheeler MC, Hendon HH. 2004. An all-season real-time multivariate MJO index: development of an index for monitoring and prediction. *Monthly Weather Review* **132**: 1917–1932. doi: 10.1175/1520-0493(2004)132<1917:AARMMI>2.0.CO;2.
- Wilks DS. 2006. *Statistical methods in the atmospheric sciences*. Academic Press 3rd edition: London, UK, pp 704. doi: 10.1016/S0074-6142(06)80036-7.
- Woolf DK, Challenor PG, Cotton PD. 2002. Variability and predictability of the North Atlantic wave climate. *Journal of Geophysical Research: Oceans* **107(C10)**: 3145. doi: 10.1029/2001JC001124.
- World Bank Group. 2016. Global Economic Prospects, January 2016: Spillovers amid Weak Growth. Washington, DC, World Bank, Washington, D.C. doi: 10.1596/978-1-4648-0675-9.
- WW3DG, 2016. The WAVEWATCH III Development Group: User manual and system documentation of WAVEWATCH III version 5.16. Tech. Note 329, NOAA/NWS/NCEP/MMAB, College Park, MD, USA, 326 pp. + Appendices.

- Wyrski K. 1975. El Niño — the dynamic response of the equatorial Pacific Ocean to atmospheric forcing. *Journal of Physical Oceanography* **5**: 572–584. doi: 10.1175/1520-0485(1975)005<0572:ENTDRO>2.0.CO;2.
- Yamada Y, Oouchi K, Satoh M, Tomita H, Yanase W. 2010. Projection of changes in tropical cyclone activity and cloud height due to greenhouse warming: global cloud-system-resolving approach. *Geophysical Research Letters* **37**: L07709. doi: 10.1029/2010GL042518.
- Yates ML, Guza RT, O'Reilly WC. 2009. Equilibrium shoreline response: Observations and modelling. *Journal of Geophysical Res.* **114**: C09014. doi: 10.1029/2009JC005359.
- Young IR. 1994. Global ocean wave statistics obtained from satellite observations. *Applied Ocean Research* **16(4)**: 235–248. doi: 10.1016/0141-1187(94)90023-X.
- Young IR. 1999. Seasonal variability of the global ocean and wind and wave climate. *International Journal of Climatology* **19(9)**: 931–950. doi: 10.1002/(SICI)1097-0088(199907)19:9<931::AID-JOC412>3.0.CO;2-O.
- Young IR, Vinoth J, Zieger S, Babanin AV. 2012. Investigation of trends in extreme value wave height and wind speed. *J. Geophys. Res.* **117**: C00J06. doi: 10.1029/2011JC007753.
- Young IR, Zieger S, Babanin AV. 2011. Global trends in wind speed and wave height. *Science* **332**: 451–455. doi: 10.1126/science.1197219.
- Young IR, Zieger S, Babanin AV. 2011. Response to comment on: "Global trends in wind speed and wave height". *Science* **334(6058)**: 905. doi: 10.1126/science.1210548.
- Yuan J, Cao J. 2013. North Indian Ocean tropical cyclone activities influenced by the Indian Ocean Dipole mode. *Science China Earth Sciences* **56(5)**: 855–865. doi: 10.1007/s11430-012-4559-0.

- Yuan X, Li C. 2008. Climate modes in southern high latitudes and their impacts on Antarctic sea ice. *Journal of Geophysical Research* **113(C6)**: C06S91. doi:10.1029/2006JC004067.
- Zhang C. 2005. Madden-Julian Oscillation. *Reviews of Geophysics* **43(2)**: RG2003. doi: 10.1029/2004RG000158.
- Zhang Y, Wallace JM, Battisti DS. 1997. ENSO-like interdecadal variability: 1900–93. *Journal of Climate* **10(5)**: 1004–1020. doi: 10.1175/1520-0442(1997)010<1004:ELIV>2.0.CO;2.